

**ULTRAVIOLET-ASSISTED OXIDATION AND NITRIDATION OF HAFNIUM AND
HAFNIUM ALUMINUM ALLOYS AS POTENTIAL GATE DIELECTRICS FOR
METAL OXIDE SEMICONDUCTOR APPLICATIONS**

By

CHAD ROBERT ESSARY

A DISSERTATION PRESENTED TO THE GRADUATE SCHOOL
OF THE UNIVERSITY OF FLORIDA IN PARTIAL FULFILLMENT
OF THE REQUIREMENTS FOR THE DEGREE OF
DOCTOR OF PHILOSOPHY

UNIVERSITY OF FLORIDA

2004

Copyright 2004

by

Chad Robert Essary

This document is dedicated to my loving family.

ACKNOWLEDGMENTS

I would like to first thank my advisor, Dr. Rajiv Singh, for giving me the opportunity to study this exciting field of electronic materials. Also I want to thank Dr. Valentin Craciun and Dr. Joshua Howard for being good friends as well as mentors to me during my time here at the University of Florida. To all the group members I have had the pleasure to work with and to our wonderful secretary Margaret, I would like to offer my sincere gratitude for all your help and friendship all of you have provided my four years here at the University of Florida. Furthermore, I would like to thank Dr. Cammy Abernathy, Dr. Stephen Pearton, Dr. David Norton, and Dr. Fan Ren for taking the time to serve on my committee and for providing direction and guidance. Finally, I would like to thank the electronics group at the University of Texas-Austin for helping with the electrical measurements on a portion of this dissertation.

TABLE OF CONTENTS

	<u>page</u>
ACKNOWLEDGMENTS	iv
LIST OF TABLES	viii
LIST OF FIGURES	x
ABSTRACT.....	xiii
CHAPTER	
1 LITERATURE REVIEW	1
Introduction.....	1
CMOS Transitors	3
Properties and Limitations of SiO ₂	5
Materials Selection Guideline.....	7
Band Gap and Alignment	8
Thermodynamic Stability	8
Film Morphology and Interface Quality.....	10
Implementation and Process Compatibility.....	10
Reliability	11
Hafnium Oxide Properties	11
Hafnium Oxide Research.....	12
Nitride Barrier Layers.....	13
Other Novel Approaches	14
UV Assisted Oxidation.....	15
Motivation.....	18
2 EXPERIMENTAL PROCEDURES	19
Deposition Setup and Equipment	19
UVPLD System.....	19
Laser Ablation.....	21
Laser System	23
Experimental Setups and Samples	25
Interfacial Layer Formation and Growth.....	25
UV Assisted Oxidation and Nitridation of Hafnium Films	26
UV Assisted Oxidation and Nitridation of Hafnium/Aluminum Alloy Films	27

Experimental Characterization Techniques	28
Variable Angle Spectroscopic Ellipsometry	28
X-ray Reflectivity.....	29
X-ray Diffraction and Glancing Incidence X-ray Diffraction.....	31
X-ray Photoelectron Spectroscopy	33
Atomic Force Microscopy.....	34
Electrical Characterization	34
Current-Voltage Measurements.....	36
Capacitance-Voltage Measurement	37
3 KINETICS OF INTERFACIAL LAYER FORMATION DURING DEPOSITION OF HAFNIA ON SILICON.....	43
Deposition Conditions	43
X-ray Results	45
XPS Analysis	49
Ellipsometry Results.....	53
Summary.....	54
4 EFFECT OF UV-ASSISTED OXIDATION AND NITRICATION OF HAFNIUM METAL FILMS	56
Experiment.....	56
Results and Discussion for Low Temperature Deposited Samples	60
Surface Morphology	60
X-Ray Analysis	61
X-Ray Reflectivity.....	64
XPS Analysis	64
Electrical Properties Analysis	72
Capacitance-Voltage Results	72
Repeatability.....	74
Interfacial Trap Density Measurements	76
Current-Voltage Results	77
TEM Analysis.....	78
Proposed Model.....	79
Results and Discussion of the High Temperature Depositions	81
XPS	82
X-Ray Analysis	83
Electrical Characterization Results.....	85
Discussion.....	87
Summary.....	89
5 UV-ASSISTED OXIDATION AND NITRIDATION OF HAFNIUM ALUMINUM METAL ALLOY FILMS	90
Experiment.....	90
X-Ray Analysis	92

Compositional Comparisons	92
Electrical Characterization Results.....	94
High Temperature Anneal.....	96
Summary.....	98
6 CONCLUSIONS.....	99
APPENDIX	
A ELECTRICAL DATA EXTRACTION METHOD	102
B XPS DATA	107
LIST OF REFERENCES	111
BIOGRAPHICAL SKETCH	116

LIST OF TABLES

<u>Table</u>	<u>page</u>
1-1: Industrial roadmap for minimum feature size	5
1-2: Various properties of high-k oxide materials.	8
1-3: Gibbs free energy of formation for potential alternative high-k dielectrics.	10
1-4: Various properties of HfO ₂	12
2-1: Conditions for growth of ultra-thin HfO ₂ films.....	26
2-2: Growth and postdeposition conditions for UV oxidation of Hf	27
2-3: High temperature Hf metal deposition and oxidation conditions.....	27
2-4: Growth and annealing conditions for Hf/Al metal films.....	28
2-5: Conversion factors for series-parallel electrical equivalent circuits.....	41
3-1: Conditions for growth of ultra-thin HfO ₂ films.....	44
3-2: XRR modeling parameters used to fit the spectra	48
3-3: Ellipsometry modeling results	54
3-4: Comparison of the thickness values (in Å) for HfO ₂ thin films deposited on Si.....	55
4-1: Growth and postdeposition conditions for UV oxidation of Hf	59
4-2: Z range and RMS roughness for oxidized Hf metal films.....	61
4-3: d/λ values for samples H2-H5	67
4-4: Dielectric constants and EOT for samples H2-H4.	74
4-5: Repeatability study results for k and EOT of oxidized hafnium metal films.	76
4-6: Defect density results for samples analyzed at UT-Austin.	77
4-7: EOT and k for the high temperature deposited samples.....	87

5-1: Sample deposition conditions	91
5-2: Sample composition from elemental analysis using XPS.	93
5-3: Predicted film density and bulk dielectric constant.....	94
5-4: Dielectric constants and EOT for the aluminum study samples.....	96

LIST OF FIGURES

<u>Figure</u>	<u>page</u>
1-1: Typical CMOS inverter.....	4
1-2: Energy band diagram of an n+ poly-Si/SiO ₂ /n-Si structure	7
1-3: Bandgap and band offset comparison for various dielectric materials.....	9
2-1: UVPLD system with excimer laser and optics setup.....	20
2-2: Photograph of UV lamp placement in the chamber.....	21
2-3: Laser energy distribution during target ablation.....	22
2-4: Typical XRR plot showing which film properties most influence various features.	30
2-5: Typical XRD equipment geometry setup	32
2-6: AFM operational setup showing laser detection of the cantilever deflection	35
2-7: MOS capacitor setup used for CV/IV measurements.....	36
2-8: Kiethley Instruments Inc. Win-82 measurement system.....	38
2-9: Typical capacitance/voltage response curve.....	40
2-10: Equivalent circuits for estimation of capacitance.....	42
3-1: Comparison of GIXD ($\Omega=1^\circ$) for the 200 °C and 600 °C samples.....	46
3-2: Acquired XRR spectrum and its simulation for a HfO ₂ film.....	47
3-3: Schematic of gate oxide stack model used for XRR simulations.....	47
3-4: Interfacial layer thickness dependence on O ₂ pressure for the 600 °C samples.	49
3-5: High resolution XPS scans of the Hf 4f region.....	50
3-6: Raw data and fit for the Si 2p region for the 600 °C, 1×10^{-2} Torr O ₂ sample.	51
3-7: Variations of d/λ values for a 5 nm pure SiO ₂ on Si and a deposited sample	52

3-8: Interfacial layer thickness as a function of temperature and pressure.....	53
4-1: CV response of an UV grown Si _x N _y film.....	57
4-2: 2D AFM scans of samples a) H2 and b) H3 taken using contact mode	62
4-3: 2D AFM scans of samples a) H4 and b) H5 taken using contact mode	63
4-4: 3D AFM micrographs of both a) UV-oxidized and b) non-irradiated	65
4-5: GIXD spectra ($\Omega=1^\circ$) of Hf films deposited on Si and oxidized.....	66
4-6: XRR plot and fit for as deposited Hf metal film.	66
4-7: Angle-resolved XPS Si 2p spectra for system calibration.....	68
4-8: Angle-resolved XPS Si 2p spectra for H2 and H3 (UV and no-UV films).....	68
4-9: O 1s spectra for H2 and H3 (UV and no-UV) films at 45 and 90°.....	69
4-10: Si 2p spectra for UV-oxidized films H4 and H2 (with and without nitrogen).	70
4-11: N 1s peak of as deposited nitrided Hf metal film.	71
4-12: N 1s peak after PDA for samples H4 and H5.....	71
4-13: Comparison of high and low frequency capacitance responses for sample H4.	75
4-14: High frequency capacitance voltage responses for samples H2-H4.	76
4-15: CV response and model fit data for samples H2, H4, and H5.....	77
4-16: Current voltage results from oxidized hafnium metal films.....	78
4-17: XTEM of the UV annealed nitrided sample H4.....	79
4-18: XTEM of non UV annealed hafnium film H3.....	81
4-19: Model of the effect of UV and nitrogen.	82
4-20: O 1s Peaks for the high temperature deposited sample set.	83
4-21: Hf 4f Peaks for the high temperature deposited sample set.	84
4-22: GIXD for the high temperature deposited samples taken at $\Omega = 0.5^\circ$	85
4-23: XRR plots and models for the high temperature deposited samples.	86
4-24: CV plots for the high temperature deposited samples	88

4-25: IV plots for the high temperature deposited samples	88
5-1: GIXD scans taken at $\Omega=1^\circ$ comparing the effects of aluminum additions	92
5-2: Compilation of the capacitance-voltage results.....	95
5-3: Compilation of the current-voltage results.	97
5-4: GIXD for sample AH3 annealed at 900 °C	97

Abstract of Dissertation Presented to the Graduate School
of the University of Florida in Partial Fulfillment of the
Requirements for the Degree of Doctor of Philosophy

**ULTRAVIOLET-ASSISTED OXIDATION AND NITRIDATION OF HAFNIUM AND
HAFNIUM ALUMINUM ALLOYS AS POTENTIAL GATE DIELECTRICS FOR
METAL OXIDE SEMICONDUCTOR APPLICATIONS**

By

Chad Robert Essary

December, 2004

Chair: Rajiv K. Singh

Major Department: Materials Science and Engineering

The continued miniaturization of silicon-based complimentary metal oxide semiconductor (CMOS) devices is pushing the limits of the silicon dioxide (SiO_2) gate dielectric. As the channel widths are decreased to increase packing densities and functionality of new chips, proportional vertical scaling of the dielectric must be maintained to keep constant capacitances. Silicon dioxide is approaching its fundamental limit in which it can be used as the gate dielectric due to high leakage currents resulting from direct tunneling through the layer. In order for the continued use of current CMOS gate design, an alternative material with a higher dielectric constant must be found. Several materials have been proposed but are still not providing the electrical characteristics favorable for use in the devices due to problems with excessive leakage and hysteresis resulting from the quality of the film and oxygen defects.

The goal of this study is to create higher quality films at lower processing temperatures with low leakage and less hysteresis than has been achieved with hafnium

oxide films. This study first examines the formation of the interfacial layer in pulsed laser deposited hafnium oxide films to understand the kinetics behind its formation. The second section focuses on the oxidation of pulsed laser deposited (PLD) hafnium metal thin films using ultraviolet (UV) assisted post-deposition annealing. Another set of samples was deposited in an ammonia atmosphere in order to incorporate nitrogen into the films. Comparisons of microstructure and stoichiometry of oxidized hafnium and oxy-nitride films were made using x-ray photospectroscopy, variable angle spectroscopic ellipsometry, glancing angle x-ray spectroscopy, x-ray reflectivity, and atomic force microscopy. Analysis of the interface between the films and the silicon substrate was carried out using x-ray reflectivity. The electrical characteristics of the films were characterized using capacitance-voltage and current-voltage measurements in order to compare the quality of the films. Ultimately a model of the effect of UV and nitrogen additions was presented. In the final portion of this work, additions of aluminum were used to increase the crystallization temperature of the films. The effect of aluminum both with and without nitrogen incorporation on the dielectric constant and leakage for the films was studied.

CHAPTER 1

LITERATURE REVIEW

Introduction

Over the past 30 years, the integrated circuit industry has strived to maintain constantly shrinking device geometries and increased chip density.¹ The decrease in device size has allowed for greater packing densities, thus increasing the functionality and speed of the chips. The industry trend has followed what is known as Moore's Law.

In 1965, Gordon Moore from Intel first noted that every two to three years a new technology generation with approximately doubled logic circuit density and a 40% performance increase is realized as design and processing methods are improved.²⁻³

Since then, through continued miniaturization of gate widths of the metal oxide semiconductor field effect transistors (MOSFET) and proportional vertical scaling, Moore's Law has been maintained.

In order to continue miniaturization using current MOSFET structure designs, the gate oxide, which is currently silicon dioxide, thickness must be reduced to less than 15 Å.⁴ This represents five atomic layers of oxide or less. Problems not only arise in processing to keep the thickness from varying across the gate, but also in the amount of leakage current that results due to quantum mechanical tunneling. Tunneling current increases exponentially as the thickness of the layer is decreased.⁵ Losses due to tunneling would exceed the power consumption standards the industry wishes to use.¹ In order for continued reduction in gate widths, alternative materials with higher dielectric constants (high-k) than silicon dioxide must be implemented.

Silicon dioxide (SiO_2) has been vital to the industry due to its abundance and many useful properties. First of all, SiO_2 is readily formed by the oxidation of the surface of the silicon layer and can be precisely controlled through both chemical and thermal means. This provides an easier process than a deposition technique and eliminates interfacial defects experienced with deposition because SiO_2 forms an atomically abrupt interface with silicon limiting the number of carrier traps that degrade the performance of the transistor. Furthermore, post-annealing in a hydrogen containing ambient can easily passivate dangling bonds. This excellent interface allows for high mobility of the carriers in the MOSFET channel and high device performance.⁵

Finding an alternative gate dielectric that will act as well as SiO_2 is not an easy task. Research groups are working on a wide range of single metal oxides and nitrides,⁶⁻⁹ binary compounds,¹⁰⁻¹³ and some ternary oxides.⁹ The replacement oxide must be thermodynamically stable on silicon up to current processing temperatures for the chips (~900-1000°C)^{1, 14-15} to avoid reactions with the silicon that create compounds with lower dielectric constants that parasitically hinder the benefits of the higher-k material. The dielectric also needs to resist leaching of the dopants from the silicon channel and the gate contact, which is currently heavily doped poly-silicon. The layer must form an atomically abrupt or near-atomically abrupt interface with silicon to minimize carrier traps at the surface of the channel and prevent mixing and formation of a lower-k silicate interface layer. Ideally, the layer would be single crystalline or amorphous to inhibit leakage due to grain boundaries. Growth of single crystals is a slow process and thus does not lend itself well to implementation into industry. With amorphous layers, some

materials will crystallize when heated, so careful selection of the material must be made based on the wafer processing conditions it will be subjected to after deposition.¹⁶

CMOS Transistors

The basis of the computer revolution of the past 30 years has been the use of complementary metal oxide semiconductor (CMOS) transistors as the logic components of the integrated circuits. Research on a new class of materials known as semiconductors conducted at Bell Laboratories began in 1945 in an attempt to replace vacuum tubes for signal amplification in long distance telecommunication applications. Vacuum tubes were bulky, unreliable, consumed too much power, and produced too much heat. The first design to utilize this new class of materials was the point contact transistor, created on December 16th, 1947. The point contact transistor consisted of gold foil on top of a plastic triangular piece in intimate contact with a chunk of germanium. This first design was modified within a year into the junction sandwich transistor and proved to be more practical, rugged, and easier to manufacture. Twelve years later, the field effect transistor was created based on the original theories predicted in the early 1900s and has remained the key design that has been continuously used and adjusted for the past forty years.

Figure 1-1 shows a typical CMOS inverter structure containing both a nMOS and a pMOS device working jointly.¹⁷ The gates are made of poly-Si and are heavily doped to reduce the sheet resistance along the lines and to tailor the work function of the gate to the type of channel being used. The poly-Si is insulated from the MOS channels by a thin gate oxide dielectric.

When a voltage is applied to the gate, a potential is set up across the dielectric. Depending on the type of the channel, the potential will either decrease or increase the

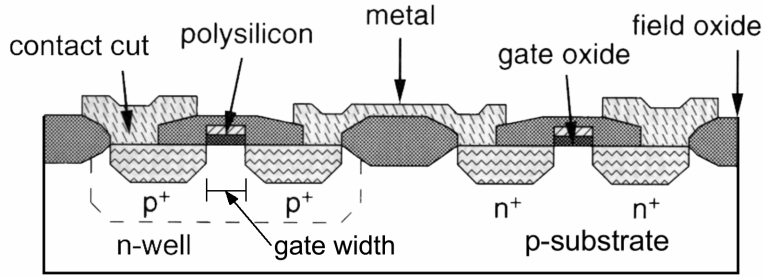


Figure 1-1: Typical CMOS inverter [17].

current from the source to the drain. For the inverter structure, when a voltage is applied (represented by a 1) typically the nMOS device will turn on and the pMOS device will turn off. The source for the nMOS is connected to ground (represented by a 0) and so passes the 0 to the drain. And vice-versa, when a 0 is applied to the gates, the pMOS structure, whose source is wired to line voltage, will turn on and pass the 1 signal to the drain while the nMOS will be turned off. By packing more of such logic components on the area of a chip, faster processing speeds can be obtained. There are design rules that must be followed as to the spacing between each device; however the rules, for the most part, scale with the dimensions of the gates.¹⁷ The current technology on the market now is 0.13 μm gate widths used in the Intel Pentium 4 processors.¹⁸ This corresponds to SiO_2 gate dielectric thickness of $\sim 20\text{\AA}$. For further gate width reduction, proportional scaling of the gate dielectric must be maintained to keep a constant capacitance across the gate channel area.

By replacing the SiO_2 with a material having a greater dielectric constant, the capacitance can be maintained while affording a thicker dielectric layer and thus reduce the leakage inherent with thinner films. This relationship is shown in equation (1-1).

$$t_{eq} = \frac{(t_{high-k} \cdot k_{ox})}{k_{high-k}} \quad (1-1)$$

t_{eq} = thickness of the equivalent SiO_2 layer

t_{ox} = thickness of the SiO_2 layer

κ_{ox} = dielectric constant of SiO_2

κ_{high-k} = dielectric constant of the alternative material

The interface between the silicon and the gate dielectric is very important because formation of a lower-k layer will result in thicker equivalent thickness. This is because the capacitances of the stacked layers add in series as shown in equation (1-2).

$$\frac{1}{C_{tot}} = \frac{1}{C_1} + \frac{1}{C_2} \quad (1-2)$$

C_{tot} = total capacitance

$C_{1,2}$ = respective capacitances of the layers

Ultimately by using higher-k materials if the interface can be controlled, t_{eq} thicknesses of $<10\text{\AA}$, which are needed for further advancement of the silicon based CMOS devices, can be realized. Table 1-1 shows the predicted roadmap for equivalent gate oxide thickness required for the minimum feature size.¹

Table 1-1: Industrial roadmap for minimum feature size and equivalent dielectric thickness in MOSFET devices.

Year	Minimum Feature Size (μm)	Equivalent Dielectric Thicknes (\AA)
1997	0.25	40-50
1999	0.18	30-40
2001	0.15	20-30
2003	0.13	20-25
2006	0.10	15-20
2009	0.07	10-15
2012	0.05	<10

Properties and Limitations of SiO_2

Amorphous SiO_2 has served as the gate dielectric for silicon-based CMOS devices due to its excellent properties. SiO_2 has a bandgap of 9 eV and a dielectric constant of 3.9 and can readily be formed on silicon with low defect concentrations at the interface. Using modern processing techniques, defect charge densities on the order of $10^{10}/\text{cm}^2$,

midgap interface state densities of $\sim 10^{10}/\text{cm}^2\text{eV}$, and hard breakdown fields of 15 MV/cm are routinely obtained.¹ The industry has come to rely on these standards when designing new chips. This presents a major challenge when trying to replace SiO₂. However, SiO₂ is approaching its limit of usefulness as the gate dielectric thickness requirements are pushed below 15 Å.

SiO₂ has a large conduction band offset (~3.5 eV) compared with silicon and therefore provides a stable electrical insulation layer. However, this offset decreases as the thickness of the layer is decreased. Ultimately, the SiO₂ layer loses its bulk properties at a thickness of around 7-8 Å.¹⁹ Below this thickness, the Si-rich interfacial regions from the channel and poly-Si gate interfaces overlap, causing an effective “short” through the dielectric, rendering it useless as an insulator. Experimental evidence has shown that ultrathin (13-15 Å) SiO₂ films can be processed which operate satisfactorily. However, high leakage current densities of 1-10 A/cm² have been measured for such devices.²⁰

In order to meet the power guidelines set forth by the industry, current leakage densities must be kept below $1 \times 10^{-1} \text{ A/cm}^2$ for gate biases of 1.2 V, corresponding to a contribution of only a few mW to the overall chip dissipation.²¹ For SiO₂ layers thicker than 6 nm, the leakage current mechanism is explained by Fowler-Nordheim electron tunnelling. As the layer thickness decreases, the mechanism switches to direct tunnelling. The difference between Fowler-Nordheim tunnelling (FNT) and direct tunnelling (DT) of electrons is determined by the shape of the tunnel barrier. If the oxide tunnel barrier is triangular, FNT occurs while DT takes place through a trapezoidal barrier as shown in Figure 1-2.²² This occurs because of the band offset reduction as the layer becomes thinner. As a result, the FNT leakage current is exponentially dependent

on the thickness of the oxide. To illustrate the drastic effect this relationship has, Buchanan in his review article gave the example: for silicon dioxide, at a gate bias of 1 V, the leakage current changes from $1 \times 10^{-12} \text{ A/cm}^2$ at 35\AA to $1 \times 10 \text{ A/cm}^2$ at 15 \AA , a change of 12 orders of magnitude.²³

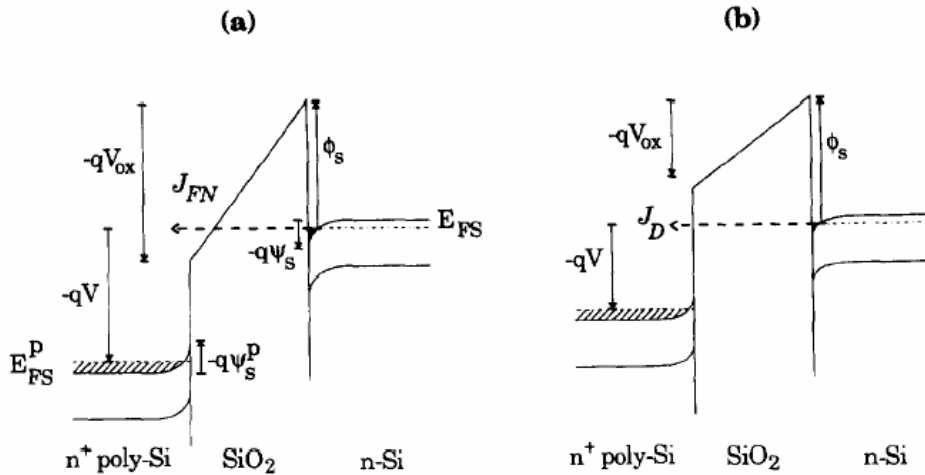


Figure 1-2: Energy band diagram of an n⁺ poly-Si/SiO₂/n-Si structure in the case of (a) Fowler-Nordheim tunnelling and (b) direct tunnelling of electrons from the Si degenerate accumulation layer into the poly-Si gate conduction band. [22]

Materials Selection Guideline

Many materials are being studied for use as replacement gate dielectrics. Over the past decade, Al₂O₃, ZrO₂, Y₂O₃, TiO₂, Ge₂O₃, La₂O₃, Ta₂O₃, HfO₂, SrTiO₃ and Ba_xSr_{1-x}TiO₃ have all been considered. Various properties of these materials are shown in Table 1-2.⁵ However, the following key properties suggested by Wilk *et al.*¹ must be considered when choosing a material:

- Permittivity, band gap, and band alignment to silicon
- Thermodynamic stability
- Film morphology
- Interface quality
- Compatibility with current or expected materials used in processing

- Process compatibility
- Reliability

Table 1-2: Various properties of high-k oxide materials.

Oxide Material	Dielectric Constant	Conduction Band Offset (eV)	Density (g/cm ³)	Melting Point (°C)	Stable in Contact with Silicon
Al ₂ O ₃	9.3	2.8	3.97	2054	YES
BaSr _{0.5} Ti _{0.5} O ₃	80 – 3600	-0.1 -0.1	6.02	1625	NO
CeO ₂	7	---	7.65	2400	YES
HfO ₂	22-25	1.5	9.68	2774	YES
Ta ₂ O ₅	24 – 65	0.3	8.20	1785	NO
TiO ₂	80 – 170	---	4.23	1843	NO
Y ₂ O ₃	10	2.3	5.03	2439	YES
ZrO ₂	~25	1.4	5.68	2710	YES

Band Gap and Alignment

The material should have a band gap offset of greater than 1 eV to that of the conduction band of silicon. This requirement rules out some of the higher dielectric materials such as SrTiO₃. Figure 1-3 graphically compares the band gaps and offsets of some potential alternative dielectrics to that of Si and SiO₂.^{24,25} Typically, materials with higher dielectric constants will have smaller band gaps, so an optimization must be made to balance the dielectric constant and band gap to get the best overall results. It was first believed that materials with very high dielectric constants such as SrTiO₃ and BaTiO₃ would be ideal so thick dielectric layers could be implemented. However due to their small band gap offsets to Si, they had shortcomings for use in gate dielectric applications but have found uses in RAM applications.

Thermodynamic Stability

The dielectric must be thermodynamically stable in contact with Si to prevent formation of SiO₂ or lower-k silicate structures. Single component oxides can be examined by comparing the Gibbs free energy of formation with respect to oxygen

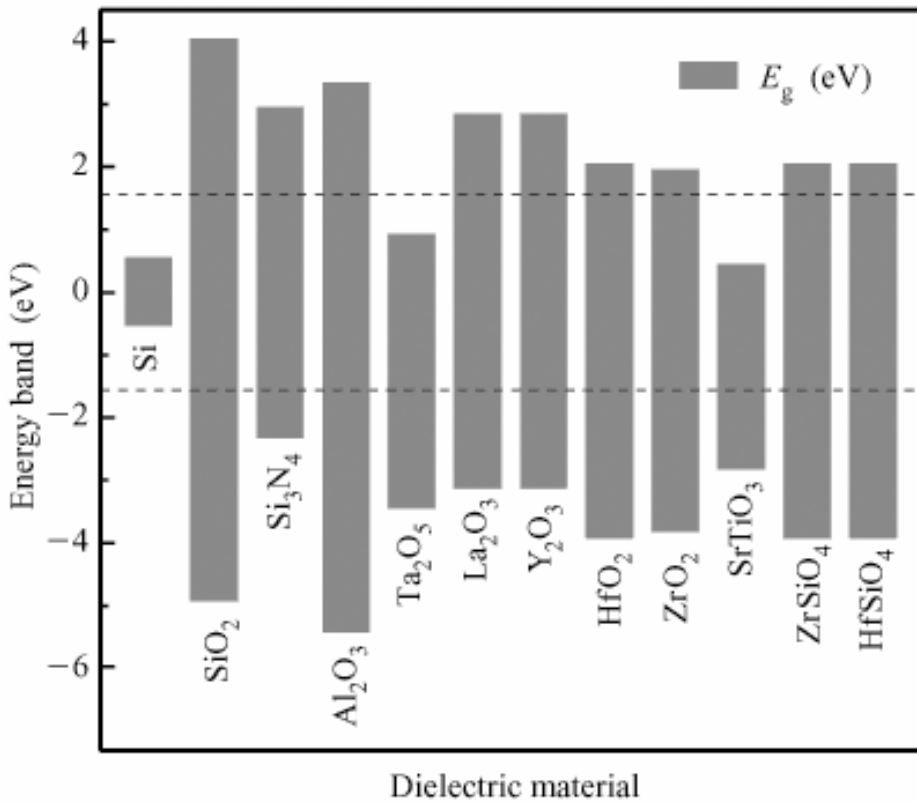


Figure 1-3: Bandgap and band offset comparison for various dielectric materials. [24] bonding. Elements having greater magnitude free energies than silicon will not readily give up oxygen to form SiO_2 when in contact with Si.²⁶ Table 1-3 lists the Gibbs free energies for various metals that form potential alternative high-k oxides.²⁶ Ta, Mo, and W have been ruled as unstable in contact with silicon because their energies of formation are less in magnitude than silicon and thus will give up oxygen to the silicon, and also tend to form silicates that will hinder the dielectric constant and equivalent thickness of the stack.

Further considerations must be taken into account because this table only shows the values for systems in equilibrium. However, during deposition or formation of devices, rarely is the system at a true equilibrium. Therefore, other reactions could occur, so a

good understanding of the kinetics behind the deposition or growth and processing steps is key in predicting non-equilibrium products.⁹

Table 1-3: Gibbs free energy of formation for potential alternative high-k dielectrics.

Metal	$-\Delta G_f (10^{-22} \text{ kcal/O atom})$ of metal oxide	Expected oxidation product of metal silicide on silicon
Si	1.70	
Ta	1.52	$\text{SiO}_2/\text{TaSi}_2/\text{Si}$
Mo	0.88	$\text{SiO}_2/\text{MoSi}_2/\text{Si}$
W	1.01	$\text{SiO}_2/\text{WSi}_2/\text{Si}$
Y	2.40	$\text{Y}_2\text{O}_3\cdot\text{SiO}_2/\text{Si}$
La	2.26	$\text{La}_2\text{O}_3\cdot\text{SiO}_2/\text{Si}$
Zr	2.06	$\text{ZrO}_2\cdot\text{SiO}_2/\text{Si}$
Hf	2.16	$\text{HfO}_2\cdot\text{SiO}_2/\text{Si}$

Film Morphology and Interface Quality

To avoid high-leakage paths due to grain boundaries, single crystalline or amorphous films are desired. Grain boundaries also promote the diffusion and leaching of dopants from the channel when thermally processed. However, Al_2O_3 is the only single-metal oxide that does not have a preferable crystalline phase under normal processing conditions. Single-crystal oxides with excellent interface structure can be grown using molecular beam epitaxy. However, this process is extremely slow and requires ultra-high vacuum conditions resulting in very low throughput.¹ Ultimately, amorphous barrier layers may have to be used at the interfaces of the dielectric even if it will hinder the benefits of using that high-k dielectric.

Implementation and Process Compatibility

Ultimately whatever material that is chosen as the replacement for silicon dioxide as the gate dielectric must be able to be fit into the large scale production scheme the micro-electronics industry runs on. Thus, additional processing steps or a hindrance to

throughput are unacceptable. The new material must be able to be implemented into the fabrication line with as little equipment and process flow changes as possible.

Reliability

Finally, the reliability of devices using the new gate material must be proven. The devices must meet stringent ten year lifetime standards set by industry.¹ These tests use higher voltages than normal operating voltage to stress the devices until breakdown conditions occur. This allows for lifetime estimates under actual working conditions to be extrapolated. To date, few reports have been generated of this nature and additional work must still be conducted. Further issues with threshold voltage shifts during operation must also be considered. Stability of the threshold voltage will ensure repeatable response of the device. If the threshold shifts too far, the device will cease to function as the operating voltage being used is not sufficient to operate the gate.

Hafnium Oxide Properties

One of the most promising materials currently being studied is HfO₂. Table 1-4 lists some of the properties of this dielectric.^{24, 27-28} Full ternary phase diagrams for the Hf-Si-O system have not yet been reported. However, similarities to the well studied Zr-Si-O system have been shown.⁹ Both metals are from the same family of the periodic table and exhibit the same crystal structure and preferred equilibrium compounds. Furthermore, due to the large negative free energy of formation for Hf-O bonds, hafnium metal has the ability to pull oxygen from SiO₂ thus limiting interfacial formation. For these reasons, Hf and its subsequent oxide and oxy-nitride will be used for this study.

Table 1-4: Various properties of HfO₂.

Property	Value
Dielectric constant	20-30
Band Gap	6 eV
Conduction Band Offset	2.8 eV
Crystallization temperature	450-500°C
Crystal Structure	Monoclinic
Thermal Stability w.r.t. Silicon	950°C

Hafnium Oxide Research

Over the past three years, many groups have been focusing their research efforts on HfO₂ and trying to use various methods for improving its performance as a gate dielectric. The interface quality between silicon and the dielectric is highly dependent on the deposition and annealing processes used. B. Y. Park *et al.*²⁹ grew HfO₂ thin films with thicknesses from 27-55 Å on hydrofluoric acid-treated Si wafers at a temperature of 200°C by chemical vapor deposition. They noted that the initial film growth was controlled by fast oxidation of the Si wafer. The Hf concentration in the film increased with deposition time. The films were post-annealed in N₂ at 800°C. Upon annealing the film separated into two distinct layers having approximate dielectric constants of 5.6 and 9.3 respectively. Equivalent thicknesses of 19 Å were reported for the thinnest layers. The incorporation of Si into the depositing HfO₂ film must be controlled if equivalent thicknesses of ~10 Å or less are to be realized.

Using reactive DC magnetron sputtering, L. Kang *et al.*³⁰ formed HfO₂ films with physical thicknesses of 45 Å. The sputtering was done at room temperature in a modulated O₂ flow to control the interface qualities and to suppress the additional growth of an interfacial layer. The deposition was followed by an ex-situ anneal at 500°C in N₂ ambient for 5 min. Pt was used as the gate electrode. They reported an equivalent

thickness of \sim 13.5 Å. The leakage currents for the films were about 1×10^{-4} A/cm², which is four orders of magnitude less than that for an equivalent SiO₂ film. Hysteresis values of <100 mV were also obtained. This study shows that HfO₂ can be successfully used as an alternative gate dielectric under the right processing conditions. However, thinner equivalent thicknesses will be required for future technologies.

S. W. Nam *et al.*³¹ studied the effect of annealing ambient on reactive DC magnetron sputtered HfO₂ films. First, Hf metal was pre-deposited as an oxidation barrier, and then a thin HfO₂ layer was deposited at room temperature in Ar and O₂ ambient from an Hf metal target. The Hf metal layer helps to form HfO₂ by reducing the native oxide on the substrate. Samples were annealed at temperatures ranging from 500-900°C in both N₂ and O₂. The as-deposited films were amorphous in structure. Formation of a monoclinic phase was reported for annealing temperatures above 650°C and at greater than 800°C an orthorhombic HfO₂ structure emerges. The equivalent thickness values obtained in this study were calculated to \sim 19 Å for N₂ annealed HfO₂ films and \sim 28 Å for O₂-annealed films. The increase in equivalent thickness is believed to be due to the increase of the thickness in the interfacial oxide layer.

Nitride Barrier Layers

Attempts have been made to control the interface by using barrier layers. P. D. Kirsch *et al.*³² investigated the electrical properties of HfO₂ films on nitrided and un-nitrided Si substrates. The samples were prepared by magnetron sputter deposition of Hf metal and subsequent oxidation on both bare silicon and on wafers which had been exposed to NH₃ for 30 s at a temperature of 700°C. The samples were annealed in N₂ ambient for 10 s at 600°C. After annealing, MOS capacitors with HfO₂ thicknesses of \sim 50 Å were fabricated using TaN as the gate electrode. The nitrided samples

demonstrated leakage current densities two orders of magnitude less (4×10^{-5} A/cm²) than the non-nitrided samples (4×10^{-3} A/cm²) and an increase in capacitance of 15%. Equivalent oxide thickness for the 50 Å films was estimated to be 10.6 and 11.7 Å with and without SiN_x, respectively. Therefore, use of a nitride barrier layer can improve the leakage and capacitance characteristics of HfO₂ gate dielectrics. However, the nitride interface layer degrades mobility and capacitive response due to additional interface traps.

Other Novel Approaches

Other novel approaches have been used to tailor the electrical characteristics of HfO₂. H. Lee *et al.*³³ examined using Dy doping to control oxygen vacancies in the film. Since the electronegativity of Dy is lower than that of Hf, the concentration of oxygen vacancies in the Dy-doped HfO₂ was lower than that of their control HfO₂ and thus yielded leakage current densities over three orders of magnitude smaller than the control. Furthermore, the large atomic radius of Dy was predicted to reduce the leakage current through the dielectric due to a packing density effect.

In a study by H. Yu *et al.*,³⁴ Al₂O₃ was added to HfO₂, and a range of compositions were compared in an attempt to control and model the energy gap and band alignment for the dielectric on Si. Band gap and offset values for various compositions ranging from pure HfO₂ to pure Al₂O₃ were carried out using high-resolution XPS. The Al 2p, Hf 4f, O 1s core levels spectra, and O 1s energy loss spectra all showed continuous changes with the variation of the HfO₂ mole fraction. From this data, they were able to model the band gap and band offsets for the (HfO₂)_x(Al₂O₃)_{1-x} system. This system is important because of the higher temperatures at which the film will remain amorphous. It has been shown that Al concentrations of greater than 31.7% will result in

crystallization temperatures between 850 and 900°C, which is about 400°C higher than that for HfO₂.

Various studies have also investigated the interface layer of the HfO₂ dielectric to the gate electrode. One of the approaches used barrier layer formation by nitriding the top surface of the HfO₂ before electrode deposition creating a thin Hf_xN_y layer so B doped poly-Si gates could be used.³⁵ A similar study was conducted using Al₂O₃ as the capping layer.³⁶ Both types of barrier layers were shown to reduce leakage and improve the stability of the doping levels in the gate.

UV Assisted Oxidation

Ultraviolet (UV) radiation has been shown to assist in the thermal oxidation of silicon.³⁷⁻³⁹ For temperatures around 850°C, thermal oxidation of silicon in dry O₂ is on the order of 2Å/min even though the supply of O₂ from the gas phase to the SiO₂ surface is plentiful. This is due mainly to the high activation energies of >1.5 eV required for O₂ diffusion through the oxide to react with the underlying silicon. By using a UV source producing photons with wavelengths of less than 200 nm, the energy of the photons is great enough to split O₂ bonds, thus forming more reactive species. The following equations (1-3..1-6) show the reactions that take place in the gas phase.⁴⁰ M is a third body.



Furthermore interaction of photons with wavelengths less than 254 nm will cause the ozone species to break apart as shown in equation (1-7).



Within the bulk, photoinduced transitions occur from the conduction band of Si to the conduction band of SiO_2 (3.15 eV) and from the valence band of Si to the conduction band of SiO_2 (4.25 eV) when the sample is irradiated.⁴¹⁻⁴² Therefore during irradiation of UV, the SiO_2 layer is supplied with both atomic oxygen from the gas interface and electrons from the Si/ SiO_2 and thus the probability of ionization of the oxygen species is enhanced.

The oxidation rate of light-enhanced thermal oxidation of silicon at temperatures above 740°C can be explained using the photo-enhanced Deal and Grove model.^{38,43} Below this temperature, the Carera and Mott model demonstrated by Ishikawa *et al.* better explains the initial 70 Å of film growth and thereafter the Deal and Grove model seems to fit.⁴⁴ In this model, the oxidants are assumed to absorb on the surface creating vacancies and thereby encouraging electrons to tunnel through the oxide to fill them. The charged species then move under the influence of the space charge through the oxide to the oxide/silicon surface.

Current work is being conducted on the oxidation of zirconium metal to form dielectric films.⁴⁵⁻⁴⁹ Ramanathan *et al.* deposited thin 20-30 Å films of Zr at room temperature onto peroxide washed Si substrates. The washing process leaves a thin amorphous SiO_2/SiON layer. The films were then exposed to Hg vapor lamps emitting primarily at wavelengths of 185 and 254 nm. They have shown that the light interacts with O_2 to form atomic O and ozone enhancing the oxidation rate of Zr enabling formation of a stoichiometric metal oxide up to about 55 Å thick after 90 minutes at room

temperature.⁴⁶ They compared these films to ones oxidized without the use of UV assisted annealing. The films oxidized without UV demonstrated severe frequency dispersion in both the accumulation and depletion regions of the capacitance-voltage plots. Using electron energy loss spectroscopy and chemical mapping of the oxygen concentration, they were able to explain that the cause of the poor electrical characteristics resulted from a high concentration of oxygen vacancy defects. The films oxidized using UV showed very little frequency dispersion and had a more constant oxygen distribution through the thickness of the layer.

In another study Ramanathan *et al.*⁴⁷ proposed that the oxidation of Zr films by the UV-ozone method is expected to be self-limiting at room temperature. To verify this, capacitors were fabricated by oxidizing ~20 Å Zr films for 60 min and 90 min. Both sets of samples were subjected to a forming gas anneal at 400°C for 30 min. Then capacitors were made from the films by using Pt electrodes. Capacitance-voltage curves were measured at 100 KHz from both samples and yielded nearly identical results. This implies that the oxidation is self-limiting for the thickness range investigated and also shows that lengthy room temperature oxidations do not result in significant growth of interfacial SiO₂. Further analysis in this study compared the hysteresis of reported values for ZrO₂ from other groups to the films they formed by the UV-ozone oxidation of Zr. They were able to obtain films with ~100 mV hysteresis for physical thicknesses of 50 Å. Their value was markedly better than the 200 mV hysteresis reported by Wang *et al.*⁵⁰ Electrical traps in the zirconia films are proposed to be the cause of the hysteresis.⁵¹ UV-ozone oxidation eliminates many of the oxygen defects which contribute to the

hysteresis. Ultimately films with <15 mV are desired for future implementation into device structures.⁵²

Motivation

Even after years of research in an attempt to find a suitable replacement dielectric for SiO₂, more research is still needed to understand the role of the interface, to tailor the chosen dielectric, and to insure reliability.

This three part work first examines the interfacial layer formation of pulse laser deposited (PLD) HfO₂ ultra-thin films under different processing conditions. The role of temperature and oxygen deposition pressures was studied. By understanding the nature of the interface and how it is formed we can better control it to tailor the ultimate properties of the film.

The second portion of the work combines the use of UV-assisted oxidation and the incorporation of nitrogen into the films during deposition to produce higher quality films and interfaces. The use of UV radiation lowers the temperature required to fully oxidize the thin metal films and limits the oxygen vacancy and non-stoichiometry issues typically encountered in PLD deposition of oxides. The nitrogen incorporation during deposition limits the diffusion of oxygen to the interface thus slowing interfacial oxide growth.

Finally, aluminum was added to the films during deposition to increase the crystallization temperature in an attempt to maximize the dielectric constant while minimizing the leakage current. Initial studies of the composition and structural properties of the films, as well as, the electrical characteristics were conducted after deposition and UV-oxidation processes were concluded. The samples with the lowest concentration of aluminum were subsequently heat treated at 500, 700 and 900 °C to determine the crystallization temperature of the films.

CHAPTER 2 EXPERIMENTAL PROCEDURES

Deposition Setup and Equipment

All the thin film samples in this work were deposited using a pulsed laser deposition (PLD) technique in an ultra-high vacuum compatible chamber utilizing an excimer laser system. The chamber has been modified for use with an ultra-violet (UV) lamp array for irradiation during deposition and for in-situ post-deposition (PD) anneals.

UVPLD System

A Neocera brand single chamber vacuum system was used for all the sample depositions. Figure 2-1 shows a schematic of the system along with laser and the optics setup used for the pulsed laser depositions. Due to the lack of a loadlock for the system, the chamber was backfilled with nitrogen to bring it to atmosphere each time a sample was loaded/unloaded. The chamber pumping system consists of a Pfeiffer MD-4T oil free diaphragm roughing pump backing a Pfeiffer TMU 230 turbo pump. Vacuum levels of 1×10^{-6} Torr can be reached within an hour, 1×10^{-7} Torr within twenty four hours, and 1×10^{-8} Torr within 3 days. Addition of a liquid nitrogen cooling to the system allows for 1×10^{-8} Torr within 24 hours. Higher vacuum levels are possible if a loadlock system is added and thus eliminating the viton seals on three of the ports.

Samples were mounted on a 2" Neocera brand stainless steel resistive heater capable of 850°C and positioned vertically in the chamber. The system has a variable controller to regulate the substrate temperature and has been calibrated within ± 5 °C. This system includes a computer controlled multi-target carousel available for

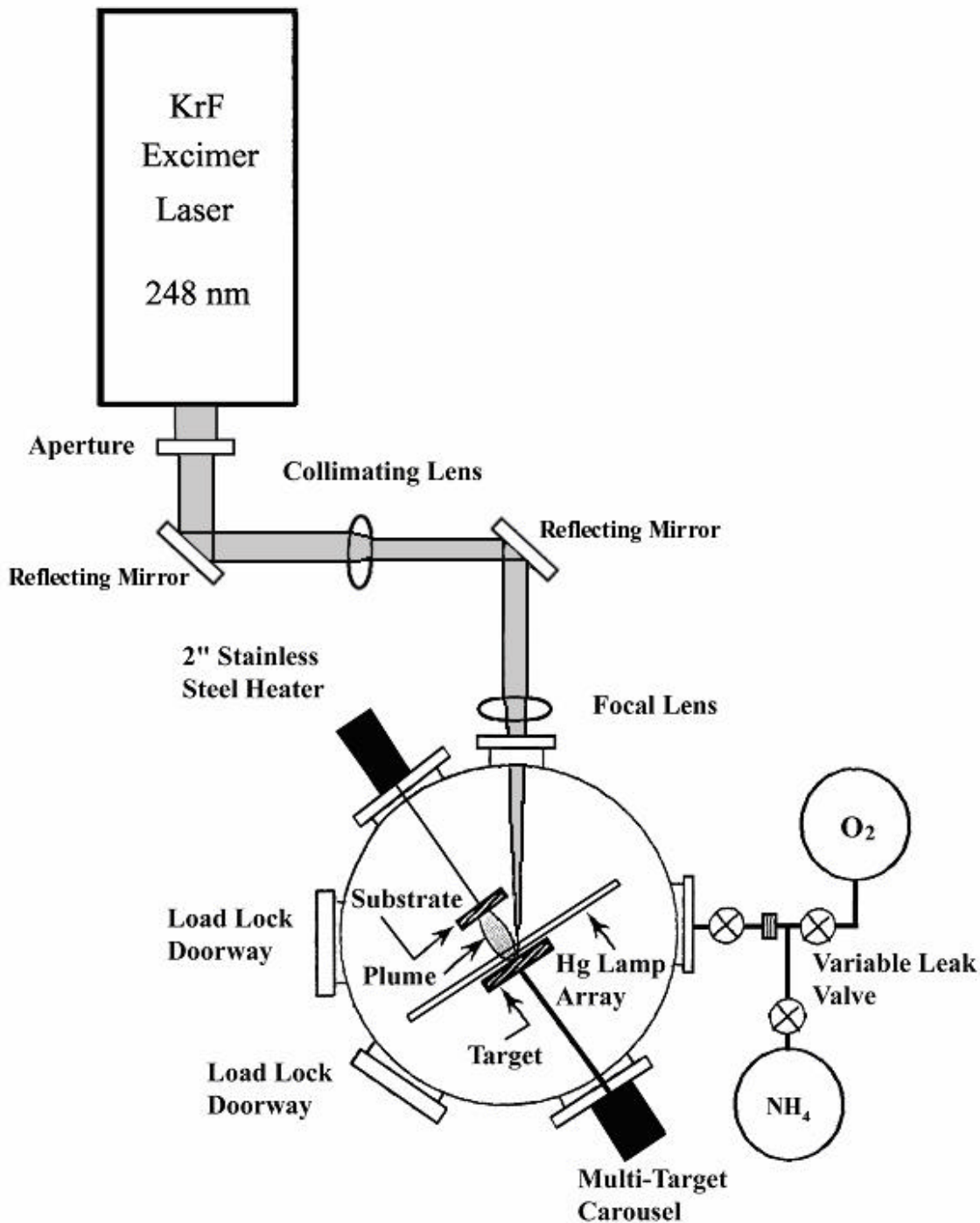


Figure 2-1: UVPLD system with excimer laser and optics setup.

depositions of up to six different materials for multilayer/mixture or superlattice experiments. This carousel was used for the third portion of the experiments. An array of 4-11" u-bend low pressure Hg lamps from Atlantic UV was added to the conventional

PLD setup to convert it into a UVPLD apparatus. The lamps were placed on a rack in a plane parallel to the surface of the substrate halfway between the substrate and the target. Figure 2-2 shows the placement of the lamps and target. Highly sensitive Varian brand leak valves were used to control input of ultrapure gases into the chamber allowing for a wide range of deposition ambients and pressures.

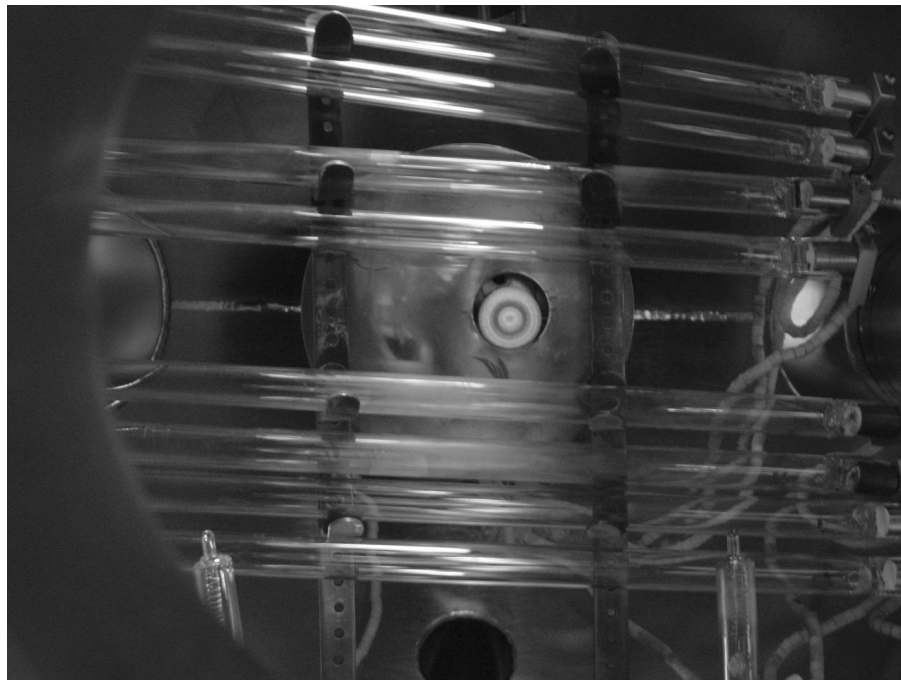


Figure 2-2: Photograph of UV lamp placement in the chamber.

Laser Ablation

Many techniques are available for the deposition of thin films onto a substrate, however pulsed laser deposition has several key advantages that make it an ideal small batch research tool. PLD provides near-stoichiometric transfer of molecules from the target to the substrate, rapid testing of many different materials, and offers a wide range of applications, though it does not lend itself well for industrial scale production.

The ablation process itself is characterized by an input of energy from the laser to a given target material. Figure 2-3 shows a schematic of the energy distribution at the

target surface during ablation. The total energy for the system is represented in equation 2-1.

$$E = E_r + E_p + E_d + E_c \quad (2-1)$$

E = incident energy

E_r = reflected energy

E_p = plasma plume energy

E_d = energy of disintegration

E_c = energy absorbed by the cavity wall

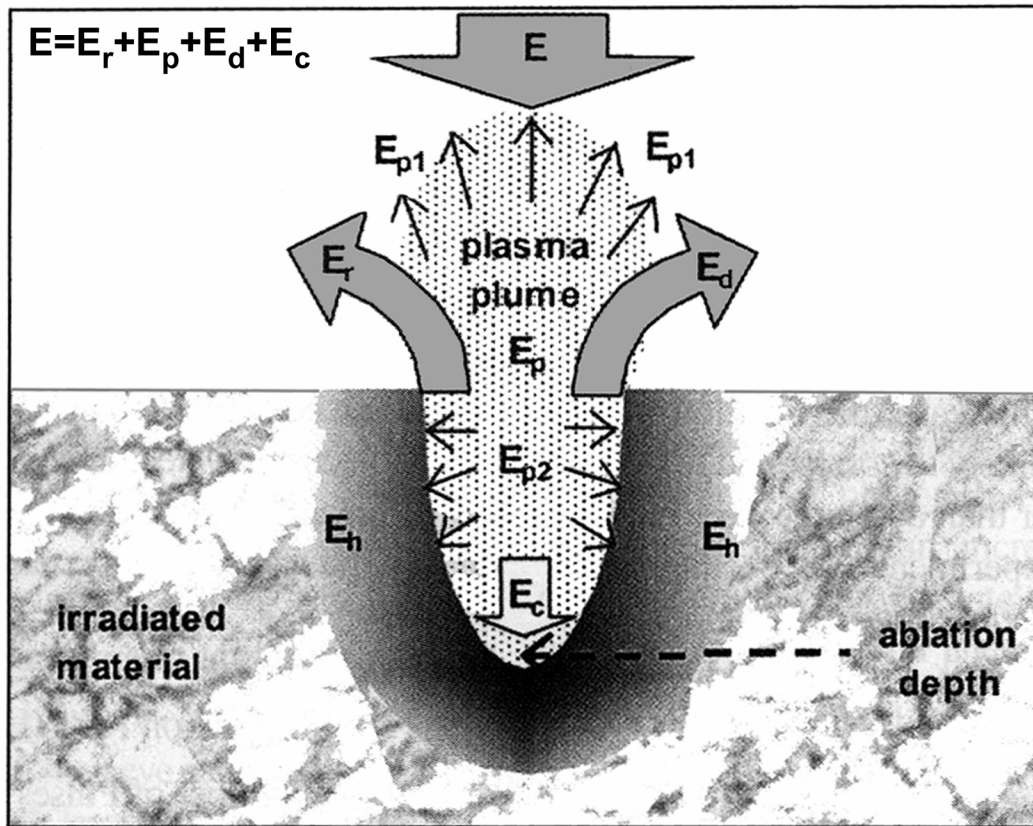


Figure 2-3: Laser energy distribution during target ablation.

There are additional factors related to the laser energy that play an important role in surface response to pulse energy. The incident pulse energy must exceed the ablation threshold energy for the material for ablation to occur. If the pulse energy is less than the ablation threshold, material will not be physically removed from the surface (i.e., E_p and E_d tend to zero), but that energy will be absorbed by the cavity wall (E_c) as heat, which

can be useful for laser annealing applications. The degree to which the target material is ablated depends on the extent the energy is exceeded. If excessive energy is used, large particulates from the target can be blown off. This is unwanted for high-quality films. All experimentation in this study was carried out at an energy value greater than the ablation threshold but low enough to minimize particulate ablation.

Laser System

A Lambda Physik LPX 305 I KrF excimer laser (s/n 9412 E 4188) was used to deposit all the samples in the following experiments. This model laser uses a pulsed mode delivering 25 nanosecond duration square shaped wave pulses at frequencies from 1-50 Hz and output energies from 10-1100 mJ yielding ultimate fluences from 0.1-4 J/cm² depending on optics used. The laser is fired or triggered by either an internal computer module near the laser or from a remote external computer placed near the deposition chamber, which also controls the multi-target carousel.

Excimer lasers function on the principle of stimulated photoemission of gases within a set cavity. This laser uses a mixture of Kr, F, and a buffer gas, typically Ne or He. High voltages ranging from 16-23 kV elevate electrons in the Kr and F atoms into excited states causing excited KrF* complexes to form. Upon their decay, 248 nm single wavelength radiation is given off. The cavity is designed such that conditions of stimulated emission of coherent radiation occurs and thus subsequent amplification of the radiation is achieved resulting in high energy laser output in a pulsed mode.

A series of lenses and an aperture are used to select the highest energy portion of the beam, direct, collimate, and focus the pulse until it impinges the sample. For the PLD system, the laser beam first passed through a 2 cm x 1 cm aperture to select the center portion of the spot from the laser. This eliminates the lower energy diffuse side portions

of the spot and gives the initial rectangular spot shape. Due to positioning of the chamber, the beam is then reflected using a UV mirror optic placed at 45° to the beam path. Once reflected, the incident beam is passed through a collimating lens to keep the radiation from diverging due to scattering as it passes through the ambient air. One more mirror is used to reflect the beam to the chamber. The beam then is passed through a focusing optic with a 30 cm focal length placed just outside of the chamber. The beam enters the chamber through a fused silica window port rated for use with excimer radiation. This window passes 90% of 248 nm radiation.

A Gentec Sun Series EM1 energy meter (s/n 86052) was used to determine the fluence reaching the sample. The laser was operated at the lowest energy possible, the focusing optic was removed, and the meter head was placed inside the chamber. Lower energies had to be used as the meter head has a low maximum energy tolerance before damage to the surface will occur. Averages of 20 pulses were used to record the energy of the spot impinging the meter head. An additional 10% of the energy was subtracted to take into account the focusing optic. By taking the energy value obtained and dividing by the area of the spot on the target, precise calculation of the laser fluence was possible and then scaled with the laser energy settings used for the experiments.

The laser ablation spot impinging the target had dimensions of 2 x 5 mm, maintaining the shape of the rectangular aperture used at the start of the beam path. By moving the focusing optic to a position of 35 cm from the target, the target is past the focal length of 30 cm of the optic and thus is in the imaging plane region allowing for conservation of the spot shape. By placement of the lens such that the focal point coincides with the target surface, smaller spot sizes and greater fluence can be obtained.

However, it was unnecessary because the threshold value for laser ablation of the oxide materials and metals used in our experimentation were sufficiently exceeded with the current optics setup. Having a larger spot size also gives more uniform ablation of the target so trenching does not occur as rapidly. Another argument for not using the focal point for ablation arises from the irregular shape of the spot which results. The spot geometry is shifted to an elongated oval shape with two additional satellite peaks to either side of the main ablation spot. The energy of the main spot was characterized by a Gaussian type distribution while the satellite peaks were of lower energies based on burn paper tests. All of the samples in this work were deposited using the previously mentioned laser and optics setup.

Experimental Setups and Samples

There are three main areas that comprise the work discussed in this dissertation. This section delineates the differences in the samples and gives the motivation behind each portion of the experiments.

Interfacial Layer Formation and Growth

In this initial portion of the experimentation, the formation and characteristics of the interfacial layer were investigated. Ultrathin HfO₂ samples were deposited on silicon by ablating a high purity HfO₂ target in a conventional PLD chamber under different oxygen ambients and substrate temperatures. The main goal for this investigation was to determine the nature of the interfacial layer and the factors that control its formation and growth. The conditions for deposition are shown in Table 2-1. The samples were investigated by variable angle spectroscopic ellipsometry, x-ray reflectivity, and angle resolved x-ray photoelectron spectroscopy. These techniques will be discussed later in this chapter.

Table 2-1: Conditions for growth of ultra-thin HfO₂ films.

Sample ID#	Temp. °C	Pressure Torr
Hf11		1x10 ⁻⁴
Hf12	200	1x10 ⁻³
Hf13		1x10 ⁻²
Hf14		1x10 ⁻⁴
Hf15	400	1x10 ⁻³
Hf16		1x10 ⁻²
Hf17		1x10 ⁻⁴
Hf18	600	1x10 ⁻³
Hf19		1x10 ⁻²

UV Assisted Oxidation and Nitridation of Hafnium Films

The second portion of this dissertation examines both the effect of UV oxidation of hafnium metal thin films and the effect of nitrogen incorporation into the films. Four conditions were used and are denoted in Table 2-2. Half of the samples were deposited in ambient vacuum levels of 1×10^{-6} Torr while half were deposited in 1×10^{-2} Torr of ammonia. Half the samples were oxidized in 300 Torr of oxygen at 650 °C without the aid of UV radiation while the other half were oxidized for 30 minutes with the lamps on under the same temperature and pressure used for the non-irradiated samples. Target film thicknesses of 40-50 Å were obtained after oxidation for all the samples. This experiment was repeated three times to verify reliability and repeatability of the process. The goal of this portion of the experiments was to improve the electrical characteristics and film stoichiometry while using lower processing temperatures. Lower deposition temperatures usually result in poorer quality films when using PLD to deposit them, however by depositing a metal then oxidizing it with a post-deposition (PD) annealing step higher quality films can be realized.

In an attempt to incorporate a significant amount of nitrogen into the films, higher temperature depositions carried out at 650 °C. A set of four samples were produced, all

of which were deposited in 1×10^{-2} Torr of ammonia. Half were deposited with the use of UV radiation during deposition and half were deposited with the lamps off. Then half of the samples were annealed in UV during the oxidation step. Table 2-3 shows the sample identification and conditions for this set of samples.

Table 2-2: Growth and postdeposition conditions for UV oxidation of Hf metal ultra-thin films.

Sample ID #	Deposition Pressure Torr	Anneal Conditions
H2	1×10^{-6}	UV
H3	1×10^{-6}	No UV
H4	1×10^{-2} Ammonia	UV
H5	1×10^{-2} Ammonia	No UV

Table 2-3: High temperature Hf metal deposition and oxidation conditions.

Sample ID #	Deposition Conditions	Anneal Conditions
HN1	UV	UV
HN2	No UV	UV
HN3	No UV	No UV
HN4	UV	No UV

UV Assisted Oxidation and Nitridation of Hafnium/Aluminum Alloy Films

Finally, to increase the crystallization temperature of the films aluminum additions were studied. This set of experiments used the carousel with two high purity targets of Hf and Al. The pulse ratio between targets was varied to obtain different film stoichiometry. The sample conditions are listed in Table 2-4. Half of the samples were deposited in ammonia to incorporate nitrogen into the structure as was done in the second set of experiments. After electrical characterization, the samples were annealed at 900 °C in N₂ to study the detrimental effect of high temperature anneals and to determine if the aluminum additions will suppress crystallization.

Table 2-4: Growth and annealing conditions for Hf/Al metal films.

Sample ID #	Pulse Ratio	1×10^{-2} Torr Ammonia
AH1	1 Al: 1 Hf	No
AH2	1 Al: 2 Hf	No
AH3	1 Al: 3 Hf	No
AHN1	1 Al: 1 Hf	Yes
AHN2	1 Al: 2 Hf	Yes
AHN3	1 Al: 3 Hf	Yes

Experimental Characterization Techniques

Many techniques are available for characterizing the structure, morphology, stoichiometry, and electrical properties of thin films. This section reviews the techniques used to compare the samples in this dissertation to delineate the effect of temperature, pressure, UV oxidation, nitrogen incorporation, and aluminum additions.

Variable Angle Spectroscopic Ellipsometry

Variable angle spectroscopic ellipsometry (VASE) is a simple, yet very powerful, nondestructive analysis tool for determination of thickness in thin film multilayered structures. Optical properties such as index of refraction and the extinction coefficient can also be obtained. This technique is best suited for flat planar materials with thicknesses ranging from 1-1000 nm having low surface roughness, which makes it an invaluable tool for analysis of the thin film samples in this work.

A J. A. Woollam brand M-88 variable angle ellipsometer was used for sample analysis. VASE operates by reflecting a collimated beam of light of known polarization from a Xenon lamp off of the surface of the sample to be analyzed. A second polarizer is used to determine the polarization shift resulting from interaction with the sample. The angle of incidence and wavelength of light used are extremely important factors

dependent on the thickness and type of sample being analyzed. For dielectric films, an incidence angle of 75° is optimal.

All electromagnetic phenomena are governed by Maxwell's equations and thus certain mathematical relationships can be determined when light encounters boundaries between different materials. Ellipsometry uses Snell's Law and Fresnel reflection relationships to determine delta and psi for the film. The software package that runs the equipment plots the psi and delta values obtained.

A model is then needed to interpret the data. It is best if information such as estimated thickness and density are known. The software has a database of material properties for use in the models. Various mixture routines are available for multi-component films. The software takes the initial information the user inputs and iterates through a routine until the model has the lowest least square fit.

X-ray Reflectivity

X-ray reflectivity (XRR) measurements were made with the assistance of a Panalytic MRD X'Pert system. XRR is another non-destructive optical characterization technique that yields similar data to that of VASE. XRR will verify the VASE result and can be used to better fit the models used to interpret the raw data obtained from both analysis techniques. X-ray reflectivity plots provide information on the thickness, roughness, and density of a given material. Figure 2-4 demonstrates an example of a typical plot showing how the features of an acquired spectrum relate to the various data that can be extracted from the spectrum. Similar to VASE, this technique is well suited to smooth flat samples with low surface roughness and is most sensitive to samples in the 10-400 nm thickness range.

This particular x-ray based analysis technique works in the traditional θ - 2θ geometry and scans angles from subcritical to a few degrees. The detector records the intensity of the radiation reflected from the surface of the sample. At angles of less than the Brewster's angle, also known as the critical angle, total reflection occurs. At angles greater than the Brewster's angle, the radiation begins to interact with the surface and interfaces within the sample. This interaction is governed by Snell's law and Fresnel's relationships similar to VASE. The constructive and destructive nature of the x-rays at a particular angle generates the fringe pattern in the detected signal. The raw data are modeled using a user-input system whereby the density, roughness, thickness, and absorption coefficients can be changed until a suitable fit is obtained.

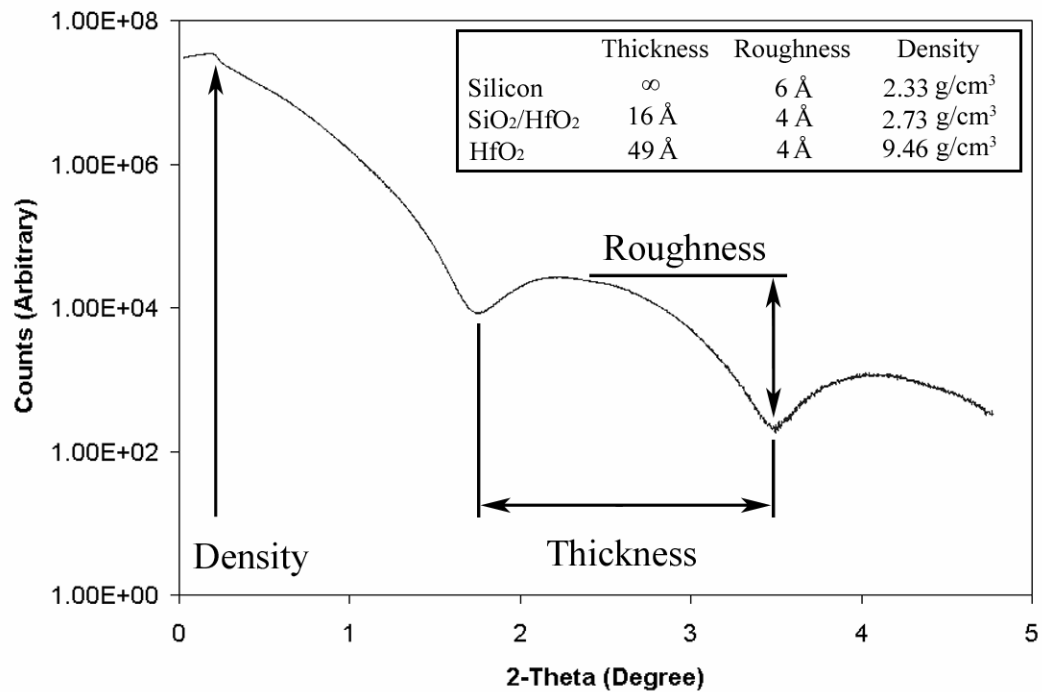


Figure 2-4: Typical XRR plot showing which film properties most influence various features.

X-ray Diffraction and Glancing Incidence X-ray Diffraction

X-ray diffraction (XRD) is an invaluable tool that provides phase analysis as well as strain, grain size, epitaxial quality, phase composition, preferred orientation, and defect structure. This technique is nondestructive and noncontact and can be used for films greater than 50 Å. The basic equipment setup is shown in Figure 2-5. X-rays (typically Cu K_α) impinge the sample at a specific angle. The scattering of the X-rays by the sample atomic planes produces constructive and destructive interference. The condition for constructive interference from planes with a given spacing is given by Bragg's Law shown in Equation 2-2. When this condition is met, peaks in the intensity detected will occur.

$$\lambda = 2d_{hkl} \sin\theta_{hkl} \quad (2-2)$$

λ = wavelength of the x-ray radiation

d_{hkl} = d-spacing between (hkl) planes

θ_{hkl} = angle between the atomic plane and the incidence direction

For single crystal films, there is only one specimen orientation that will satisfy the conditions for Bragg diffraction for each family of planes, so careful alignment procedures must be taken. However, with thin films that are polycrystalline, fiber textured, or exhibit preferred orientations several families of planes may contribute to a diffraction system. X-ray diffraction data for this dissertation was obtained with a Panalytic X'Pert MRD diffraction system. Once an x-ray diffraction pattern is generated, positive phase identification can be achieved by comparing measured d-spacing from the diffraction pattern (and their integrated intensities) to a known JCPDS powder diffraction standard. Additional information such as grain size can be generated from the full width at half max of the peaks.

Normal XRD mode of operation could not be used for the thin films produced in this dissertation. The high intensity peaks from the underlying silicon substrate masked the weak signal from the film. Glancing incidence x-ray diffraction had to be used in this case. In this setup, the incident angle of the x-ray system is fixed at a small value (typically from $0.250\text{--}1.000^\circ$) so only the surface of the sample is probed and the receiving slit is allowed to scan through a typical range for a conventional XRD 2θ scan. As a result, only planes that satisfy the Bragg condition with the additional constraint in place will produce peaks. In a polycrystalline sample with many orientations, this will still generate a representative x-ray diffraction plot, but with much higher surface sensitivity without any masking peaks from the silicon substrate. This method proved to be beneficial for several samples in this dissertation.

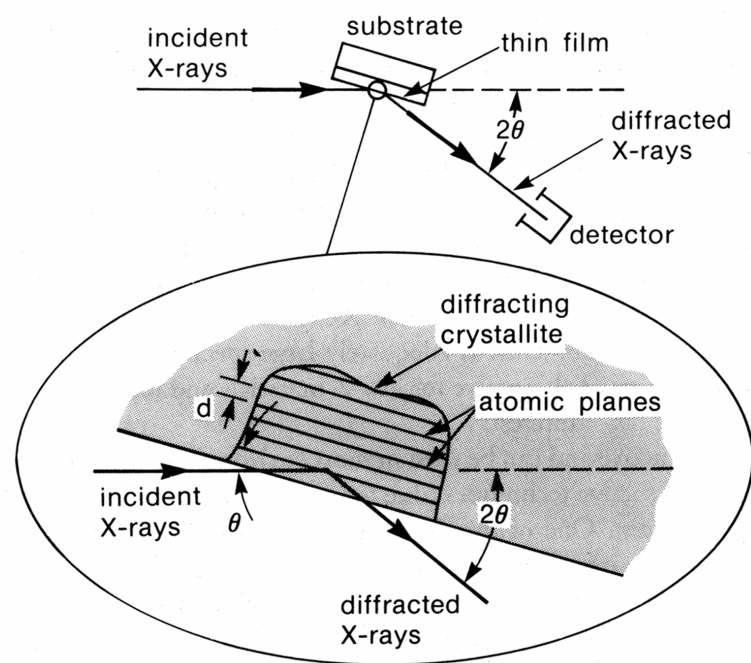


Figure 2-5: Typical XRD equipment geometry setup. [53]

X-ray Photoelectron Spectroscopy

X-ray photoelectron spectroscopy (XPS) is one of the most commonly used techniques for thin film chemical analysis along with Auger electron spectroscopy (AES). This surface sensitive technique provides elemental as well as bonding environment information. Elemental analysis can be obtained for all elements except hydrogen and helium. XPS spectra were collected using a Perkin Elmer 5100 installation using Mg K_a radiation (1486.6 eV) at takeoff angles from 45-90°.

This technique works by impinging high energy photons at a specific angle to the surface. The photons cause electrons from the atoms in the sample to ionize and form photoelectrons. The kinetic energy of the electron is measured and used to calculate the binding energy based on Einstein's Photoelectron law given in Equation 2-3.

$$\text{KE} = h\nu - \text{BE} \quad (2-3)$$

KE = Kinetic energy
 $h\nu$ = Energy of incident photons
 BE = Binding energy

Each atom can be identified by the binding energies of its electrons. By comparing the ratios of photoelectrons from the different atoms along with the sensitivities for each a quantitative chemical analysis can be obtained. Compositional changes across the thickness of the thin film sample can be generated by one of two ways. The first is by using an argon sputtering gun which removes a portion of the sample from the surface at a set rate. The other, which was used in these experiments, is angle-resolved XPS, whereby different take-off angles are used and the data generated is compared. This allows for different interaction volumes of the sample to be probed to compare any differences that might occur through the thickness.

Atomic Force Microscopy

Atomic force microscopy measurements were made with a Digital Instruments brand Nanoscope III operating in both contact and tapping mode. This technique was chosen for its exceptional ability to produce topographic images of surfaces in three dimensions at high resolutions. Atomic resolution is attainable, if proper conditions are set. This technique is also perfectly suited to the insulating, low roughness samples created for this dissertation. In an atomic force microscope, a sharp tip is mounted on a flexible cantilever. A piezoelectric scanner moves the cantilever/tip assembly along the surface of the sample, while a laser reflecting off the end of the cantilever maps the topographical changes the cantilever senses. When the tip comes into close proximity of a sample surface, van der Waal forces repel the tip causing the cantilever to deflect, in contact mode the tip stays at a constant distance from the surface while in tapping mode a potential is applied at a specific frequency moving the tip near the sample surface at a certain cyclical rate. The typical operational setup for the AFM is shown schematically in Figure 2-6.

Electrical Characterization

A primary tool for indication of quality of thin film is the use of electrical characterization techniques. After deposition or processing of thin films, metal oxide semiconductor (MOS) devices were fabricated and measured. Typical preparation of the film included the deposition of platinum (Pt) contacts via DC magnetron sputtering. A shadow mask with an array of circular dots ranging from 25-500 μm was used to create dot arrays on the samples for the gate contacts. The backside contact was silver (Ag).

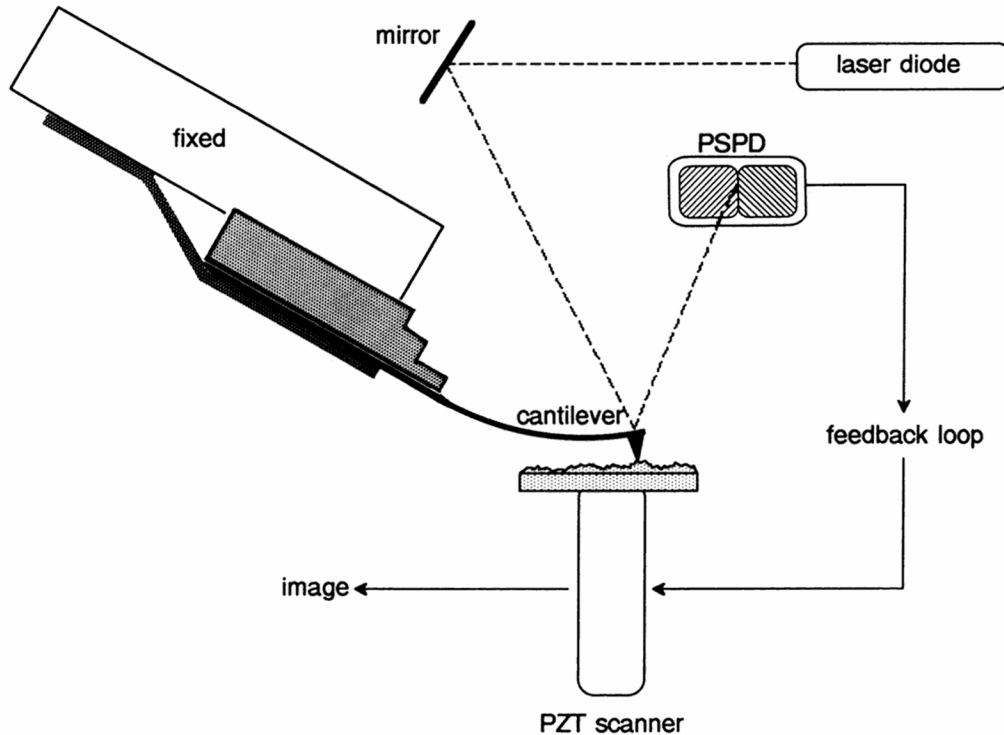


Figure 2-6: AFM operational setup showing laser detection of the cantilever deflection. [53]

The backside of the wafer was first abraded and swabbed with 1% HF so that clean silicon, without any native silicon dioxide, was present. It is of paramount importance to choose the proper metals for the dielectric film being measured and the type of silicon substrate that was used. If improper metals are chosen for a given setup, band alignment conditions may exist whereby non-ohmic contacts are created within the device. As an example, the backside metal contact on a p-type silicon wafer should have a work function greater than that of the silicon. If these conditions are met, there should be an ohmic contact, if not, the contact will be a rectifying Schottky contact. A schematic of a MOS capacitor fabricated for this dissertation is shown in Figure 2-7 demonstrating the testing setup used for these experiments. After the front side gate metallization was complete, samples underwent heat treatments in a conventional tube

furnace under a flowing forming gas atmosphere (4% H₂, balance N₂). Both current-voltage and capacitance-voltage measurements were taken once the MOS capacitors were formed.

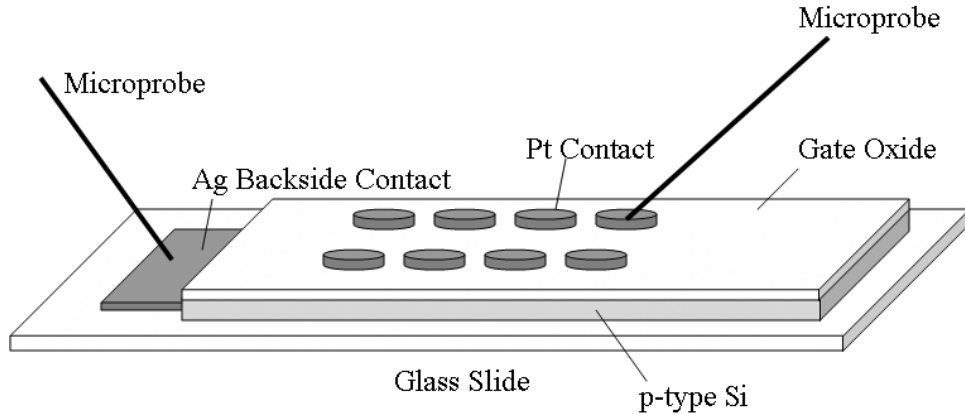


Figure 2-7: MOS capacitor setup used for CV/IV measurements.

Current-Voltage Measurements

Determination of the leakage current is an essential first step in analyzing an MOS device. Once MOS devices were fabricated, a Keithley Instruments Inc., KI236 source measurement unit (SMU) was used to measure the current flow through a device. The 236 SMU was attached to a pair of Signatone Inc, micromanipulators mounted on a probe station. Tungsten probes that were milled to produce a fine ~5 μm tip were fitted in the micromanipulators. The output of the SMU was connected to the micromanipulator in contact with the Pt gate while the input was connected to the backside Ag contact. This configuration is optimal for the determination of current leakage pathways directly below the device being measured (i.e., it avoids stray leakage paths). The current compliance threshold, a value that may not be exceeded by the machine, of 100 nA was input into the measurement parameters. Then a direct current bias sweep was conducted over a voltage range (from negative to positive) and the amount of current that passed through the MOS

structure was monitored. To reduce creation of bias induced defects, typically it is best to start at a small voltage sweep range so that it is possible to determine if the device is leaky before a wider voltage sweep range is implemented. The main goal of the leakage current measurement is to identify a high quality device that can be used for capacitance voltage measurements and to determine if excessive leakage is present that needs further investigation.

Capacitance-Voltage Measurement

Capacitance-voltage measurements serve as one of the most versatile and sensitive of all electrical characterization techniques. It is the ultimate tool for determining discreet differences in a MOS device that may serve as the final word in whether a given processing condition has resulted in a high enough quality device to apply to MOSFET applications. These measurements were carried out with a Keithley Instruments Inc. Win-82 measurement system. This system, as seen in Figure 2-8, is comprised of four main components working in unison. The Keithley 595 capacitor is used for simultaneous quasistatic low frequency measurements. The Keithly 590 capacitance meter is used for high frequency capacitance measurements at 100 kHz and 1 MHz. The Keithley 230 voltage source is used for static bias condition measurements. These three devices are wired into the Keithley 5951 remote input coupler, which serves to filter and relay the device data to and from the various pieces of equipment. Due to its ability to give detailed information about the quality of the MOS device, the Win-82 system will be discussed in Appendix A.

The output of a typical CV curve can be seen in Figure 2-9. There are several important features that should be noted. First, there are three main regions with respect

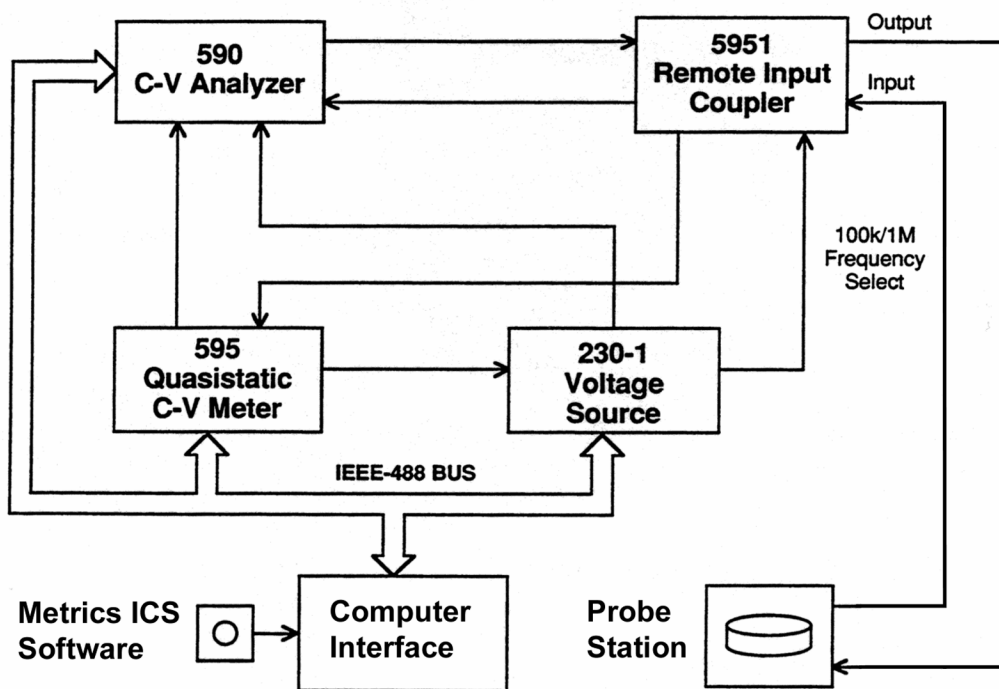


Figure 2-8: Kiethley Instruments Inc. Win-82 measurement system. Modified from the Win-82 manual.

to gate bias voltage to take into consideration, known as accumulation, depletion, and inversion. The presence of the different regions is a result of the majority charge carriers (e.g., holes in a p-type silicon wafer) in the semiconductor. When a negative bias is applied to the gate electrode, positively charged holes are attracted from the semiconductor bulk region to the oxide/semiconductor interface where they accumulate (the accumulation region) in order to maintain charge balance in the system. The depletion region is generated when a gate is made less negative and the reduced field across the oxide allows the charge at the interface to diminish. As the sign on the voltage changes from a negative to a positive, majority carriers are repelled from the interface creating an area depleted of majority carriers (the depletion region). Finally, the inversion region is generated when the voltage becomes very positive and the depletion width has increased to a point where other mechanisms become important. For example,

in the depletion region, the product of the concentration of electrons and hole (np) is much less than the square of the intrinsic carrier concentration (n_i^2) and in this case, pair generation may occur and the subsequent minority carriers can migrate to the interface. The result of this is prevention of further depletion and a constant value for the capacitance is maintained. An additional possible scenario may occur whereby insufficient time is allowed for pair generation in which case a model called deep depletion will occur.

The high frequency measurement system has the ability to measure two different frequencies and using Metrics ICS software with two different equivalent circuit models, seen in Figure 2-10, to generate capacitance values. This system does not directly measure a capacitance value for the films, but instead measures resistance and conductance and uses the models to generate the capacitance values. The parallel and series models represent two different physical structures. The series model addresses a capacitor in series with a resistance, possibly from the semiconductor. The equation that describes this scenario is:

$$Z = R + iX \quad (2-3)$$

where Z is the impedance, R is the resistance, and X is the reactance. Alternatively, the parallel model addresses a capacitor in parallel with some sort of conductance, possibly resulting from leakage through an ultrathin film. The equation that describes this scenario is:

$$Y = G + iB \quad (2-4)$$

where Y is the admittance, G is the conductance, and B is susceptance. Note that the

admittance, conductance, and susceptance are each the reciprocals of the impedance, resistance, and reactance, respectively.

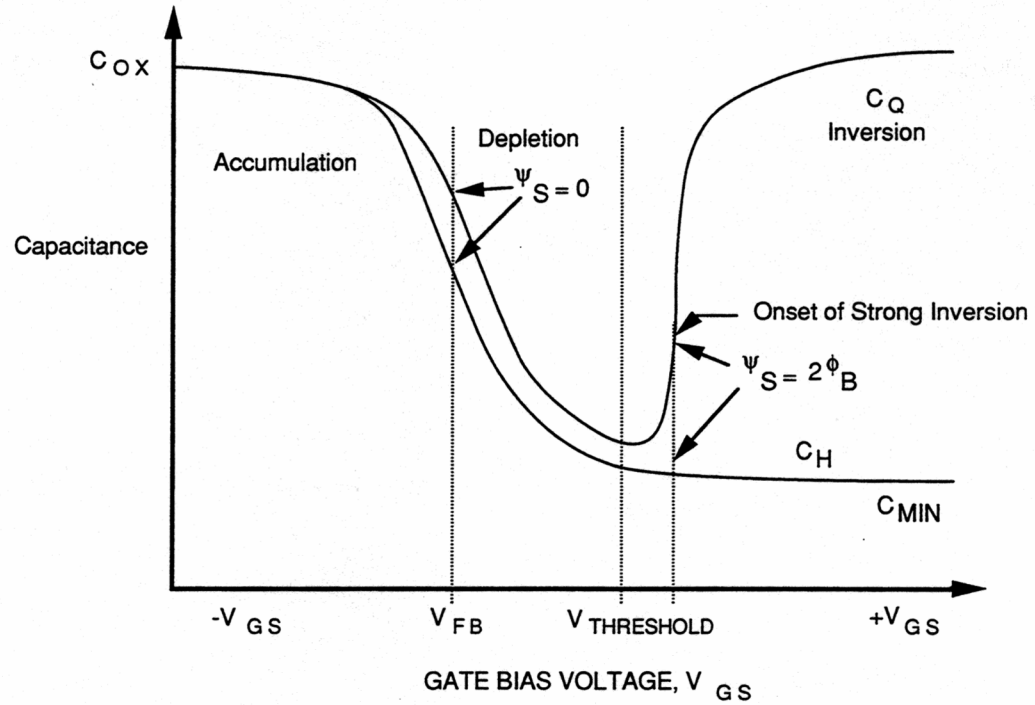


Figure 2-9: Typical capacitance/voltage response curve demonstrating major areas of interest modified from the Win-82 manual.

The reactance and susceptance can then be further described in a capacitive sense as:

$$X = \frac{1}{wC_s} \quad (2-5)$$

$$Y = wC_p \quad (2-6)$$

where ω is the frequency of the setup and C_s and C_p are the capacitance for the series model and parallel model respectively. The net impedance of the equivalent series and parallel circuits at a given frequency are equal, but the individual components are not:

$$R + iX = \frac{1}{G + iB} \quad (2-7)$$

If there is a lossless circuit (i.e. $R = 0$ and $G = 0$) the C_S and C_P are equal.

However, since circuits do have losses, a dissipation factor is added to the system

$$D = wC_S R \quad (2-8)$$

$$D = \frac{G}{wC_P} \quad (2-9)$$

Conversion from one equivalent circuit model to the other is obtainable through further manipulation of the previous equations yielding the conversion factors shown in Table 2-5.

Table 2-5: Conversion factors for series-parallel electrical equivalent circuits.

Model	Dissipation Factor	Capacitance	Resistance or Conductance
Parallel C_P, G	$D = \frac{1}{Q} = \frac{G}{wC_P}$	$C_s = (1 + D^2)C_P$	$R = \frac{D^2}{(1 + D^2)G}$
Series C_s, R	$D = \frac{1}{Q} = wC_S R$	$C_P = \frac{C_s}{1 + D^2}$	$G = \frac{D^2}{(1 + D^2)R}$

This treatment has been applied to illustrate how capacitance values are generated from the impedance values and subsequent conversion to series and parallel cases. As mentioned earlier, the series represents a physical scenario where a capacitor is in line with some type of resistance, while the parallel mode represents a physical scenario where a capacitor is in parallel with some type of conductance. This however does not take into consideration the physical possibility of an ultrathin film that is leaky, but also encounters resistance from the substrate. In this case, a three element electrical circuit, also seen in Figure 2-10, could be analyzed in a similar manner as above to develop equations for converting from either the parallel or series mode to the three element equivalent circuit that more appropriately represents the physical structure.

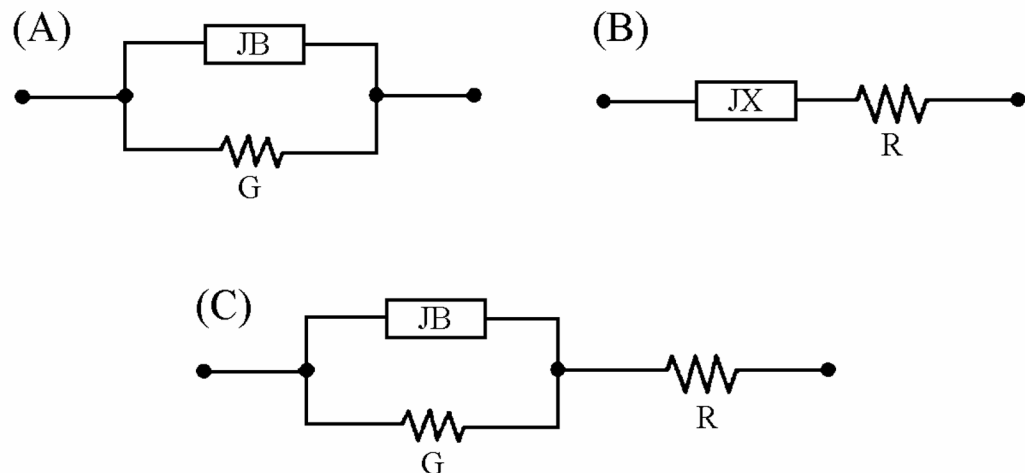


Figure 2-10: Equivalent circuits for estimation of capacitance in a) parallel, b) series, and c) combination models.

CHAPTER 3

KINETICS OF INTERFACIAL LAYER FORMATION DURING DEPOSITION OF HAFNIA ON SILICON

Oxide thin films are essential components of many advanced structures and devices. One of the most commonly used substrates for thin film deposition, both for applications and for properties characterization, is Si wafers. In many instances, the oxide films are directly deposited on silicon substrates. As long as the oxide films are thick, the chemical and physical phenomena occurring at the interface with the Si substrate do not usually play a major role in determining the properties of the deposited oxide films. However, a renewed interest in the growth of very thin (<10 nm) high dielectric constant (high-k) oxide films directly on Si has raised the question of the interfacial layer formation and its properties.⁵⁴⁻⁵⁶ In this portion of the work, a pulsed laser deposition (PLD) technique was used to deposit HfO₂ high-k dielectrics on Si. New results regarding the chemical composition and the kinetics of the interfacial layer growth during deposition of HfO₂ thin films on Si are presented here in this portion of the work.

Deposition Conditions

For this study, a 1" diameter x ¼" thick hafnium oxide target 99.99% pure from SCI Engineered Materials was ablated using a KrF excimer laser system in a typical PLD setup which was described in detail previously.⁵⁷⁻⁵⁹ The deposition parameters used were laser fluence of 2 J/cm², 5 Hz repetition rate, 430 pulses (yield thickness from 3 to 4 nm), substrate temperatures from 200 to 600 °C, and oxygen pressure during deposition from

1×10^{-4} up to 1×10^{-2} Torr. Table 3-1 reviews the sample matrix used for the nine samples in this portion of the experiments.

The films were deposited on (100) Si p⁻ substrates from MEMC cut to 2.5x2.5 cm squares then washed with acetone and methanol to remove any surface contamination. The samples were then dipped in a 1% HF solution for 10 minutes to remove the native oxide and were mounted onto the resistive heater using silver paste. This cleaning process passivates the dangling bonds of the Si with hydrogen giving between 10-30 minutes to pump down the sample before adsorption of water species and other contaminates to the surface occur.⁵⁹⁻⁶²

Table 3-1: Conditions for growth of ultra-thin HfO₂ films.

Sample ID#	Temp. °C	Pressure Torr
Hf11		1×10^{-4}
Hf12	200	1×10^{-3}
Hf13		1×10^{-2}
Hf14		1×10^{-4}
Hf15	400	1×10^{-3}
Hf16		1×10^{-2}
Hf17		1×10^{-4}
Hf18	600	1×10^{-3}
Hf19		1×10^{-2}

The surface morphology, thickness, and roughness of the deposited layers were investigated by x-ray reflectivity (XRR) with a Panalytical X'Pert MRD system. The XRR spectra were simulated using the software package Wingixa™. The same system was used for crystalline structure investigations by grazing incidence and symmetric θ - 2θ x-ray diffraction (GIXD and XRD). The chemical composition and bonding of the films were investigated by x-ray photoelectron spectroscopy (XPS) in a Perkin Elmer 5100 installation using Mg K_α radiation (1253.6 eV) at various take off angles ranging from 45-90°. The thickness and optical properties of the films were investigated by

variable angle spectroscopic ellipsometry (VASE) with a J. A. Woollam M-88 instrument using an incidence angle of 75°. The thickness, refractive index and extinction coefficient values were obtained by fitting the acquired data with a Cauchy model using the equipment software package.

X-ray Results

Upon sample fabrication, samples were cut into 1 x 1 cm squares for analysis. Due to the cosine distribution type of plume dynamics the film is not of uniform thickness across the whole sample thus it is necessary to use only the central 1 x 1 cm portion which is consistently the most uniform with a variation of ± 5 Å. Furthermore this sample size is ideal for all the analysis techniques. GIXD investigations were conducted at an incidence angle of $\Omega=1^\circ$ for all nine samples. The results from the two extreme temperature conditions of the samples are plotted in Figure 3-1. All samples in the 200 °C and 400 °C sets remained amorphous regardless of the oxygen pressure, which is to be expected as the crystallization temperature for HfO₂ is 450-500 °C. All films deposited at 600 °C exhibited broad peaks, a sign of rather poor and randomly oriented crystallites. Identification of the main peaks and relative intensities was found to match the monoclinic HfO₂ phase according to JCPDS reference card #34-0104. The peak at 55.5° is from the (311) plane of the silicon substrate. By using a glancing angle of 1° the proper diffraction conditions for this peak is present when the sample is mounted with the <010> or <001> planes in line with the beam. The samples were cut along these directions; typically the samples are mounted into the X'Pert system so that the beam impinges the sample perpendicular to the edge and centered on the sample. The (311) peak can be eliminated by using a phi rotation of the sample of 10-45°, however no peaks

from HfO_2 are in this region so this alignment step was not used. Symmetric XRD investigations did not reveal any particular texture in these films, the crystals are randomly oriented.

After each GIXD and XRD scan was made, an XRR spectrum was taken. The X'Pert system allows for all three measurements to be made sequentially once sample alignment has been completed with just a change in the optic slits. Angles from 0.125 to 5° were scanned. A typical XRR spectrum of the deposited HfO_2 films is displayed in Figure 3-2. Each spectrum was modeled using the WINGIXA software package. Also displayed in Figure 3-2 is the simulation of this spectrum obtained using a three layer structure: interfacial layer (IL), oxide layer (OL), and contamination layer (CL) located on the top surface which takes into account the carbon and water containing species. This three layer structure is represented in schematic form in Figure 3-3.

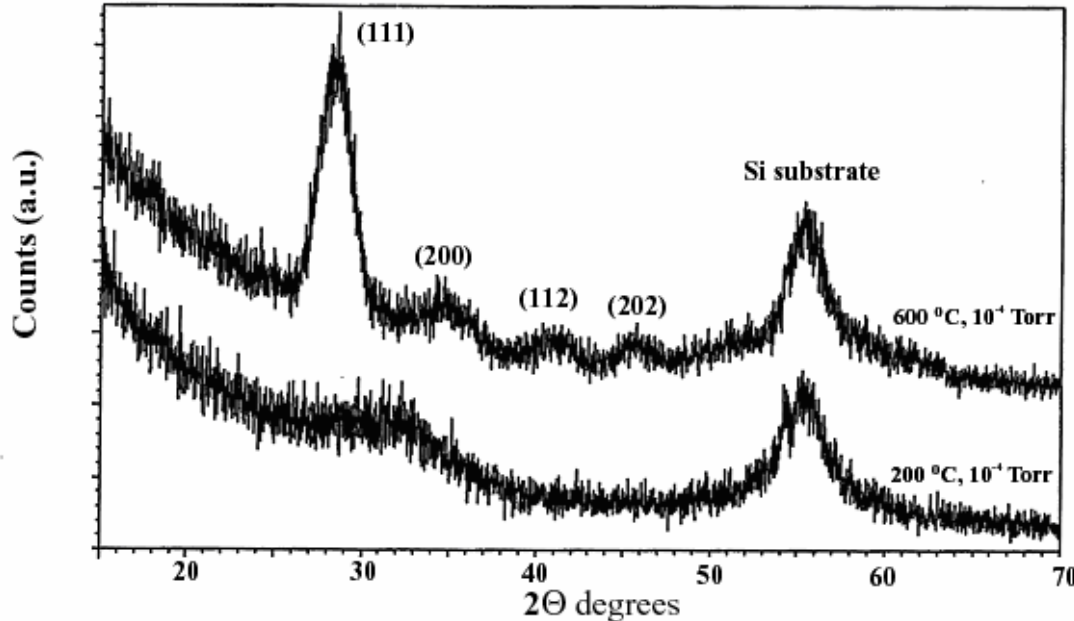


Figure 3-1: Comparison of GIXD ($\Omega=1^\circ$) for the 200 °C and 600 °C samples deposited in 1×10^{-4} Torr O₂.

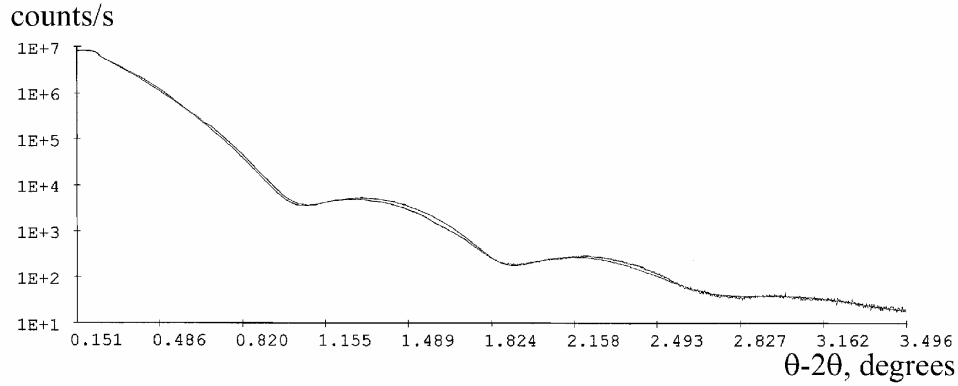


Figure 3-2: Acquired XRR spectrum and its simulation for a HfO_2 film deposited on Si at $200\text{ }^\circ\text{C}$ and 1×10^{-4} Torr of O_2 .



Figure 3-3: Schematic of gate oxide stack model used for XRR simulations.

The parameters used for simulations of all nine samples, i.e. layer thickness, roughness and density, together with the deposition conditions are displayed in Table 3-2. The mean square error of the fit χ is also included in the table. For reference, a good fit has χ values of less than 1×10^{-2} . To begin the iterative modeling process, the mass density of the hafnium oxide layer was first assumed to be the bulk tabulated value of 9.68 g/cm^3 . One can note that the region of the critical angle ($\sim 0.22^\circ$) was well simulated by using this standard value thus indicating that very dense compact films were produced.

The hafnium oxide layer density was held constant for all the sample models while the density of the IL and CL were allowed to change along with the thickness and roughness values for all the layers. The contamination layer affects the initial signal falloff and is necessary to bring the model in line with the raw data. This layer was initially assumed to have a density of 7.26 g/cm^3 , which is 75% of the HfO_2 layer density to account for voids and carbon contamination.

From the fit data, the density of the interfacial layer was consistently higher than 2.19 g/cm^3 , the density of amorphous SiO_2 . This is a clear indication that the interfacial layer is not pure SiO_2 , but a mixture containing HfO_2 . The interface layer roughness values, both towards the Si substrate and towards the deposited oxide layer are rather high, sometimes even higher than the surface roughness values. This is another indication that there was mixing between the SiO_2 and the deposited layer.

Table 3-2: XRR modeling parameters used to fit the spectra. Note values for thickness and roughness are giving in Å and the densities are given in g/cm^3 .

Sample ID	Thk. IL	Thk. OL	Thk. CL	Rgh. IL	Rgh. OL	Rgh. CL	Dens. IL	Dens. OL	Dens. CL	χ
Hf11	24.6	41.3	7.8	5.3	3.4	1.8	4.19	9.68	7.07	1.02E-02
Hf12	31.8	34.3	9.2	9.9	2.7	1.8	3.61	9.68	7.42	3.30E-02
Hf13	16.3	31.1	7.9	6.1	3.9	2.1	3.38	9.68	6.32	1.27E-02
Hf14	24.4	37.7	6.7	4.1	7.2	3.0	4.09	9.68	7.22	1.65E-02
Hf15	22.9	37.9	1.9	3.0	6.1	1.1	3.88	9.68	4.35	3.11E-02
Hf16	25.7	30.9	7.9	5.9	3.4	2.4	3.45	9.68	7.00	7.75E-03
Hf17	25.0	39.3	3.1	4.8	5.5	2.9	3.12	9.68	6.17	3.27E-02
Hf18	31.3	39.0	6.8	4.2	2.1	3.0	3.72	9.68	3.87	2.54E-02
Hf19	33.5	34.4	5.0	5.3	1.7	5.7	3.46	9.68	5.97	9.55E-03

Increased temperature was expected to promote oxygen diffusion and reaction with the silicon at the interface of the film. Average interfacial layer thickness did increase with increasing temperature, however all the data is not sufficient to statistically derive this conclusion as the 200 °C samples Hf11 and Hf12 exceed the thickness of the 400 °C

samples. The 200 °C samples should be further examined to rule out any experimental errors that might have been encountered which promoted the growth of the interfacial layer. Another trend that was expected is the increase in interfacial layer formation with the increase in oxygen pressure. The trend is sufficiently exemplified by the 600 °C sample set H17, H18, and H19 deposited at 1×10^{-4} , 1×10^{-3} , and 1×10^{-2} Torr O₂ respectively. This trend is shown in Figure 3-4 indicating a nearly linear relationship between the interfacial layer thickness and the log of oxygen pressure.

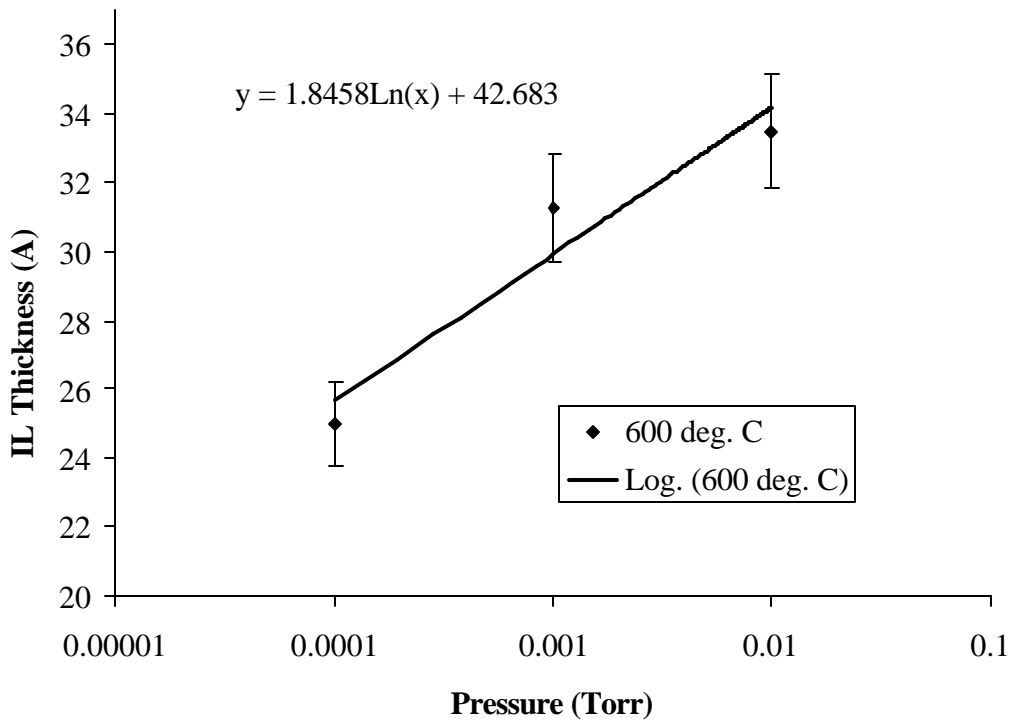


Figure 3-4: Interfacial layer thickness dependence on O₂ pressure for the 600 °C samples.

XPS Analysis

XPS was used to determine the composition, bonding environmental changes, and to estimate the thickness of the interfacial layer. Surveys from 0-1000 eV were taken for all the samples to first determine the elemental makeup and to detect any contaminates.

Then a multi-plex consisting of the C 1s, O Auger, O 1s, Si 2p, and Hf 4d peak regions were collected. The C 1s was used to determine calibration shifts resulting from charging in the samples. All materials analyzed using XPS have sufficient adventitious carbon contamination on the surface to produce the C 1s signal with known peak position of 284.6 eV. The plots were then fit using software that estimates the peaks with a 90% Gaussian curve. Fit information and analysis tables have been included in Appendix B.

XPS revealed symmetric peaks for the Hf 4d for all the samples, the two extreme conditions are compared in Figure 3-5, indicating one single oxidation state, which was identified as HfO_2 from their binding energies of 19.5 and 21.2 for the $d_{7/2}$ and $d_{5/2}$ orbitals respectively.

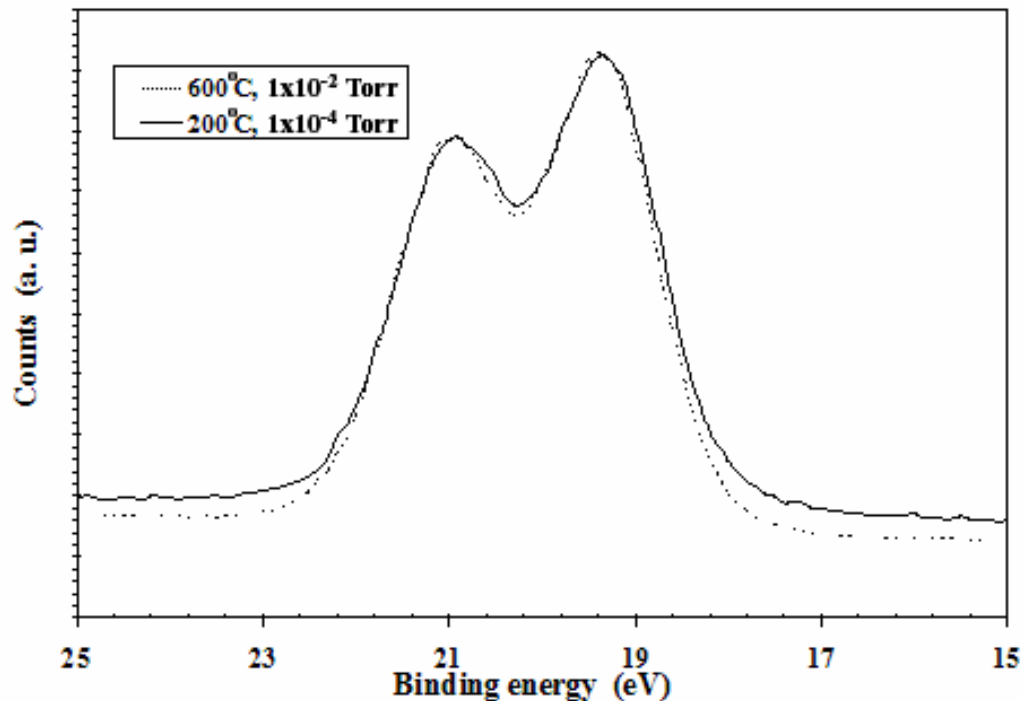


Figure 3-5: High resolution XPS scans of the Hf 4f region acquired from two HfO_2 films deposited on Si under very different conditions.

High resolution scans of the Si 2p region were acquired at takeoff angles of 45°, 65°, and 90° for the deposited samples. Figure 3-6 shows a typical scan of the Si 2p

region along with a three peak model taken using binding energies ranging from 95 to 108 eV. Peak A centered on 100.88 eV, before the C 1s shift was taken into account, represents the signal from Si^0 , Si bonded with Si, and peak B located at 104.45 eV is the signal from Si^{+4} , Si bonded with O. The third peak, C which was present in the 600 °C samples, is attributed to substiochometric silicon dioxide represented by silicon bonded to 3 oxygen atoms with a dangling bond.

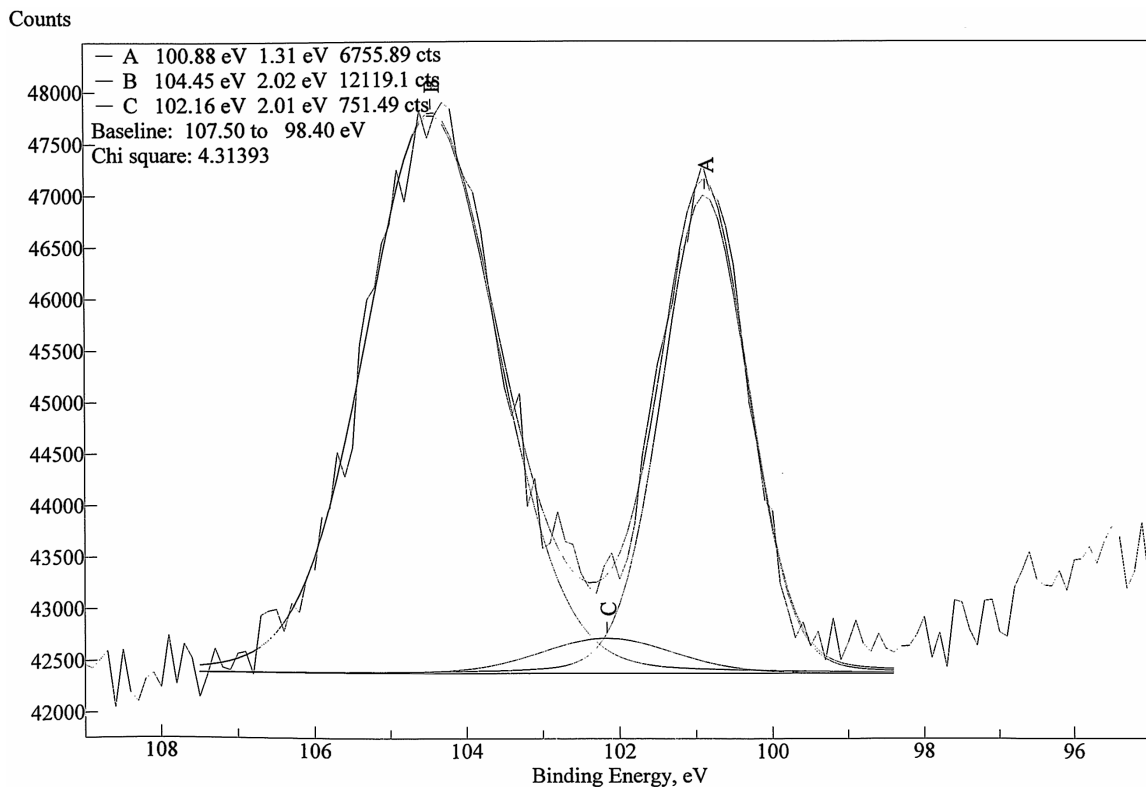


Figure 3-6: Raw data and fit for the Si 2p region for the 600 °C, 1×10^{-2} Torr O_2 sample.

The ratio of the intensities of the Si^0 to Si^{+4} peaks, represented by peak A and B respectively, were then used for estimations of the thickness of the SiO_2 layer according to:

$$d_{oxy} = I_{oxy} \sin a \ln [I_{oxy} / (bI_{Si}) + 1] \quad (3-1)$$

where $\lambda_{\text{oxy}}=36 \text{ \AA}$ is the photoelectron inelastic mean free path in the oxide film, α is the photoelectron take-off angle, I_{oxy} is the peak area for the Si-O bonding, I_{Si} is the integrated peak area for the signal from the substrate, and $\beta=0.8$ is a calibration constant for our XPS system which will be further discussed in the next chapter.⁶³ Although it has been claimed that Equation 3-1 could only work for takeoff angles greater than 60°, we have found that it can give rather accurate predictions down to 35°. The d/λ values for both a 5 nm pure SiO_2 standard and for a sample deposited at 1×10^{-2} Torr of O_2 and 600 °C are plotted in Figure 3-7. The variation between the 65° and 90° measurements for the deposited sample exceeds the error of our system based on the 5 nm SiO_2 standard. This suggests that the interfacial layer is a physical mixture of $\text{HfO}_2/\text{SiO}_2$. If the interfacial layer was uniform throughout, the d/λ would have yielded the same result for both the 65° and 90° degree scans. The estimated IL thickness using Equation 3-1 and a take off angle of 90° is displayed in the summary Table 3-4.

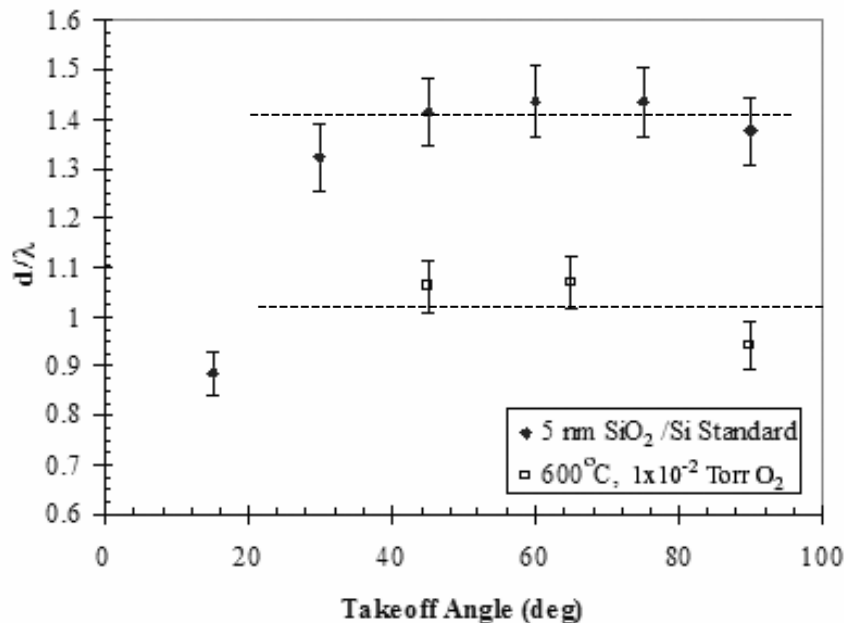


Figure 3-7: Variations of d/λ values for a 5 nm pure SiO_2 on Si and a deposited sample with changes in the take off angle.

The interfacial layer thickness values obtained using XPS are plotted in Figure 3-8. The 400 °C and 600 °C sample sets show a nearly linear increase with the log of oxygen deposition pressures used. The slope of the relationship is the same for both sets. Furthermore, higher temperature increased the interfacial layer thickness formation. The 200 °C sample set again did not follow the trends seen with the other two sets. Problems such as incomplete removal of the native oxide during the cleaning process might be the cause of this error.

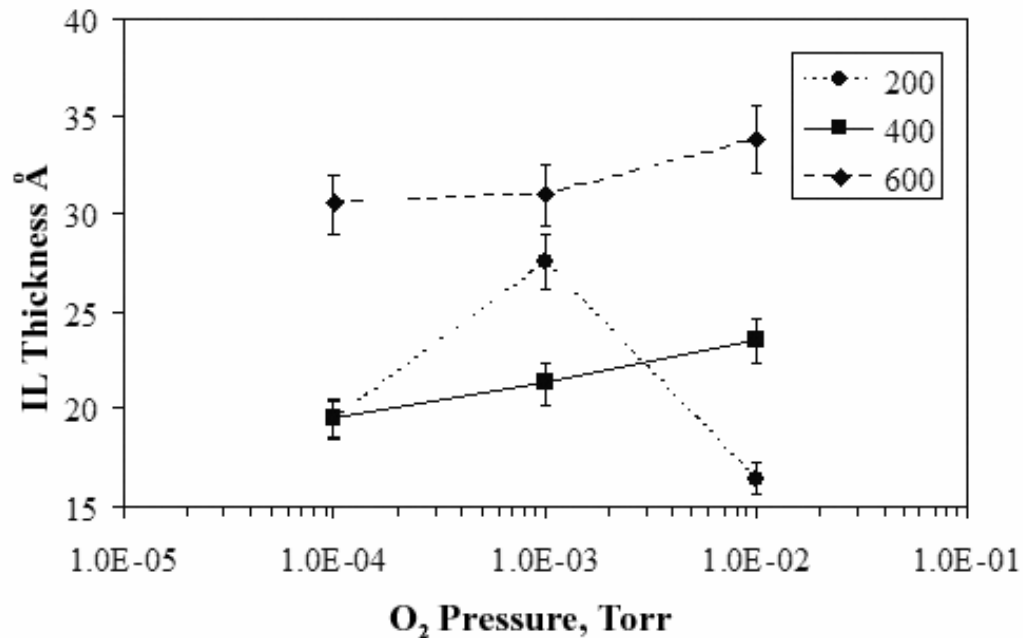


Figure 3-8: Interfacial layer thickness as a function of temperature and pressure.

Ellipsometry Results

Finally, the thickness of the deposited structures was estimated using VASE. The acquired spectra were simulated using the three layer model used for XRR simulation. An effective medium approximation Cauchy model consisting of 75% SiO₂ and 25% HfO₂ for the IL and 50% HfO₂ and 50% voids for the CL was used to simulate the acquired data. The simulation data were quite close to the acquired data without any

need to modify of the HfO_2 refractive index or add absorption, suggesting high optical quality of the deposited films. The layer thickness values are shown in Table 3-3.

Table 3-3: Ellipsometry modeling results

Sample ID	SiO_2 (50% HfO_2)[?]	HfO_2 [?]	$\text{HfO}_2+40\%$ void[?]
Hf 11	25.0	36.8	9.1
Hf12	31.7	34.9	9.4
Hf13	16.2	39.5	16.2
Hf 14	24.4	36.3	7.0
Hf15	22.9	36.1	2.4
Hf16	25.6	28.1	8.1
Hf 17	25.0	42.9	3.3
Hf18	31.6	32.2	5.1
Hf19	33.2	29.8	4.52

Summary

XPS, XRR and SE investigations were used to determine the structure of the HfO_2 thin films deposited on Si. It was found that samples deposited with substrate temperatures of 600 °C exhibit small randomly oriented crystals but samples deposited up to 400 °C remained amorphous. The interfacial layer was shown to consist of SiO_2 physically mixed with the deposited oxide which always formed, even when the deposition temperature was only 200 °C and at low oxygen pressures. The thickness of this layer is around 1-4 nm, depending on the deposition conditions used. Its density is greater than that of pure bulk SiO_2 resulting from a physical mixture of silicon suboxides with the grown oxide layer.

By inspecting the results in Table 3-4, one can clearly note that there is a good agreement between the layer thickness values obtained using these three methods. The higher the deposition temperature and/or oxygen pressure used during deposition, the thicker the IL. Also, the SE and XRR results support the XPS indication that the IL contains a physical mixture between the SiO_2 layer and the deposited HfO_2 oxide, similar

Table 3-4: Comparison of the thickness values (in Å) for HfO₂ thin films deposited on Si

Sample ID#	Temp. °C	Pressure Torr	XRR IL ?	OL ?	CL ?	Ellipsometry IL ?	OL ?	CL ?	XPS IL ?
Hf11		1x10 ⁻⁴	24.6	41.3	7.8	25.0	36.8	9.1	19.4
Hf12	200	1x10 ⁻³	31.8	34.3	9.2	31.7	34.9	9.4	27.5
Hf13		1x10 ⁻²	16.3	31.1	7.9	16.2	39.5	8.1	16.4
Hf14		1x10 ⁻⁴	24.4	37.7	6.7	24.4	36.3	7.0	19.5
Hf15	400	1x10 ⁻³	22.9	37.9	1.9	22.9	36.1	2.4	21.3
Hf16		1x10 ⁻²	25.7	30.9	7.9	25.6	28.1	8.1	23.5
Hf17		1x10 ⁻⁴	25.0	39.3	3.1	25.0	42.9	3.3	30.5
Hf18	600	1x10 ⁻³	31.3	39.0	6.8	31.6	32.2	5.1	31.0
Hf19		1x10 ⁻²	33.5	34.4	5.0	33.2	29.8	4.5	33.8

to our previous findings done by our group for Y₂O₃⁶⁰ and ZrO₂⁶¹ films deposited on Si.

By understanding the nature of the interfacial layer and its formation, better control of the layer can be realized to tailor the properties of the gate stack in future samples.

CHAPTER 4

EFFECT OF UV-ASSISTED OXIDATION AND NITRICATION OF HAFNIUM METAL FILMS

Hafnium oxide has been shown to be a promising candidate for an alternative high-k dielectric due to its high dielectric constant, large bandgap, and stability on silicon.⁵⁰⁻⁵² However processing temperatures required for standard deposition techniques are too high and exceed the crystallization temperature for the films thus resulting in current leakage and diffusion paths at the grain boundaries. Work has been done using ultraviolet-assisted oxidation of zirconium metal films deposited using a radio frequency direct current sputtering method which was shown to produce higher quality films at lower processing temperatures.⁴⁵⁻⁴⁹ Furthermore, nitridation of various metal oxide films has been used to retard the growth of interfacial layers by acting as a diffusion barrier to oxygen.⁶⁴⁻⁶⁸ This portion of the work extends these investigations to the hafnium metal system in an attempt to understand the effect of UV oxidation and the incorporation of nitrogen into the films on their electrical and structural properties under lower processing temperatures.

Experiment

Initially, it was believed a thin Si_xN_y layer grown at the interface using UV radiation would serve as a superior base for the deposition of the films in this portion of the work. The silicon wafers were cut into 2.5 x 2.5 cm squares and mounted on the resistive heater and placed into the vacuum chamber. After pumping to 1x10⁻⁶ Torr, the chamber was backfilled with 500 Torr of ammonia. The substrate was then heated to 650

$^{\circ}\text{C}$ and irradiated with the UV lamp array for 30 minutes. This formed a 20 \AA layer of Si_xN_y verified by XPS and ellipsometry. Capacitors were formed out of the films and capacitance/voltage measurements were taken. Figure 4-1 is the CV response of one of the nitrided silicon films that was tested. As can be seen from the plot, the response is not sharp but instead is elongated over 2 volts. This is a result of extreme amounts of interface traps created at the silicon/silicon nitride interface. Furthermore, at higher negative bias the capacitance is not constant but instead starts to drop off. This is suggestive of a poor quality film which is leaky. From this result in order to eliminate the charge trapping defects inherent when using silicon nitride, it was decided to deposit the hafnium films onto bare silicon.

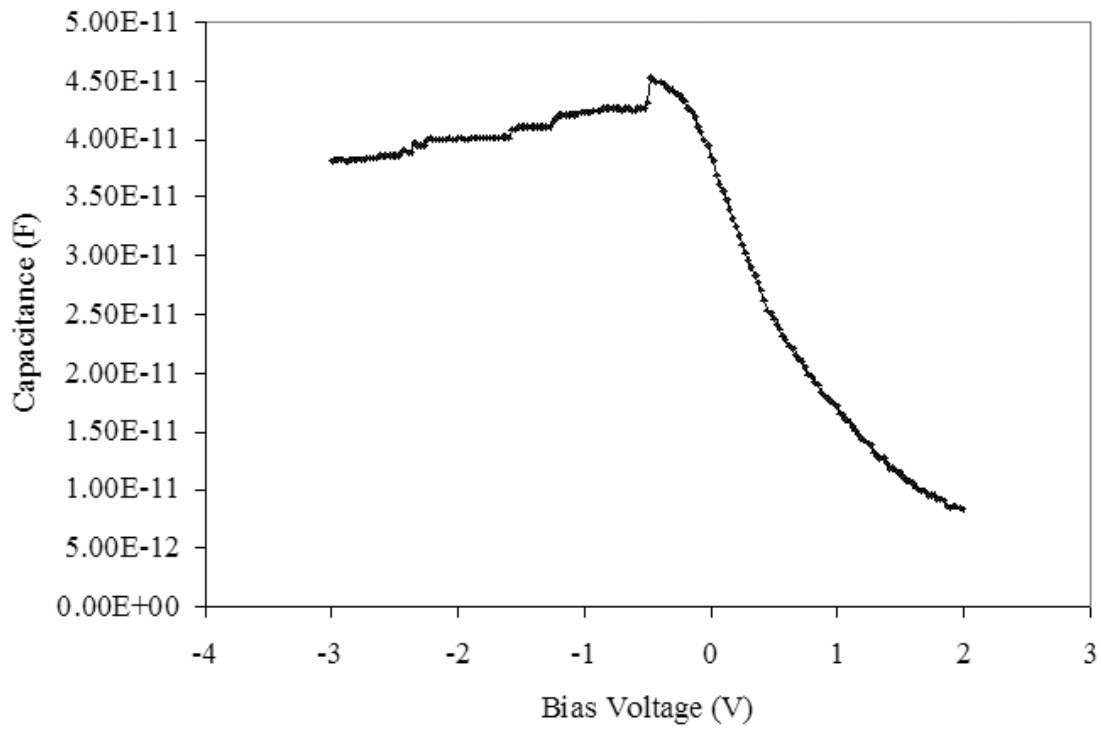


Figure 4-1: CV response of an UV grown Si_xN_y film.

A 248 nm KrF excimer laser system in a typical pulsed laser deposition (PLD) setup was used to ablate a hafnium metal target 99.95% pure from SCI Engineered Materials. The deposition parameters used were laser fluence of 3.0 J/cm^2 at a 5 Hz pulse rate with a total pulse count of 1500 for metal film thickness of 35 Å and oxidized film thicknesses of 45-50 Å. The films were deposited at 350 °C on p⁻ (100) Si substrates from MEMC (9-18 Ω cm) that were cleaned using an SC1 solution. This solution contains 80 vol% distilled water, 16 vol% hydrogen peroxide diluted to 30 vol% in distilled H₂O, and 4 vol% ammonium hydroxide. The samples were then dipped in a 1% HF solution for ten minutes to remove the native oxide. Depositions were performed either under residual vacuum at 1×10^{-6} Torr or under 1×10^{-2} Torr of ammonia. Post deposition anneals were carried out in-situ in 300 Torr of O₂ at 400 °C both with and without a Hg lamp array for 30 minutes. Each lamp emits 254 and 185 nm wavelength radiation at a total power density of 200 mW/cm². The power density from the 185 nm wavelength portion of the emission spectra is 10-15 mW/cm². Previous experiments determined that the use of UV during deposition in ammonia had no effect on the films at the deposition temperature of 300 °C. At 300 °C even with the activation of the ammonia by the removal of one or two hydrogen atoms due to UV interaction, there is not sufficient energy to promote bonding with the hafnium metal being deposited or with the silicon substrate. Therefore all depositions were conducted with the UV lamps off. A summary of the sample matrix is given in Table 4-1. This data set was repeated 3 times to study repeatability and to estimate error.

The surface morphology was studied using atomic force microscopy (AFM, Digital Instruments Nanoscope III) both in contact and tapping modes. Crystallinity

Table 4-1: Growth and postdeposition conditions for UV oxidation of Hf metal ultra-thin films.

Sample ID #	Deposition Pressure Torr	Anneal Conditions
H2	1×10^{-6}	UV
H3	1×10^{-6}	No UV
H4	1×10^{-2} Ammonia	UV
H5	1×10^{-2} Ammonia	No UV

comparisons and phase identification was done using grazing incidence x-ray diffraction (GIXD, Panalytical X’Pert system). The chemical bonding and composition of the films was investigated by x-ray photoelectron spectroscopy (XPS, Perkin Elmer 5100) using Mg K α radiation (1253.6 eV). A calibration study using a 50 Å SiO₂ film on Si standard was also carried out with the XPS system to fit the results of the angle-resolved measurements. High resolution spectra of the Si 2p region from the standard film were acquired at takeoff angles from 15° to 90° and the area ratios of the Si⁰ and Si⁴⁺ peak were compared to obtain the calibration constant for our system. Finally MOS capacitors were fabricated by sputter deposition of 1000 Å thick platinum electrodes using a shadow mask having circular dot patterns of various sizes. Capacitance voltage and current measurements were taken using a Keithley Instruments Inc., 590 capacitance meter, KI236 source measurement unit (SMU), and the Kiethley Instruments Inc. Win-82 measurement system. Confirmation of results and further analysis was done at the University of Texas-Austin. Cross-sectional transmission electron microscopy (XTEM, JEOL 2010) was used to verify thickness and layer uniformity after electrical measurements were concluded for two of the samples.

An additional set of four samples was deposited using substrate temperatures of 650 °C. At this temperature, it was believed that a more significant amount of nitrogen could be incorporated into the hafnium metal thin film. Previous work done by N.

Bassim *et al.* showed that UV radiation from our lamp array promotes the activation of ammonia into reactive species which then form a nitride layer on the surface of silicon substrates. Significant nitride layer growth occurred at substrate temperatures of 650 °C. Nitrogen does not readily react with metals and requires large activation energies. Thus for this set of experiments substrate temperatures of 650 °C were used to afford greater thermal energy for the reaction. Furthermore effects of UV during deposition and the oxidation annealing steps were compared. Finally, the electrical properties of the high temperature deposited samples were compared to the first set of samples deposited at 350 °C.

Results and Discussion for Low Temperature Deposited Samples

Surface Morphology

Atomic force microscopy was first conducted using contact mode for all four samples. An area of 1 μm x 1 μm was scanned using a tip capable of near atomic resolution on relatively smooth samples when properly calibrated. The 2D scans obtained are shown in Figures 4-2 and 4-3. Root mean square roughness was calculated for each sample based on the scans shown. These results are given in Table 4-2. The UV oxidized samples, H2 and H4, exhibit greater Z-ranges and higher RMS roughness values. There also is a slight but noticeable decrease in roughness with the addition of nitrogen.

The quality of the scans obtained using contact mode was poor, possibly due to washout from tip effects, so samples were reanalyzed using tapping mode, which affords higher resolution as the tip does not make contact with the sample but instead rides above the sample at a predetermined distance based on van der Waals forces and then is

Table 4-2: Z range and RMS roughness for oxidized Hf metal films.

Sample ID	Z range Å	RMS Roughness Å
H2	58.7	3.7
H3	24.6	2.3
H4	33.6	2.5
H5	26.5	2.0

cyclically flexed toward the sample during the measurement. The 3D scans taken from samples H2 and H3 are plotted in Figure 4-4.

From the tapping mode results, the surface of the UV-irradiated samples again showed a greater degree of roughness. The UV-irradiated sample exhibited a z-range of 7.8 nm and a RMS value of 6.4 Å while the non-irradiated sample had a z-range of 1.7 nm and a RMS value of 1.2 Å. It is believed that the UV-radiation promotes crystallization of the films. This effect has been seen before with BST films that our group has previously reported.⁶⁹ The increase in roughness is due to crystallization resulting from the UV radiation acting as a non-thermal energy source thus affording sufficient energy for promoting nucleation and growth of randomly oriented crystals at temperatures below the crystallization temperature. The 185 nm radiation is absorbed by the oxygen within 5 cm of the lamps based on the measured falloff of the intensity done at atmosphere with a detector head specifically designed to measure 185 nm radiation. Each sample is 8.5 cm from the nearest lamps, so the crystallization enhancement must be from the 254 nm radiation (4.88 eV).

X-Ray Analysis

Upon examination of the x-ray data collected, it was shown that the UV-radiation did in fact promote crystallization in the films. GIXD spectra taken at $\Omega=1^\circ$, plotted in Figure 4-5, demonstrate the emergence of a monoclinic HfO_2 phase (JCPDS 34-0104)

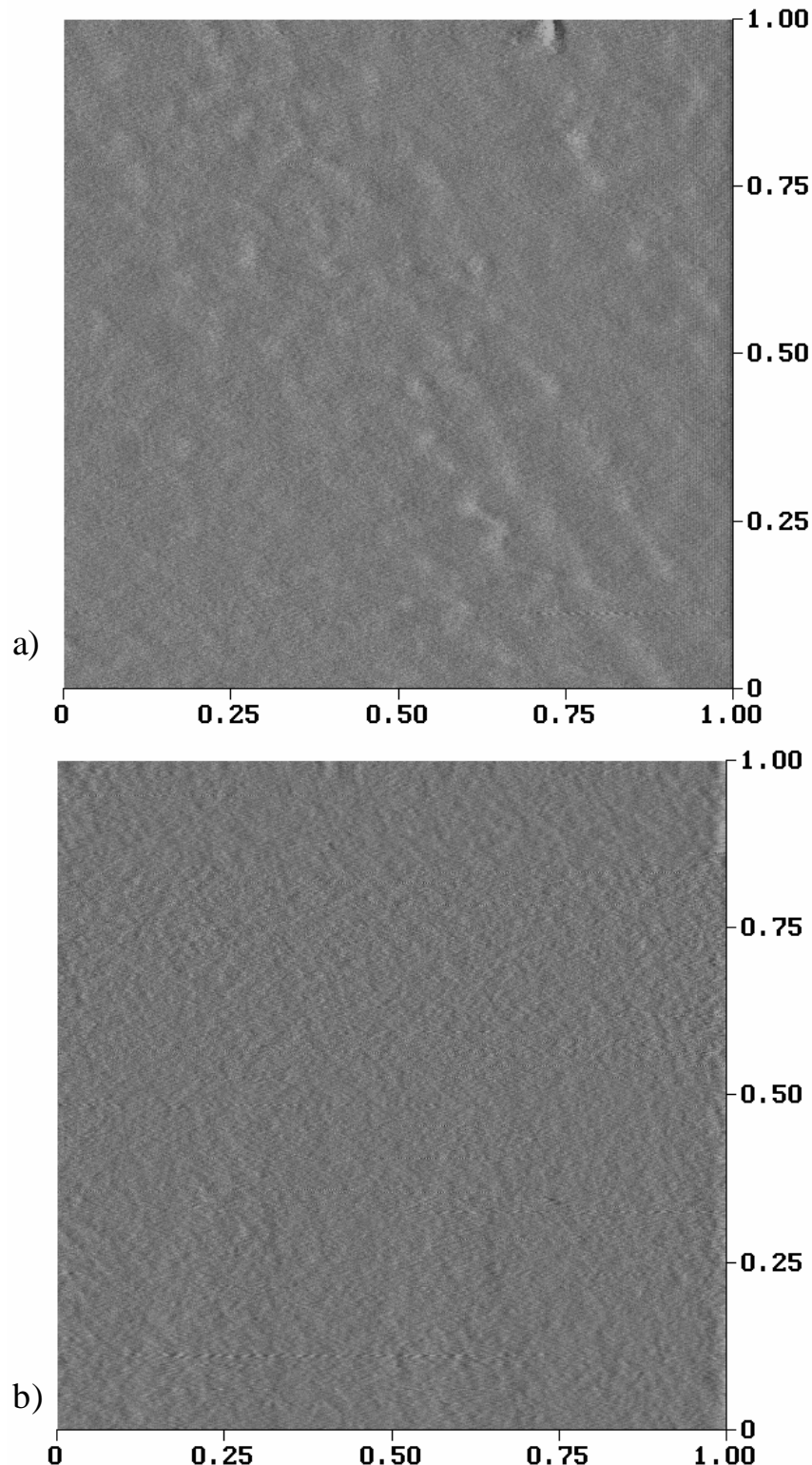


Figure 4-2: 2D AFM scans of samples a) H2 and b) H3 taken using contact mode. The scale is in μm .

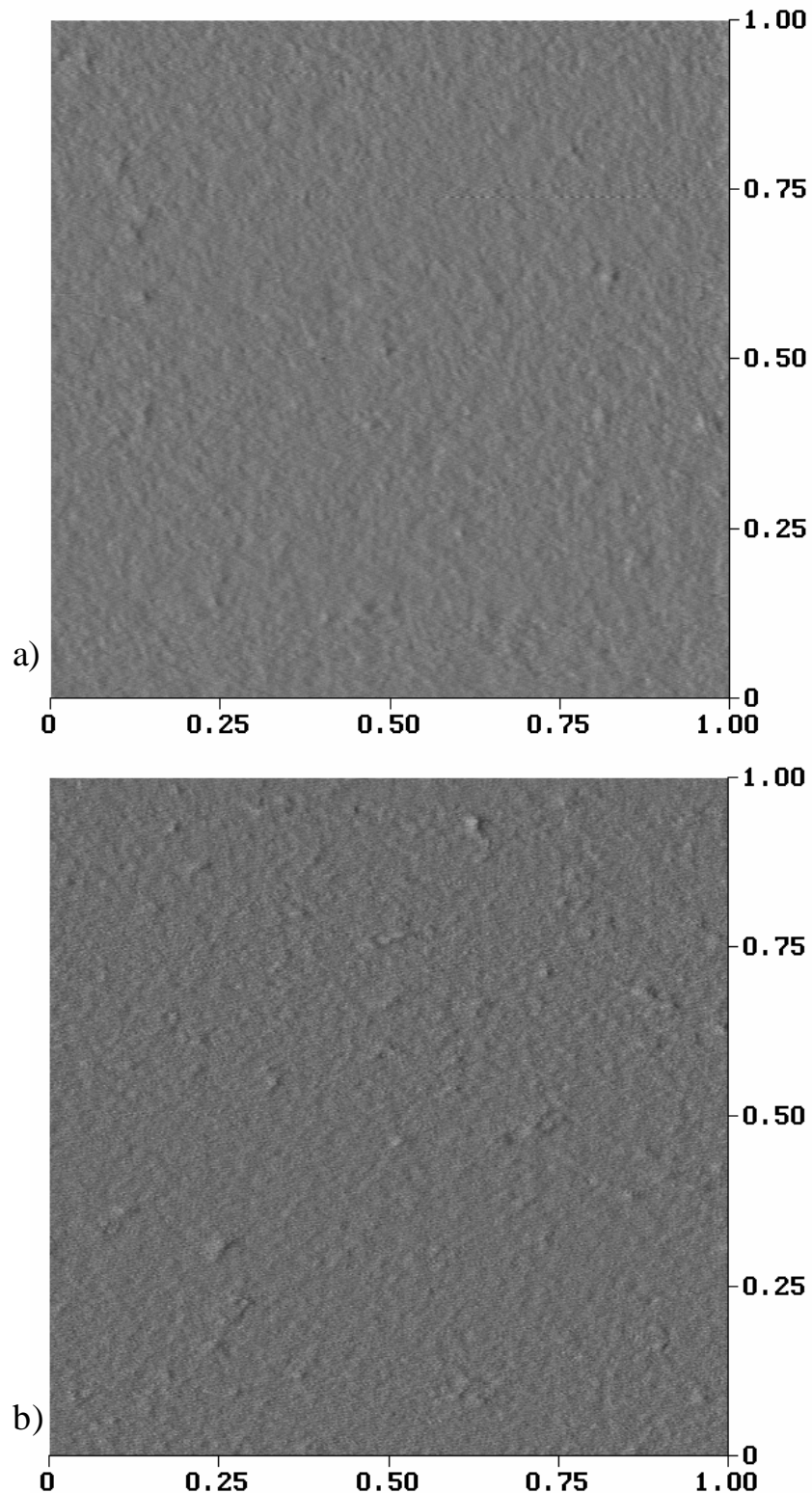


Figure 4-3: 2D AFM scans of samples a) H4 and b) H5 taken using contact mode. The scale is in μm .

with the UV-assisted oxidation. The radiation not only acts to break the oxygen into more reactive species, but also acts as a non-thermal energy source providing the activation energy for adatoms diffusion, crystal nucleation, and growth. Similar emergence of the monoclinic phase of HfO₂ was noted in the nitrided samples with no noticeable change in the lattice parameters.

X-Ray Reflectivity

As deposited metal films were analyzed using XRR in the Panalytic X’Pert system. A typical scan and fit is shown in Figure 4-6. The films were all 40±3 Å with a density of 12.9 g/cm³ and a mixed interface of ~8±2 Å having a density of 6.3 g/cm³. The density of the metal layer suggests that 1-3% porosity was present as the bulk density of Hf metal is 13.3 g/cm³.

XPS Analysis

XPS was used at take off angles of 45° and 90° for all of the scans in order to compare changes in composition with depth in the film and to better understand the nature of the silicon/film interface. Prediction of SiO₂ layer thickness and uniformity can be obtained using the previously mentioned Equation 3-1:

$$d_{oxy} = I_{oxy} \sin \alpha \ln [I_{oxy} / (\beta I_{Si}) + 1] \quad (3-1)$$

where λ_{oxy} is the photoelectron effective attenuation length in the oxide film, α is the photoelectron take-off angle, I_{oxy} is the peak area for the Si-O bonding, I_{Si} is the peak area for the signal from the substrate, and β is the calibration constant for the system.⁶³ Our system was calibrated using the high resolution Si 2p scans, shown in Figure 4-7, taken at angles from 15-90°. From these results, values of $\beta = 0.8$ and $\lambda = 36 \text{ \AA}$ were obtained and d/λ was calculated to be 1.40±0.05 for angles 45-90°.

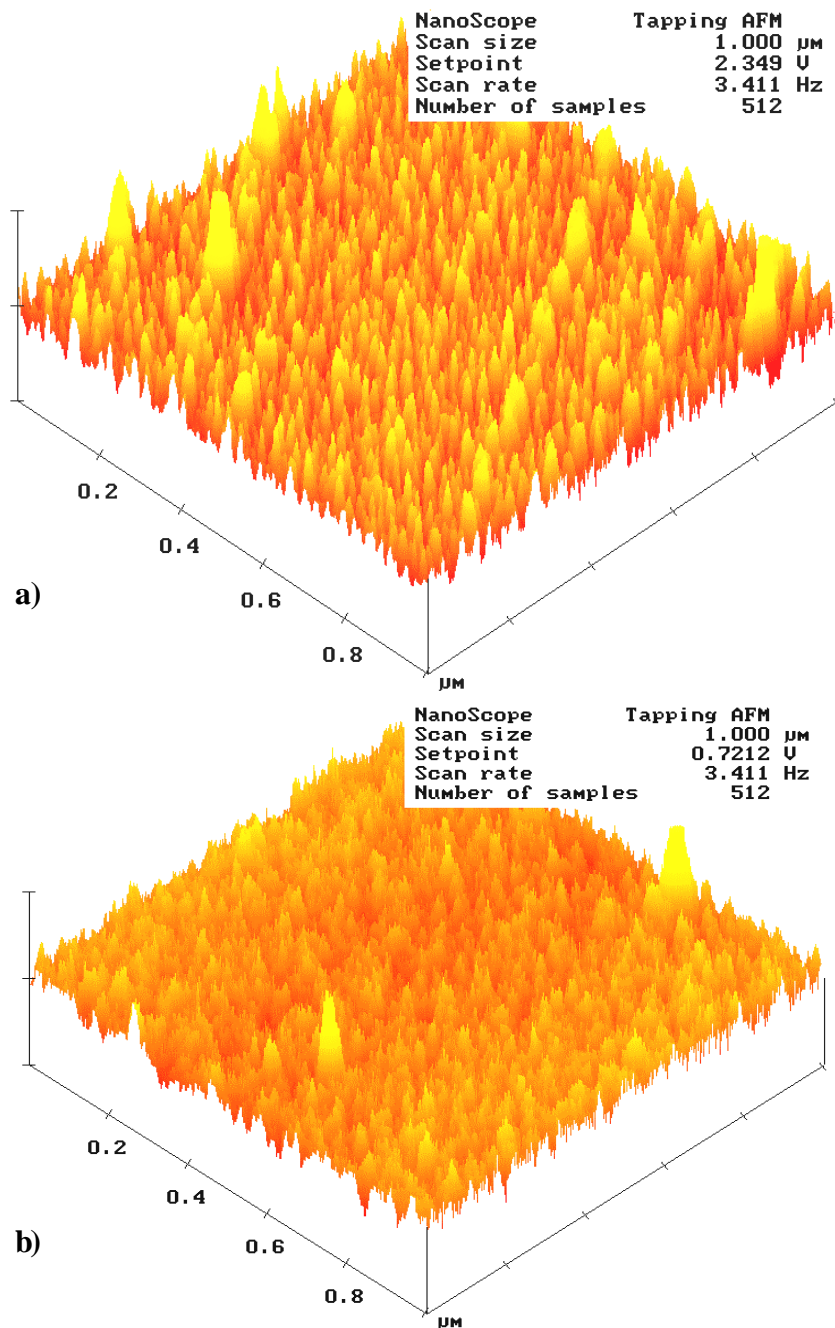


Figure 4-4: 3D AFM micrographs of both a) UV-oxidized and b) non-irradiated hafnium films.

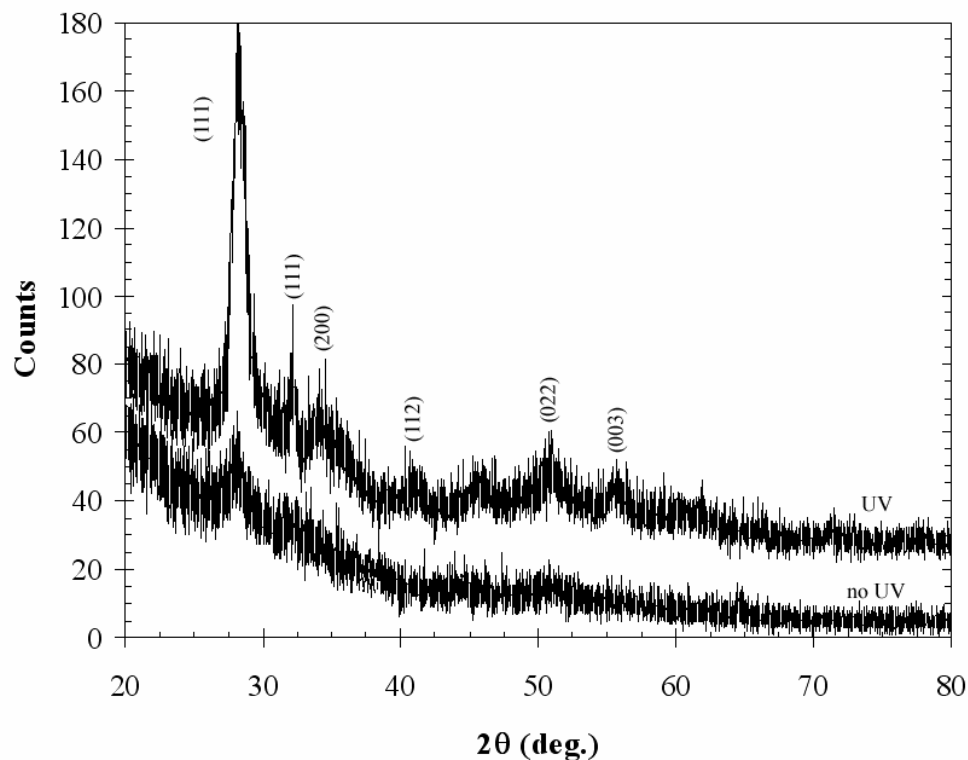


Figure 4-5: GIXD spectra ($\Omega=1^\circ$) of Hf films deposited on Si and oxidized with and without UV.

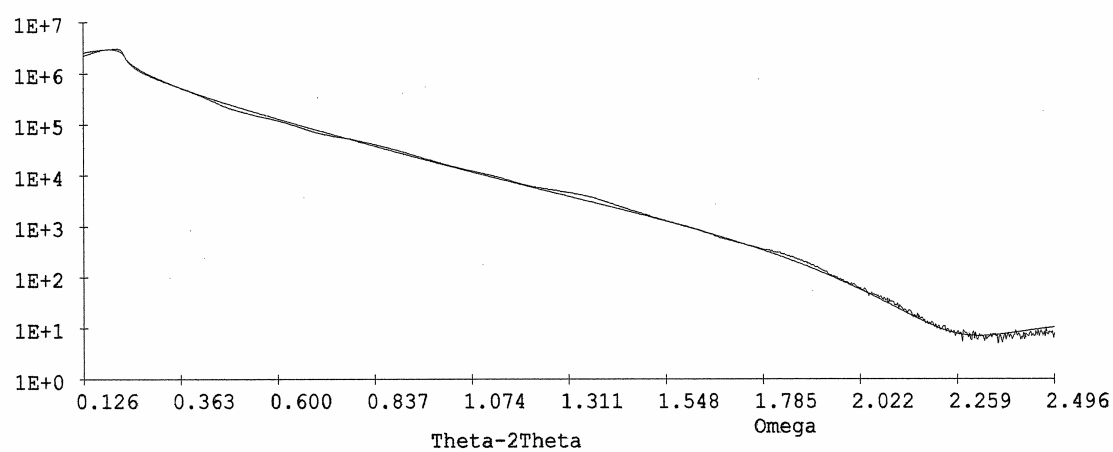


Figure 4-6: XRR plot and fit for as deposited Hf metal film.

The Si 2p scans plotted in Figure 4-8 were fit with two 90% Gaussian curves representing the Si-Si and Si-O bonding. The areas were used to calculate the d/λ values for both the 45 and 90° scans. The results of these calculations are given in Table 4-3. For all but one of the samples the d/λ values were nearly identical. Therefore the interfacial layer is primarily $\text{SiO}_2/\text{SiON}_x$ with very little degree of mixing occurring between the silicon dioxide and hafnium oxide layers. Sample H3 (no nitrogen, no UV) was the only sample with a mixed interface. The UV radiation is believed to promote the separation of the silicon dioxide and hafnium oxide into two distinct layers, while the nitrogen prevents the initial mixing normally encountered with PLD deposition.

Table 4-3: d/λ values for samples H2-H5

Sample ID	Angle	Si-Si Area	Si-O Area	d/λ
H2	45°	400	1370	1.176
	90°	986	1572	1.096
H3	45°	586	833	0.722
	90°	817	1532	1.207
H4	45°	419	1239	1.094
	90°	1207	1660	1.000
H5	45°	3506	2042	0.547
	90°	1676	1865	0.616

The Si 2p scans also show a larger percentage of Si-O peak area in the UV-irradiated samples and a peak shift of 0.5 eV to higher binding energies approaching the reported value of 103.6 eV for silicon bonded to oxygen in a pure thick SiO_2 layer.⁶⁰ Therefore, the UV-radiation is promoting oxidation of the interfacial silicon. The O 1s data for the same samples, plotted in Figure 4-9, shows a similar trend whereby the irradiated samples have a higher energy shoulder located at binding energies of 535 eV representing greater concentrations of Si-O bonding. Peak fit analysis using two peaks, one at 531.5 eV representing the oxygen atoms bonded to silicon and the other peak at

533 eV indicative of oxygen bonded with Hf, indicates an increase of 30% Si-O bonding in the UV irradiated samples.

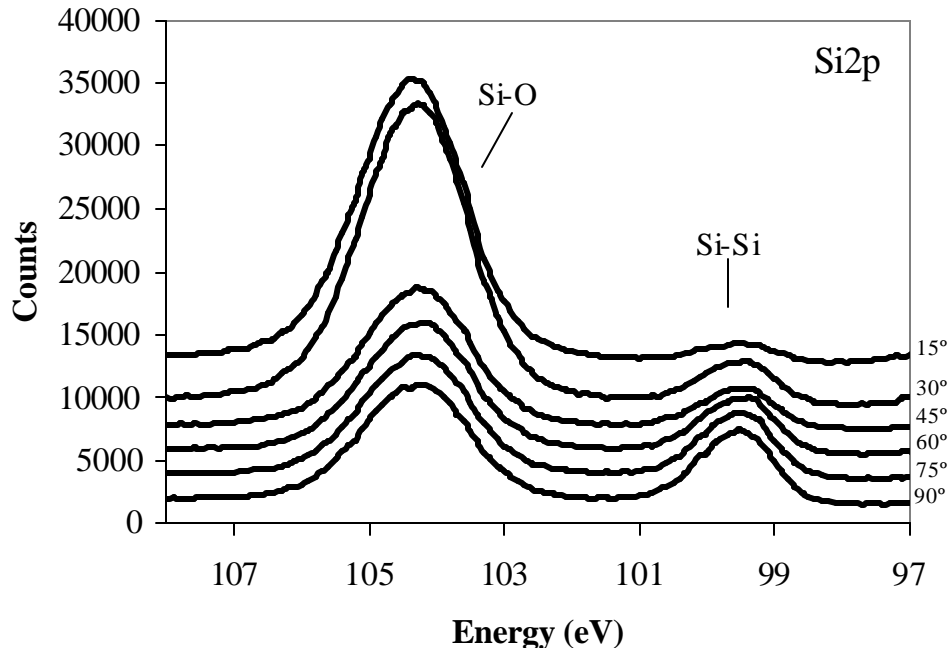


Figure 4-7: Angle-resolved XPS Si 2p spectra for system calibration.

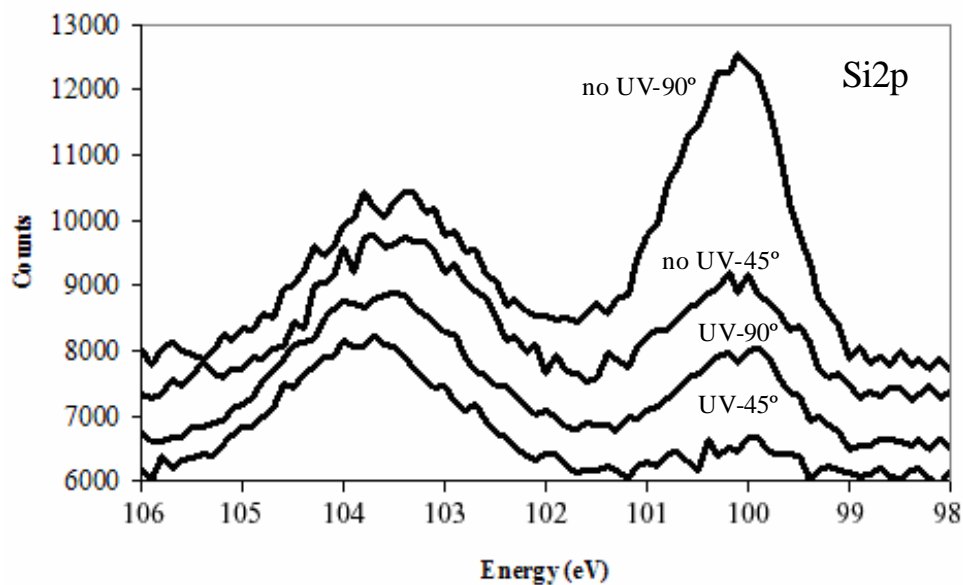


Figure 4-8: Angle-resolved XPS Si 2p spectra for H2 and H3 (UV and no-UV films).

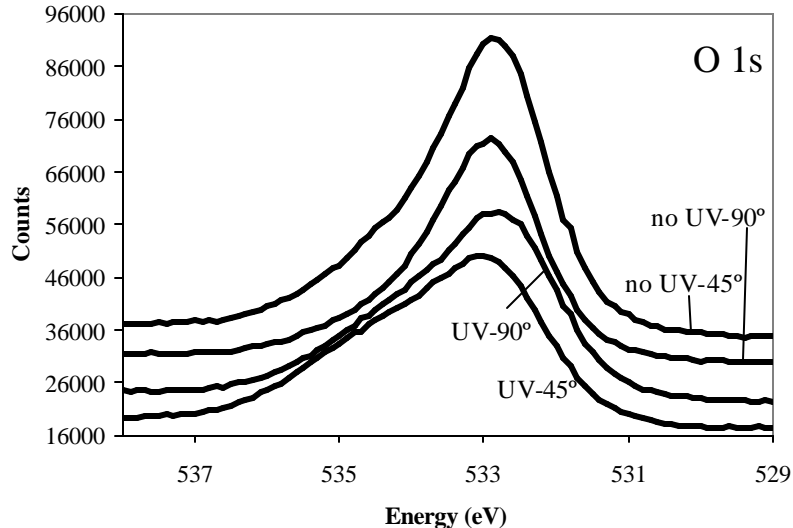


Figure 4-9: O 1s spectra for H₂ and H₃ (UV and no-UV) films at 45 and 90°.

According to XPS chemical composition analysis, depositing in ammonia only allowed for less than 2 atomic% incorporation of nitrogen into the films. Further trials using UV-radiation during deposition were tested to attempt to increase the concentration of nitrogen, but yielded the same result. It can be concluded that the energy of the radiation is not sufficient to promote highly significant amounts of reaction of the ammonia with the depositing hafnium metal or with the silicon substrate at the substrate temperature of 350 °C.

Even with just 2% incorporation of nitrogen into the films, the interfacial layer of the nitrided films have a larger ratio of Si-Si peak area suggesting less interfacial growth as shown in Figure 4-10. The Si-O peak also undergoes a shift of 1 eV to lower binding energies due to the change the bonding environment of the silicon atoms at the interface. The shift could result from the formation of a thin Si₃N₄ layer. Binding energies for Si₃N₄ type species lie within the intermediate range between the Si-Si and Si-O peaks. For fully nitrided silicon this peak is located at 101.8 eV.

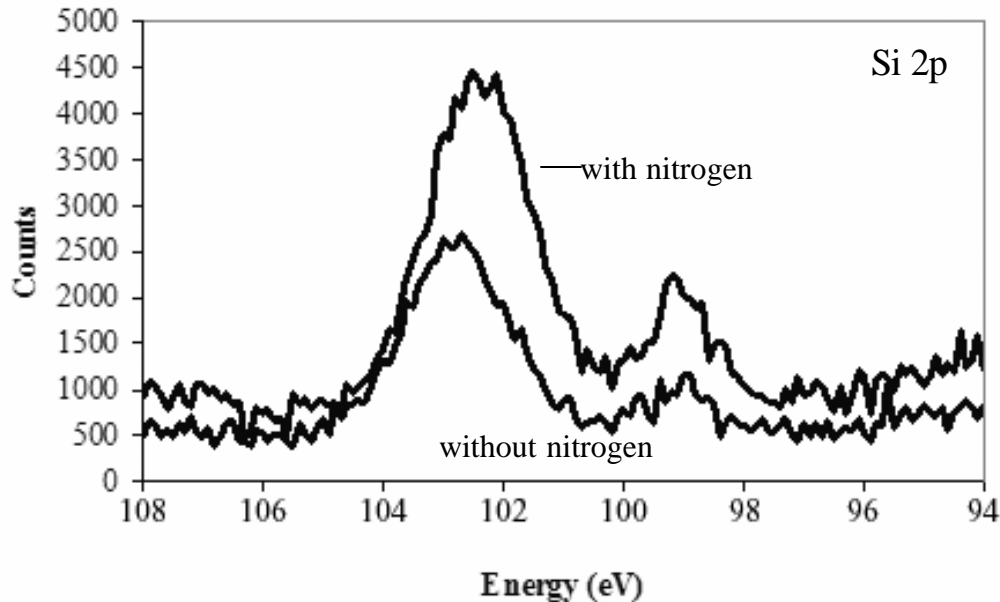


Figure 4-10: Si 2p spectra for UV-oxidized films H4 and H2 (with and without nitrogen).

In order to confirm the nature of the nitrogen in the film, high resolution XPS scans were taken for the N 1s peak range. Due to an overlap of the N 1s peaks and a higher energy satellite peak of the Hf 4p3 peak, an oxidized Hf metal film was used as a standard to subtract out the background resulting from the hafnium peak. The result of the as-deposited Hf metal film is shown in Figure 4-11. The majority of the peak occurs at a binding energy of 397.5 eV which is near the reported value of 396.3 eV for Hf-N. Granted the substrate temperature of 350 °C is not sufficient to promote a significant degree of bonding. Upon annealing the peak broadens out and shifts to higher binding energies, as shown in Figure 4-12. The broad peak is indicative of multiple bonding environs. The shift to higher binding energies during the oxidation anneals results from the nitrogen moving to the silicon interface. Si-N bonds have been reported to have values in the range of 398 to 399 eV. Furthermore upon annealing, the intensity of the signal diminishes. It is believed that a majority of the nitrogen within the metal film is replaced by oxygen when annealed. Comparing the UV to the non-UV annealed sample

(i.e. H4 and H5 respectively) shows a similar peak profile but a loss of intensity in the nitrogen signal. The UV radiation promotes the replacement of the nitrogen within the film and at the interface.

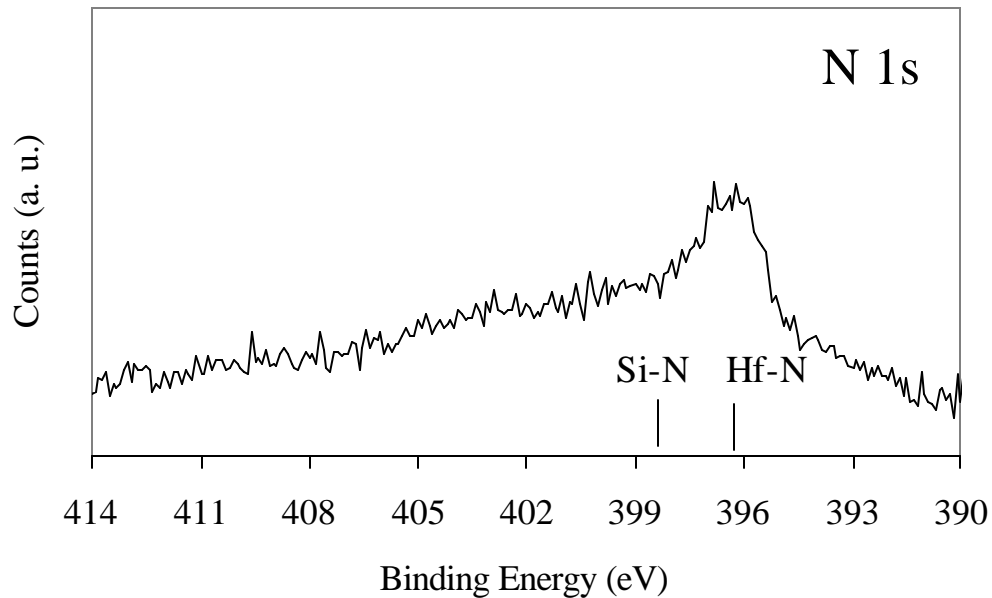


Figure 4-11: N 1s peak of as deposited nitrided Hf metal film.

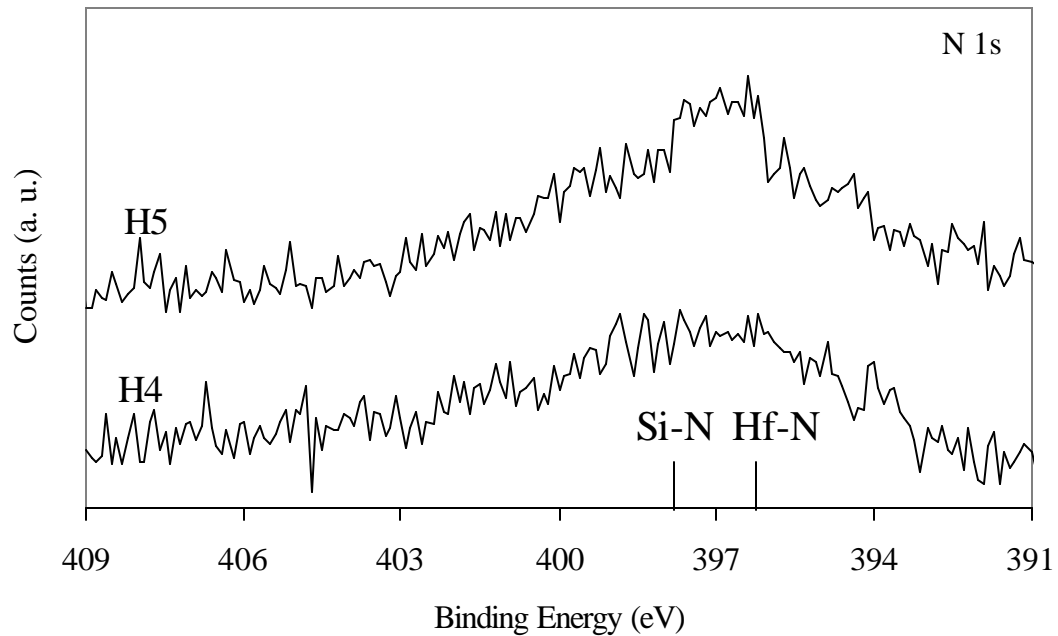


Figure 4-12: N 1s peak after PDA for samples H4 and H5.

Electrical Properties Analysis

Upon completion of the chemical and structural analysis, the sample surfaces were washed with acetone then methanol and blow dried with dry nitrogen. Then 1000 Å platinum electrodes were sputtered on the surface using a radio frequency (RF) sputtering system. The shadow mask used for this step had repeated sets of circular dots of various sizes. The size dot used for this portion of the experiments had an area of $4.66 \times 10^{-4} \text{ cm}^2$. A forming gas anneal was then carried out at 450 °C for 30 minutes in a flowing gas environment using a gas mixture of 4% H₂ and 96% N₂. The forming gas anneal step is important because the hydrogen passivates the defects between the surface of the metal and the film. The backside of the samples were then abraded and swabbed with a 1 % HF to remove any native oxide. The samples were then mounted on glass microscope slides using a silver paste which was then cured at 150 °C on a hotplate to remove the organic. The silver forms an ohmic contact with the p-type silicon for proper electrical data collection.

Capacitance-Voltage Results

Capacitance-voltage measurements were taken for a series of seven dots on each sample for both the 100 kHz and 1 MHz input frequencies to compare the frequency dependence on the capacitance response. Furthermore, scans were taken using both the parallel and series models. Figure 4-13 compares these results for sample H4, the UV-oxidized sample deposited in ammonia which overall had the best electrical characteristics of the samples. There is a large dependence of the capacitance on the frequency used for the measurement. This sample exhibited a 40% decrease in capacitance between the parallel models when going from 100 kHz to 1 MHz. The change in the response is mainly due to the choice of substrates. The low doping level of

$\sim 2 \times 10^{14} / \text{cm}^3$ provides very few charge carriers. Thus when in the accumulation region where a negative bias is being applied to the gate, the depletion region in the channel beneath the gate becomes large. As a result, the RC time constant for the carriers to move to respond to the frequency at which the voltage is being applied becomes significant when 1 MHz measurements are carried out. Thus the 1 MHz capacitance response is less than that of the 100 kHz. Ultimately films with no frequency dispersion are desired and the films should be tested on standard p-type wafers instead of the p- ones that were used. This plot also demonstrates the need to choose the proper model for the sample type being studied. For ultra thin film oxides ($< 100 \text{ \AA}$), like the samples in this work, the parallel model is best suited due to increased leakage resulting in a conductance term which must be taken into account.

The high frequency (1 MHz) parallel model scans were used for comparison of each of the samples. Figure 4-14 shows a plot of these results. From the graph it can be seen that the small incorporation of nitrogen into the films by depositing in ammonia greatly increases the capacitance of the film. This is attributed to limited interfacial layer formation during oxidation and a resulting high dielectric constant for the interface. Furthermore the use of UV-oxidation during post deposition annealing further improves the capacitance of the stack by increasing the quality of the hafnium oxide layer. The threshold voltage V_T for the samples also underwent a shift from $\sim -1.5 \text{ V}$ for sample H3, the non-irradiated, non-nitrided sample, to 0 V for sample H4. The curve response shape is also improved by nitrogen and UV-treatment suggesting minimization of interfacial and bulk defects such as oxygen vacancies. Thus combination of both nitrogen incorporation and UV-irradiation results in higher quality electrical characteristics.

From the capacitance response data, the oxide gate stack dielectric constant was calculated using equation 4-1. Thickness values used for the calculations for the films were taken from the XRR and VASE modeling results. The equivalent oxide thickness was calculated using equation 4-2.

$$\epsilon = \frac{C \times t}{A \times \epsilon_0} \quad (4-1)$$

$$EOT = \frac{3.9 \times \epsilon_0 \times A}{C} \quad (4-2)$$

ϵ = dielectric constant for the film

C = capacitance

A = area of the MOS capacitor

ϵ_0 = permittivity of free space

EOT = equivalent oxide thickness

Compilation from these calculations is presented in Table 4-4. The use of UV-irradiation and nitrogen incorporation into the films has been shown to produce film stacks with EOT values of less than 10 Å.

Table 4-4: Dielectric constants and EOT for samples H2-H4.

Sample ID	k	EOT Å
H2	10.6	18.8
H3	9.4	21.3
H4	21.0	9.1
H5	13.8	14.5

Repeatability

The sample set was repeated twice using the same experimental setup to confirm the results. Errors were estimated using the root mean square error method. From the results it is shown that the data is highly repeatable and yields nearly identical values between each set.

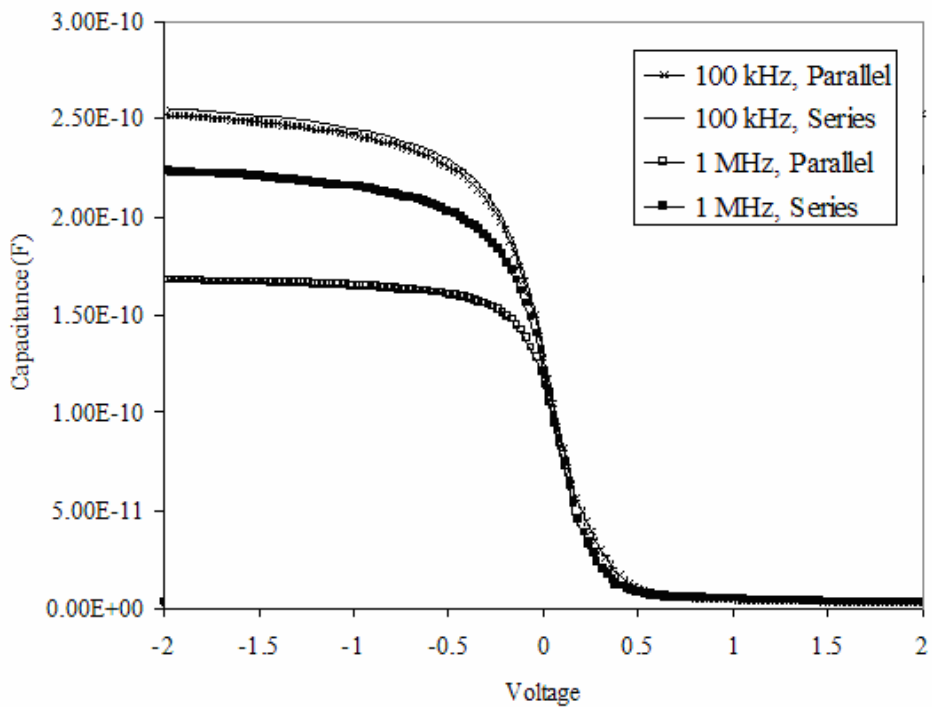


Figure 4-13: Comparison of high and low frequency capacitance responses for sample H4.

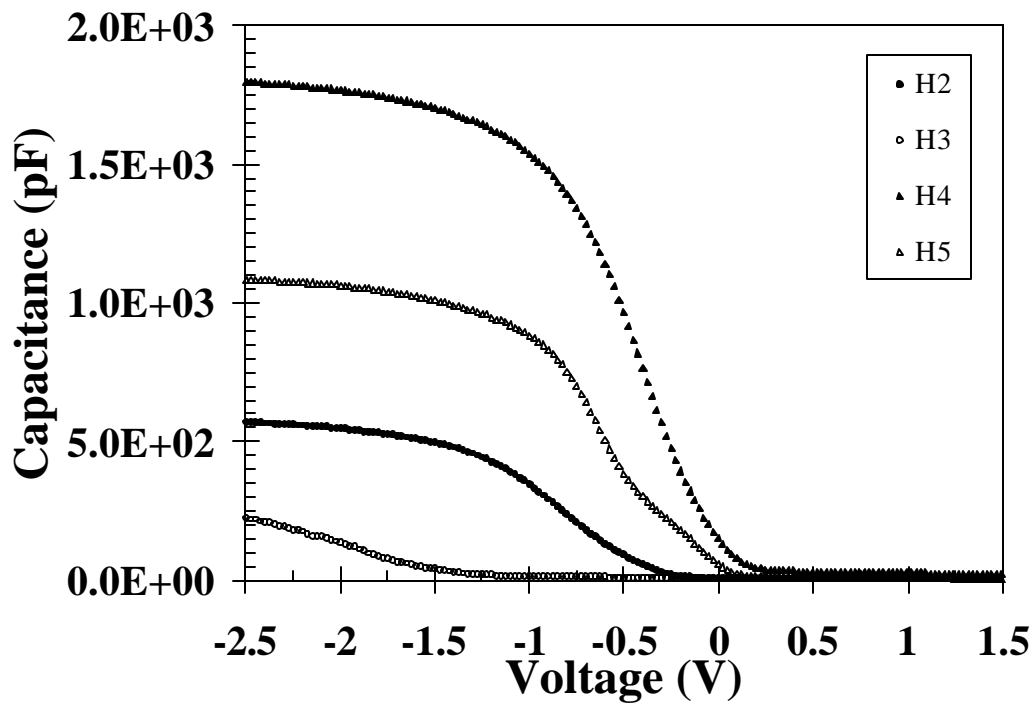


Figure 4-14: High frequency capacitance voltage responses for samples H2-H4.

Table 4-5: Repeatability study results for k and EOT of oxidized hafnium metal films.

Sample ID	Set 1		Set 2		Set 3		Avg. k	Avg. EOT Å
	k	EOT Å	k	EOT Å	k	EOT Å		
H2	10.6	18.8	10.5	19.0	10.8	18.6	10.6±0.1	18.8±0.1
H3	9.4	21.3	9.5	21.2	9.6	21.0	9.5±0.1	21.2±0.1
H4	21.0	9.1	20.9	9.3	21.2	8.9	21.0±0.1	9.1±0.1
H5	13.8	14.5	13.6	14.7	13.5	15.0	13.6±0.1	14.7±0.2

Interfacial Trap Density Measurements

The samples were sent to the University of Texas-Austin for further analysis.

Using a similar system setup to ours, capacitance voltage measurements were taken at 1 MHz in a parallel model mode. These results were then fit by the Terman method, discussed further in Appendix A, using an in-house Mathcad program which simulates the CV data based on the metals used for contacts and the known film thickness and contact area. The plots generated from the fits of the models give the quasi-static representation of the MOS stack. By comparing the fit to a curve generated based on an ideal film with no defects, an estimate of interfacial trap defect density, D_{it} , can be yielded. The results of the defect density calculations are given in Table 4-6. Figure 4-15 plots the data and the fits obtained from the three samples which could be modeled. Sample H3 was too poor of quality for any information to be properly fit by this method. All the samples had average defect densities ranging in order of magnitude from 10^{11} - 10^{12} /cm^2 . The UV-oxidized samples H4 and H5 had the highest defect densities. In order for an alternative high-k oxide to be used it must be able to compete with the low defect densities of 10^{10} 1/cm^2 obtained using silicon dioxide.

Table 4-6: Defect density results for samples analyzed at UT-Austin.

Sample ID	D_{it} (1/cm ²)
H2	3.07E+11
H4	2.18E+12
H5	1.73E+12

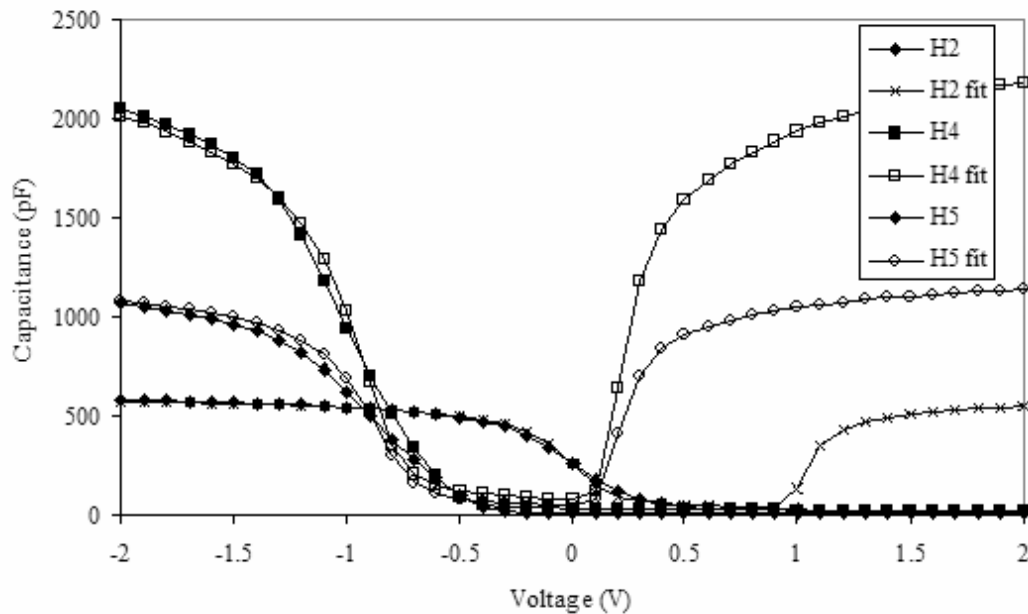


Figure 4-15: CV response and model fit data for samples H2, H4, and H5.

Current-Voltage Results

The current-voltage (IV) characteristics of the films were obtained by scanning MOS capacitors using a voltage range of -2 to 2 volts with the Keithly Win-82 measurement system. Figure 4-16 shows the IV results for the oxidized hafnium metal films. All samples exhibited leakage current densities of less than 5×10^{-4} A/cm² at voltages of -1.2 V. This is the standard operating voltage that industry uses to compare leakage. For a film to be used it must have leakages less than 1×10^{-2} A/cm² at this voltage to stay within the power consumption guidelines. Sample H4, which had the highest capacitance, exhibited the lowest leakage for both the negative and positive bias regions. The use of nitrogen incorporation and UV-assisted oxidation together provide a

synergistic effect creating higher quality films with less defects which promote leakage paths even though this film had the highest degree of crystallinity.

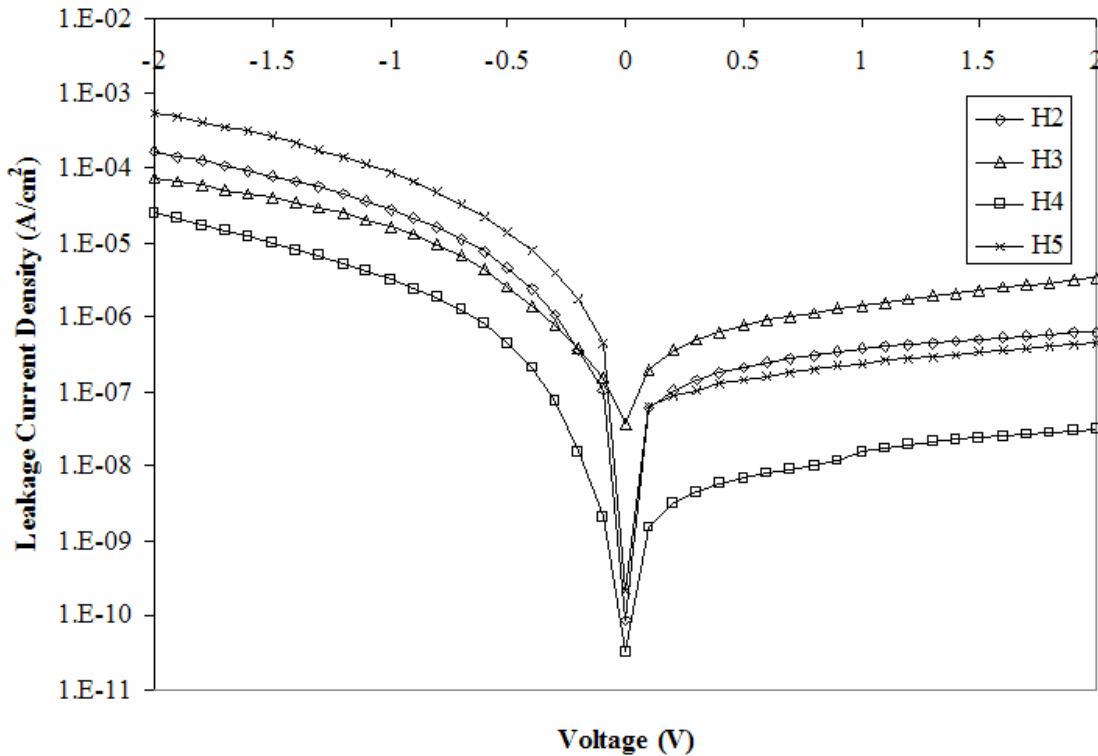


Figure 4-16: Current voltage results from oxidized hafnium metal films.

TEM Analysis

Cross sectional TEM samples were made from samples H4 and H5 to observe the film uniformity, crystallinity, and interface quality. Figures 4-17 and 4-18 depict a portion of samples H4 and H3 respectively. The thickness of the film and the interfacial thicknesses were measured from the micrograph. Sample H4 clearly shows signs of polycrystalline growth, evidenced by grains of roughly the size of the thickness of the film. EDS line scans were attempted but the drift was too great to get accurate readings across the thickness of the samples. The degree of sample tilt required ($\sim 10^\circ$) to acquire the measurement further hinders accurate elemental analysis. Scans taken at specific points in the interface region for both samples did show mostly Si and O with a trace

amount of Hf. From both the EDS and XPS results previously, the interface for all the samples is a distinct uniform SiO_2 layer (nitrogen is unable to be detected using this analysis technique). Ultraviolet radiation was shown to increase the growth of the interfacial layer. However by incorporating nitrogen into the film during deposition, the growth of the layer is hindered.

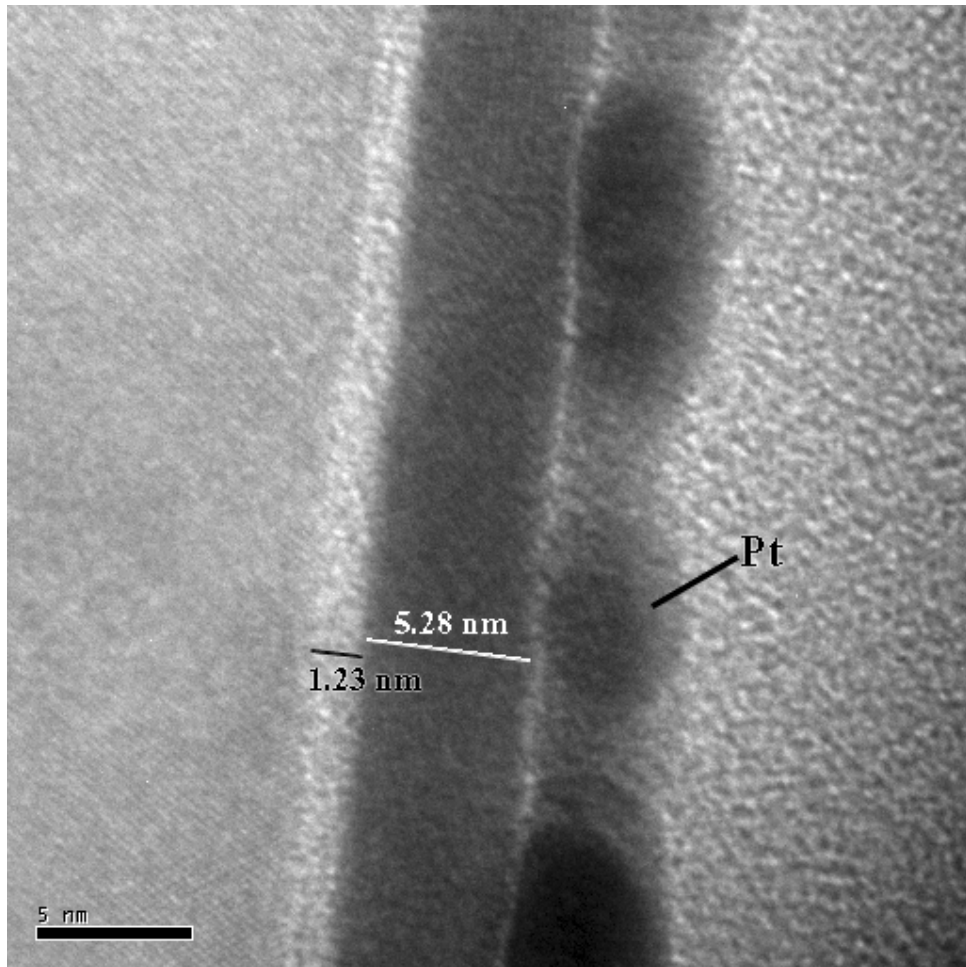


Figure 4-17: XTEM of the UV annealed nitrided sample H4.

Proposed Model

Based on the data from this set of four samples, UV radiation during the oxidation anneal promotes crystallization which, in and of itself, is a detrimental quality for the gate oxide. A polycrystalline film has grain boundaries which act as leakage paths for current

through the film and also serve as diffusion pathways for oxygen and other contaminants. Furthermore, UV radiation promotes oxidation of the interface, thus parasitically reducing the benefits of using a high-k dielectric. The benefits of UV radiation, however, are improved oxygenation of the film and reduction of physiaborbed and physically trapped oxygen. Lower temperatures can be used to fully oxidize the film and eliminate sub oxygen species. Thus UV radiation promotes the formation of higher quality oxide films.

In order to counter some of the detrimental effects of UV-assisted processing, nitrogen was incorporated into the film during deposition. The nitrogen was shown to reduce the formation of the interfacial silicon dioxide layer by both acting as a diffusion barrier to the oxygen and by the oxygen preferentially replacing the nitrogen within the film structure. The XPS results suggest a thin silicon nitride layer was formed at the interface. Nitride barrier layers have been used as oxygen diffusion barrier layers for years in the semi-conductor industry. An ultra-thin nitride layer will slow the reaction of the highly active oxygen species created by UV radiation. Furthermore, hafnium has a greater affinity for oxygen. The thermodynamics behind the reactions favor the formation of hafnium oxide over hafnium nitride. Therefore with an overpressure of oxygen species and no nitrogen during the oxidation anneal, the oxygen replaces the nitrogen within the structure and also drives out the physically trapped nitrogen. Ultimately nitrogen incorporation of the films controls the interface quality of the films, thus countering the detrimental effect of UV-assisted processing. Figure 4-19 shows a schematic of the effects of UV and nitrogen on the films.

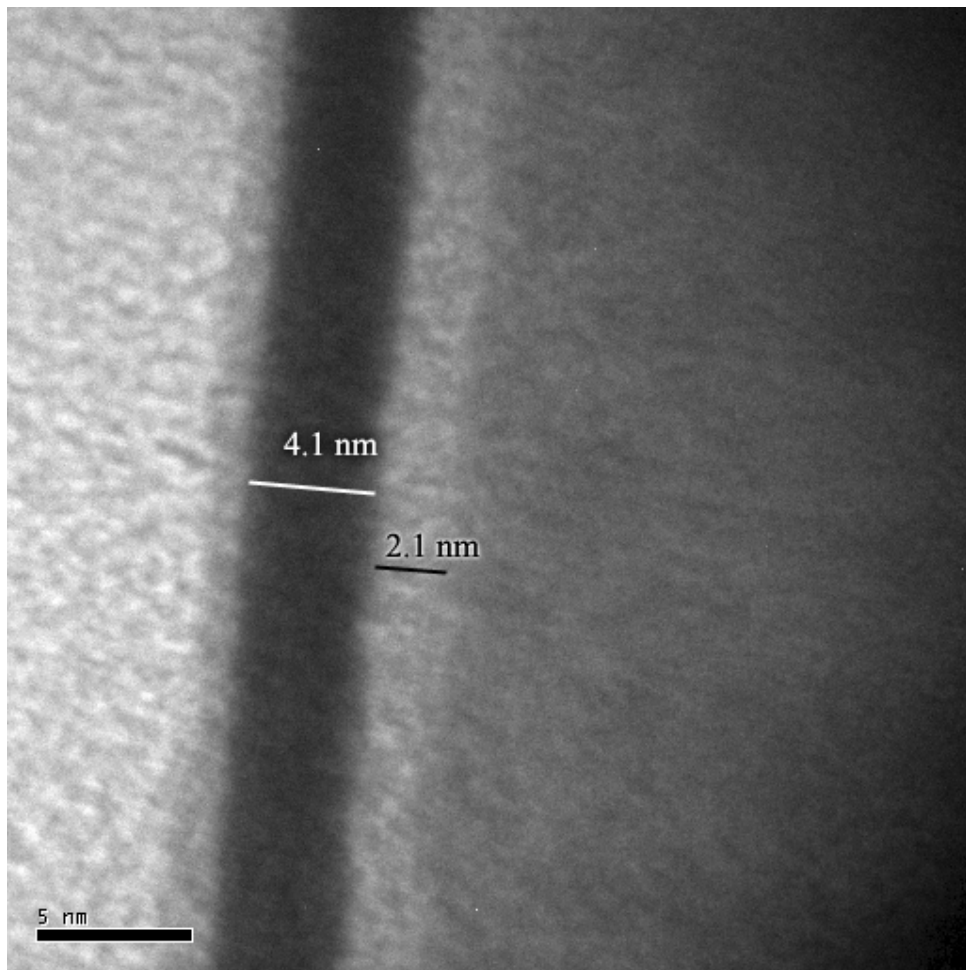


Figure 4-18: XTEM of non UV annealed hafnium film H3.

Results and Discussion of the High Temperature Depositions

The motivation behind this set of samples was to first attempt to increase the degree of nitridation of the films during deposition by increasing the substrate temperature during processing. Then comparisons in the use of UV during high temperature deposition and annealing after were made to judge the effect of UV on the nitridation and film structure. Ultimately electrical measurements were conducted on these samples to compare the low temperature and high temperature processing methods.

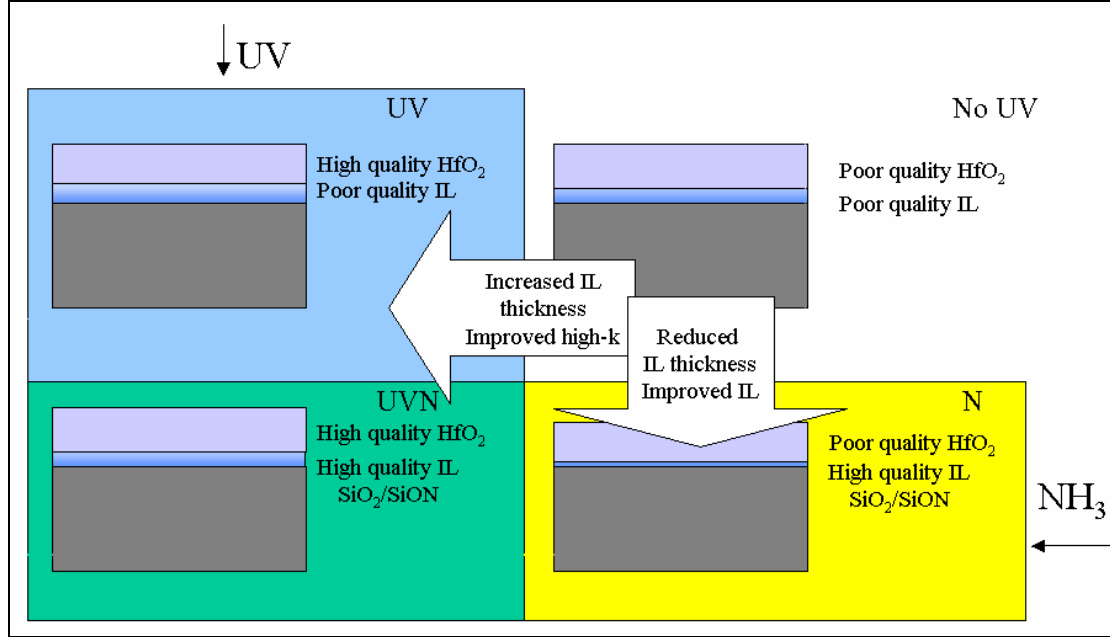


Figure 4-19: Model of the effect of UV and nitrogen.

XPS

Elemental analysis carried out by comparing the area of the scans for the O 1s, N 1s, Hf 4f, and Si 2p regions and then taking into account for the sensitivity factors yielded nitrogen percentages of 4-5 atomic % for all four samples. Therefore by depositing using substrate temperatures of 650 °C an additional 1-2% of nitrogen can be incorporated into the films. Figure 4-20 shows the comparison of the O 1s peaks for these samples. Figure 4-21 compares the Hf 4f peaks for these samples. These films were thicker than previous samples, ranging from 80-120 Å, so detailed Si 2p peaks were difficult to obtain due to the weak signal resulting from the large escape depth that the electrons from the Si atoms near the interface have to travel.

The O 1s peaks for the UV deposited samples (HN1 and HN4) exhibit a higher energy shoulder suggesting ~10-15% more Si-O type bonding environs. This is believed to be a result of initial crystallization of the films during deposition resulting in a higher

percentage of grain boundaries for the diffusion of oxygen to the interface. Thus upon annealing the oxygen can readily move to the interface to react with the silicon.

The Hf 4f peaks were all identical in shape, position, and ratio of the 4f 5/2 and 4f 7/2 peaks. Therefore UV does not affect the main bonding in the bulk of the hafnium oxide layer.

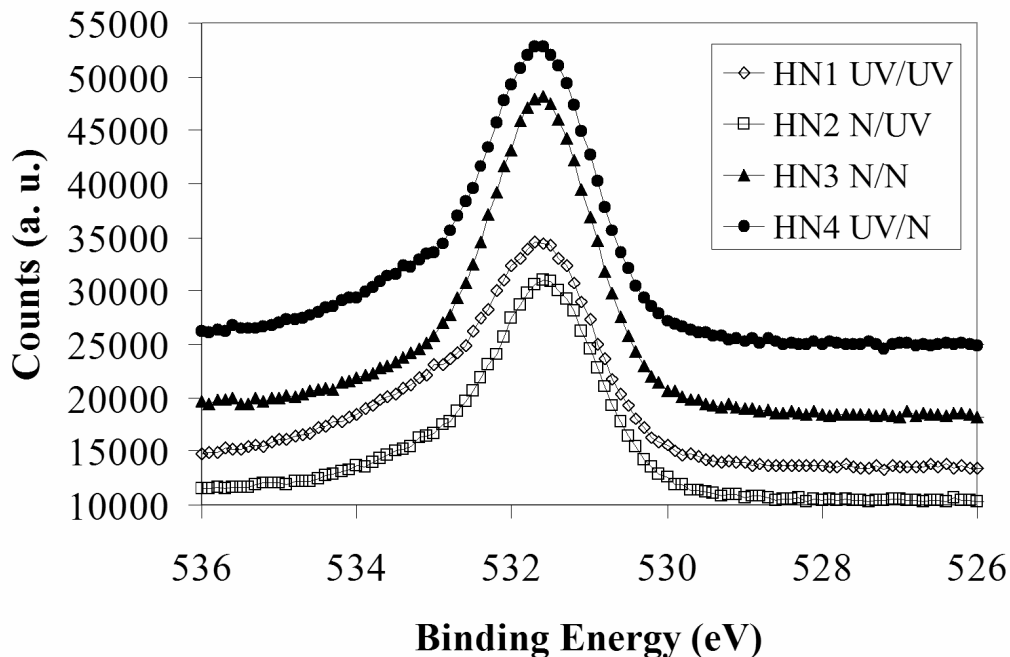


Figure 4-20: O ls peaks for the high temperature deposited sample set.

X-Ray Analysis

Glancing incidence angle measurements were made at $\Omega=0.5$ for all the samples and are plotted in Figure 4-22. All of the samples exhibited a high degree of crystallization. The FWHM for the (111) peak located at $\sim 28^\circ$ of the UV deposited and UV annealed sample (HN1) was 0.1° narrower than the other samples suggesting a slightly greater degree of crystallinity possibly due to crystal growth. This result follows

the previous observance of the promotion of crystallization resulting from using UV during processing.

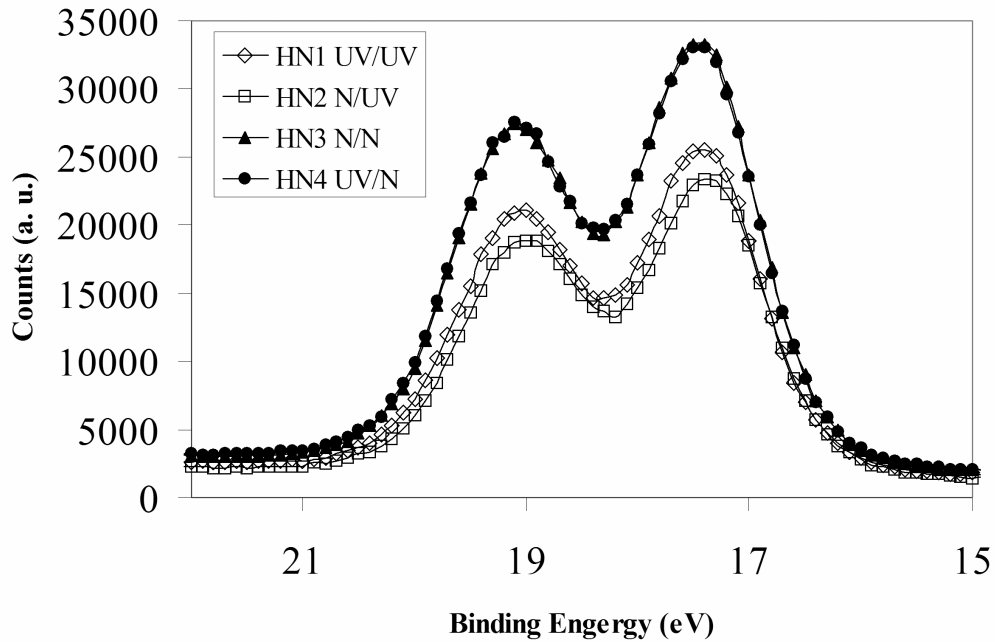


Figure 4-21: Hf 4f peaks for the high temperature deposited sample set.

X-ray reflectivity scans were also taken for all of the samples and are plotted along with the models in Figure 4-23. The XRR scans show that UV during deposition increases the growth of the interface layer as was predicted from the XPS O 1s scans. Furthermore, the film processed without UV for both the deposition and anneal has the least amount of interfacial oxide growth. The interface density is larger than SiO₂ for all the samples suggesting either there is mixing of SiO₂ and HfO₂. The higher density also could result from nitridation of the interface as the density of silicon nitride is ~4-5 g/cm³. Low roughness values for the interface and the film layer suggest abrupt interfaces and relatively smooth uniform films.

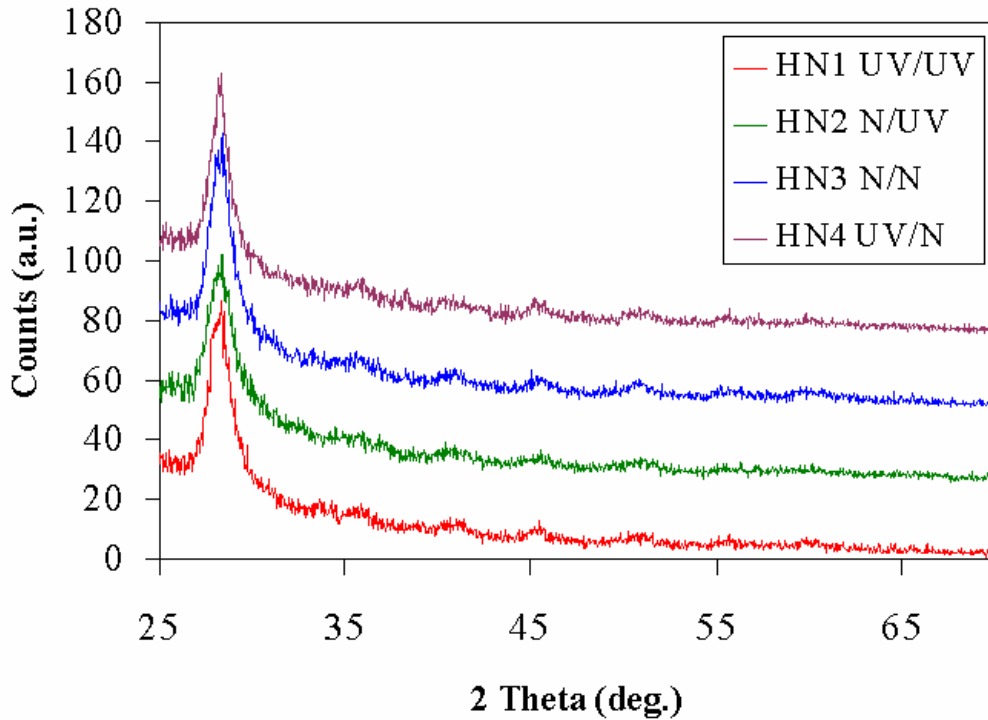


Figure 4-22: GIXD for the high temperature deposited samples taken at $\Omega = 0.5^\circ$.

Electrical Characterization Results

Capacitance/voltage and current/voltage measurements were taken for the high temperature deposited sample in a similar manner to the previous samples. The results of the capacitance/voltage measurements are shown in Figure 4-24. The data set HN1 was offset to avoid confusing overlap with HN3. From the results it is shown that UV during the deposition is detrimental to the electrical properties of the film especially when the sample is not UV annealed during the oxidation step. Sample HN4 (deposited with UV and annealed without UV) exhibits similar characteristics to the Si_xN_y samples that were first produced. The response has a large stair step due to electrical traps and then falls off at large negative bias. Similarly, sample HN3 (deposited and annealed without UV) exhibits a stair step in the depletion region. Upon UV oxidation annealing, the defects

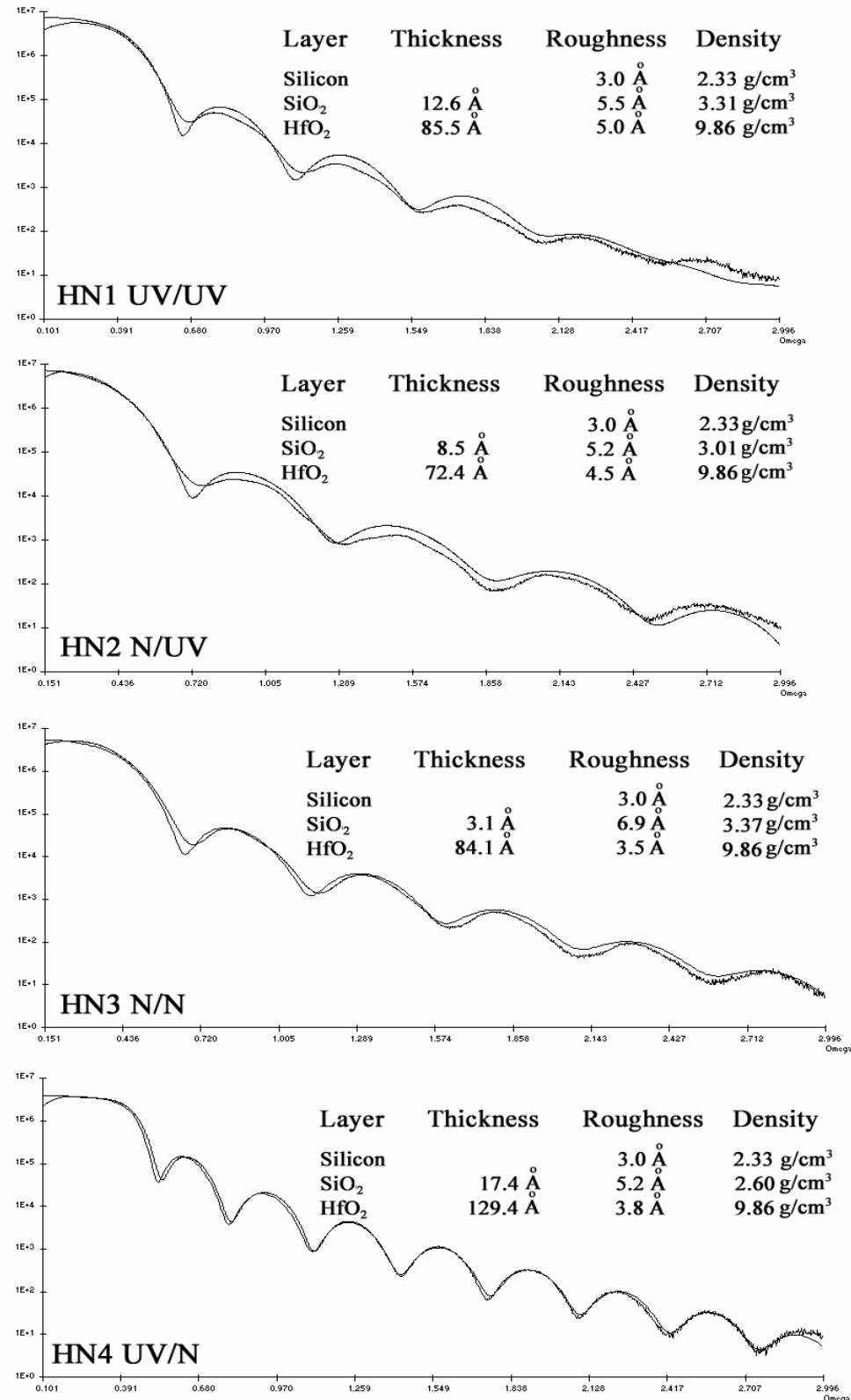


Figure 4-23: XRR plots and models for the high temperature deposited samples.

are eliminated. The estimated k and EOT values for these films were calculated and are tabulated in Table 4-7. The highest k obtained was 13.8 for sample HN3 (no UV during deposition or annealing) with an EOT of 27.5 Å. The higher temperature during processing is hindering the capabilities of the material to reach k values of the expected 25 for HfO₂.

Leakage currents were measured using a bias scan from -4 to +4 V. Larger scan ranges were not possible for two of the samples because they were leaky and exceeded the compliance current preset in the Keithley equipment before the full bias range could be completed. The IV results plotted in Figure 4-25. The samples which were UV annealed exhibited the lowest leakage currents. Furthermore, UV during deposition causes a 1-2 order of magnitude increase in leakage. This could be a result of UV causing crystallization during deposition which creates a poorer initial film with many grain boundary leakage paths. By UV annealing the samples during oxidation, the oxygen defects and many of the interface traps are eliminated and thus the leakage is reduced.

Table 4-7: EOT and k for the high temperature deposited samples

Sample ID	EOT Å	k
HN1 UV/UV	41.4	11.5
HN2 N/UV	33.1	12.2
HN3 N/N	27.5	13.8
HN4 UV/N	82.5	5.7

Discussion

From XPS, UV radiation during deposition did not improve the quantity of nitrogen incorporated into the films but does increase the subsequent formation of interfacial oxide

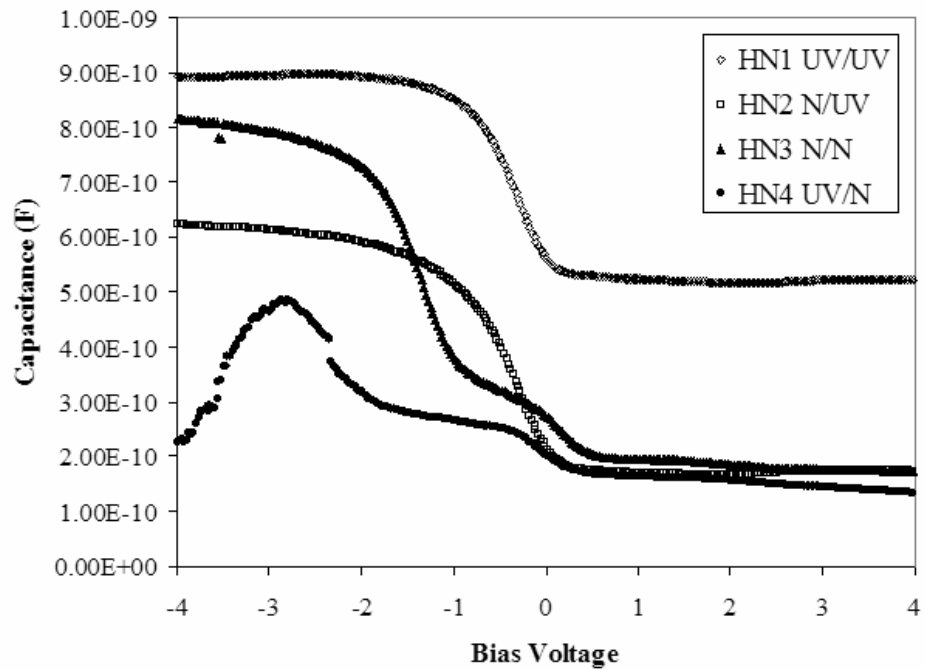


Figure 4-24: CV plots for the high temperature deposited samples

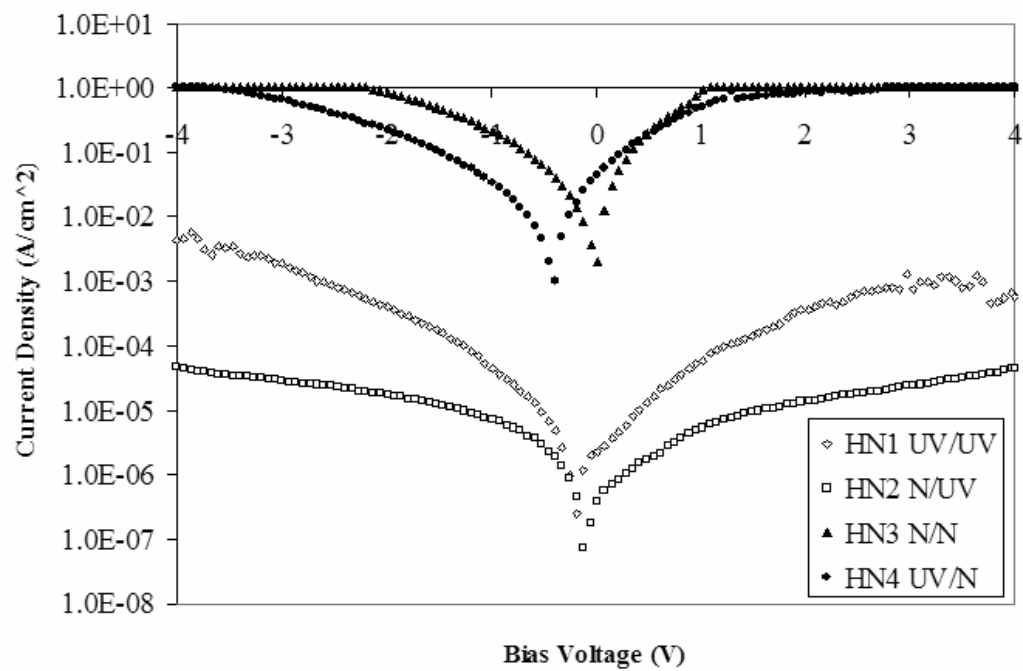


Figure 4-25: IV plots for the high temperature deposited samples

upon annealing. This result is supported by the XRR results. From the electrical data, the UV radiation during deposition increased the leakage in the films by 1-2 orders of magnitude. Furthermore degradation of the capacitive response occurs if the samples were not annealed in UV after deposition. Use of UV during the oxidation anneal is key to eliminating the oxygen defects and charge trapping defects present within the films. This is clearly shown by the elimination of the stair step within the depletion region of the CV curve and the larger slope of the response curve.

Summary

Hafnium metal films were deposited using PLD in both residual vacuum and UV-excited ammonia and were then annealed in-situ in O₂ both with and without UV. It was shown that the UV-radiation caused greater crystallinity and roughness in the films due to the non-thermal energy source that the radiation provides promoting nucleation and growth of small randomly oriented crystallites below the crystallization temperature of the film. XPS analysis showed that the UV-radiation promoted the formation of a mixed HfO₂/SiO₂ interface layer. Nitrogen incorporation was shown to reduce the formation of the SiO₂ layer, counteracting the detrimental effect of the UV-oxidation process.

By combining both the nitrogen incorporation and UV-oxidation step films with EOT of less than 10 Å can be obtained. Leakages values which meet the industry standard were also realized using this process. The D_{it} for the films was two orders of magnitude higher than that for silicon dioxide gate oxide layers, so more work must be done to bring this level down into an acceptable range. By understanding the effect of nitrogen and UV-assisted oxidation of metal films, higher quality films with low interfacial formation can be produced.

CHAPTER 5

UV-ASSISTED OXIDATION AND NITRIDATION OF HAFNIUM ALUMINUM METAL ALLOY FILMS

Aluminum additions have been shown to increase the crystallization temperature and stabilize high-k oxides so they can withstand the higher temperature processing steps which are encountered after deposition.^{34, 70-72} This portion of the work extends these investigations to the UV and nitrogen treated sample sets from the previous section to understand the role aluminum has on the electrical and structural properties of the film.

Experiment

A 248 nm KrF excimer laser system in a typical pulsed laser deposition (PLD) setup with the multi-target carousel was used to alternatively ablate a hafnium metal target, 99.95% pure, and an Al metal target, 99.95% pure, from SCI Engineered Materials. Pulse ratios of 1:1, 1:2, and 1:3 for the aluminum and hafnium targets were used and the total pulse count was 1500 for target thicknesses after oxidation of 80-100Å. The deposition parameters used were laser fluence of 3.0 J/cm² at a 5 Hz pulse rate. The films were deposited at 350 °C on p⁻(100) Si substrates from MEMC that were cleaned using an SC1 solution. This solution contains 80 vol% distilled water, 16 vol% hydrogen peroxide diluted to 30 vol% in distilled H₂O, and 4 vol% ammonium hydroxide. The samples were then dipped in a 1% HF solution for ten minutes to remove the native oxide. Depositions were performed either under residual vacuum at 1x10⁻⁶ Torr or under 300 Torr of ammonia. Post deposition anneals were carried out in-situ in 300 Torr of O₂

at 400 °C with the Hg lamp array on for 30 minutes. A summary of the sample matrix is given in Table 5-1.

Table 5-1: Sample deposition conditions

Sample ID #	Pulse Ratio	1x10 ⁻² Torr Ammonia
AH1	1 Al: 1 Hf	No
AH2	1 Al: 2 Hf	No
AH3	1 Al: 3 Hf	No
AHN1	1 Al: 1 Hf	Yes
AHN2	1 Al: 2 Hf	Yes
AHN3	1 Al: 3 Hf	Yes

Crystallinity comparisons and phase identification was done using grazing incidence x-ray diffraction (GIXD, Panalytical X’Pert system). The chemical bonding and composition of the films was investigated by x-ray photoelectron spectroscopy (XPS, Perkin Elmer 5100) using Mg K_α radiation (1253.6 eV). Finally MOS capacitors were fabricated by sputter deposition of 1000 Å thick platinum electrodes using a shadow mask having circular dot patterns of various sizes. Capacitance voltage and current voltage measurements were taken using a Keithley Instruments Inc., 590 capacitance meter, KI236 source measurement unit (SMU), and the Kiethley Instruments Inc. Win-82 measurement system.

Samples AH3 and AHN3, which contained the least amount of aluminum were then annealed in a conventional tube furnace at 900° C for 1 minute under a flow of N₂ to simulate an extreme rapid thermal annealing condition which might be encountered in an industrial process. GIXD scans were taken for these samples to observe any change in crystallization temperature with the addition of aluminum.

X-Ray Analysis

Upon examination of the x-ray data collected, it was shown that aluminum additions eliminated the crystallization caused by UV-radiation at the oxidation temperature of 400 °C. GIXD spectra taken at $\Omega=1^\circ$, plotted in Figure 5-1, for samples H2, AH3, and AHN3 show a marked decrease in crystallization after the UV-assisted oxidation treatment with samples AH3 and AHN3. Thus the aluminum addition increases the crystallization temperature of the film at least to an extent to overcome the irradiative effect of the UV radiation.

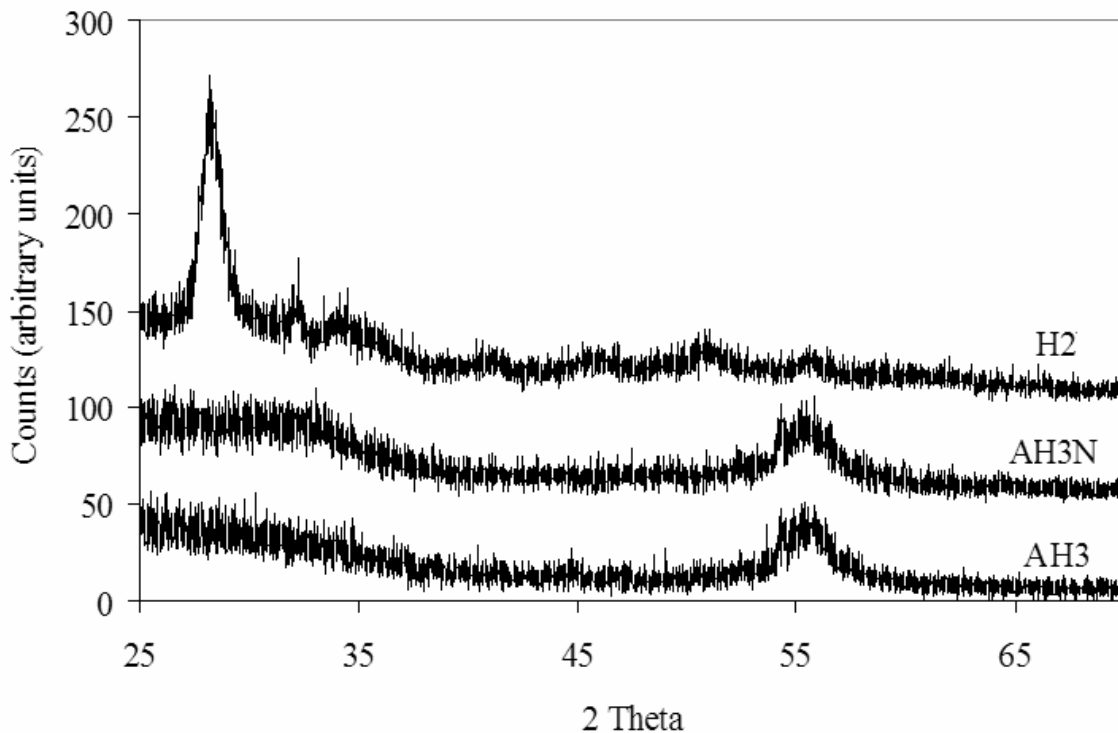


Figure 5-1: GIXD scans taken at $\Omega=1^\circ$ comparing the effects of aluminum additions in samples AH3 and AHN3 to sample H2.

Compositional Comparisons

XPS was used to determine the composition and bonding environmental changes in the films. Surveys from 0-1000 eV were taken for all the samples to first determine the

elemental makeup and to detect any contaminates. Then a multi-plex consisting of the C 1s, O Auger, O 1s, N 1s, and Hf 4d peak regions were collected. The elemental percentages were obtained from the surveys and converted to molar percentages for the HfO₂ and Al₂O₃ compounds. Results from this analysis are given in Table 5-2.

Table 5-2: Sample composition from elemental analysis using XPS.

Sample ID#	HfO ₂	Al ₂ O ₃	N
AH1	53.8%	46.2%	---
AH2	77.7%	22.3%	---
AH3	89.4%	10.6%	---
AHN1	67.0%	29.0%	4%
AHN2	82.2%	15.8%	2%
AHN3	92.4%	5.6%	2%

The hafnium metal target was shown to have a greater deposition rate than the aluminum target, thus for the samples with 1:1 pulse ratios the hafnium oxide content after oxidation was greater than the aluminum oxide. This effect is even greater when the samples were deposited in ammonia. The marked increase in hafnium oxide in these films is attributed to the higher mass density of the atoms. Because of the greater mass of the particles being ablated, less scattering due to the ammonia gas atoms occurs and a more uniform plume dynamic results.

The molar fraction results were then converted to volume fractions by taking the relative mass of each present and dividing by the tabulated densities of 9.68 g/cm³ for HfO₂ and 3.98 g/cm³ for Al₂O₃. The bulk dielectric constant of the film can be estimated from this result. In a paper by D. Young, et al.⁷² it was shown that finely dispersed mixtures of two dielectric materials yield a bulk dielectric constant that follows a logarithmic mixing rule. This relationship is given by:

$$\log k_{\text{bulk}} = \sum_i v_i \log k_i \quad (5-1)$$

where k_{bulk} is the dielectric constant of the mixture, v_i is the volume fraction of each component, and k_i is the respective dielectric constant for each component. Table 5-3 shows the predicted dielectric constant for each of the films.

Table 5-3: Predicted film density and bulk dielectric constant.

Sample ID	Mole Fraction HfO ₂	Mole Fraction Al ₂ O ₃	Density g/cm ³	Volume Fraction HfO ₂	Volume Fraction Al ₂ O ₃	Bulk k
AH1	0.54	0.46	7.04	0.74	0.26	19.2
AH2	0.78	0.22	8.40	0.89	0.11	22.5
AH3	0.89	0.11	9.07	0.95	0.05	23.9
AHN1	0.69	0.31	7.91	0.84	0.16	21.3
AHN2	0.83	0.17	8.72	0.92	0.08	23.1
AHN3	0.93	0.07	9.30	0.97	0.03	24.4

Electrical Characterization Results

Upon completion of the chemical and structural analysis, the sample surfaces were washed with methanol and blow dried with dry nitrogen. Then 1000 Å platinum electrodes were sputtered on the surface using a radio frequency (RF) sputtering system. The shadow mask used for this step had repeated sets of circular dots of various sizes. The size dot used for this portion of the experiments had an area of $4.66 \times 10^{-4} \text{ cm}^2$. A forming gas anneal was then carried out at 450 °C for 30 minutes in a flowing gas environment using a gas mixture of 4% H₂ and 96% N₂. After MOS devices were fabricated capacitance-voltage and current-voltage measurements were taken with the Keithly Instruments Win-82 system.

For the capacitance-voltage measurements, voltage was scanned from -3 to +2 V using the 1 MHz, parallel model setup. Compilation of the results from the six samples is presented in Figure 5-2. Additions of aluminum into the films were shown to decrease the capacitance as was expected. Bulk aluminum has a dielectric constant of 9 compared

to 25 for HfO_2 . The samples without nitrogen exhibit a large flat band voltage shift of $\sim 2\text{V}$. The shift is due to an increase in the amount fixed charge within the layer caused by the aluminum addition.³⁴ Furthermore, the slope of the response decreases as aluminum is added. The slope of the curve is highly dependent on the concentration of interfacial traps. It is concluded that the aluminum creates higher concentrations of these traps.

By depositing the samples in ammonia, it can be seen that a more stable capacitance response is obtained. The nitrided samples exhibit almost no shift in the flatband voltage and have similar slopes. Therefore the nitrogen helps to passivate the effect of fixed charges from the aluminum and also eliminates a majority of the interfacial traps.

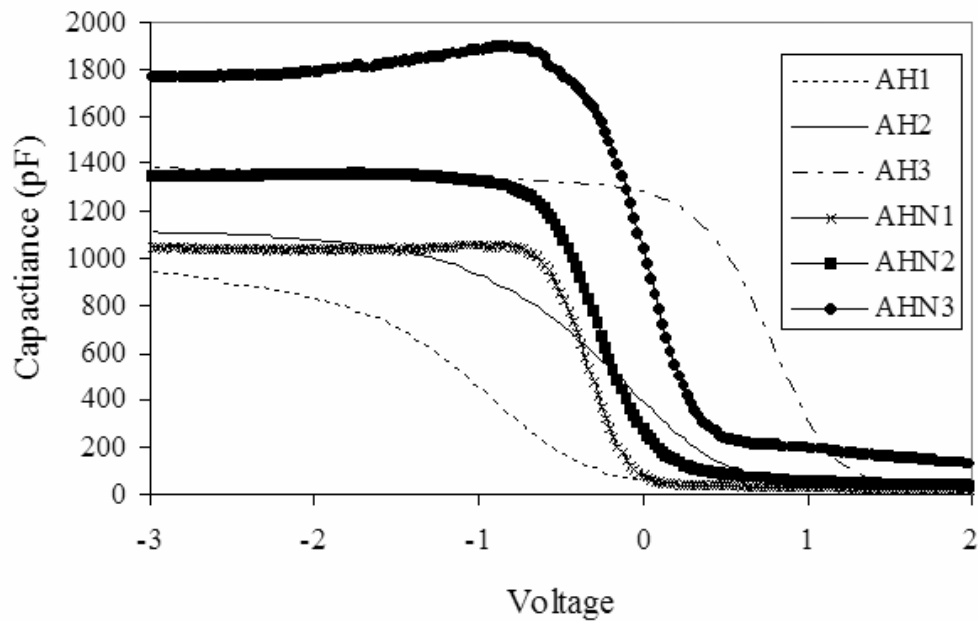


Figure 5-2: Compilation of the capacitance-voltage results from the aluminum addition samples.

Table 5-4 gives the bulk dielectric constants and the EOT for each based on 80-100 Å film thicknesses from VASE modeling. The resulting dielectric constants were lower than the predicted ideal values due to the formation of a lower dielectric constant interfacial layer which has been seen in all previous experiments.

Table 5-4: Dielectric constants and EOT for the aluminum study samples.

Sample ID	Dielectric Constant	EOT (Å)
AH1	10.1	39.6
AH2	11.6	34.5
AH3	17.2	23.3
AHN1	11.3	35.4
AHN2	15.8	25.3
AHN3	20.4	19.6

Current-voltage measurements were then scanned from -3 to 3 V for all the samples. The average leakage current density for each sample is presented in Figure 5-3. The samples deposited without nitrogen have an average of two orders of magnitude lower leakage current densities. This has been attributed to the increased growth of the interfacial layer. All the samples exhibited leakage values which fit the industry standard requirements; however, this is somewhat misleading as the samples are thicker than would be used if implemented into a device, as the EOT needs to be less than 10 Å. Further analysis using thinner samples must be carried out before these films would be deemed worthy as replacement gate oxide materials.

High Temperature Anneal

All the samples were subjected to a 900 °C RTA in flowing N₂ for 1 minute. After the anneal GIXD measurements were taken for the films. Figure 5-4 shows the result from sample AH3 which contained only ~11% Al₂O₃. No crystallization was detected for these films. Previous reports have suggested that ~30% Al₂O₃ is necessary to achieve

crystallization temperatures above 900 °C.

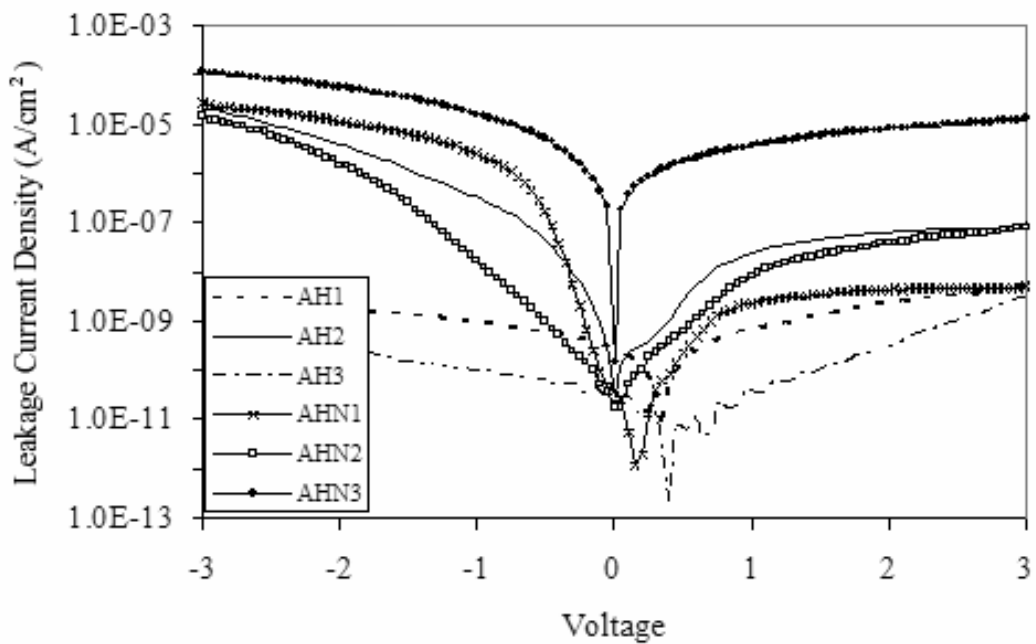


Figure 5-3: Compilation of the current-voltage results from the aluminum addition samples.

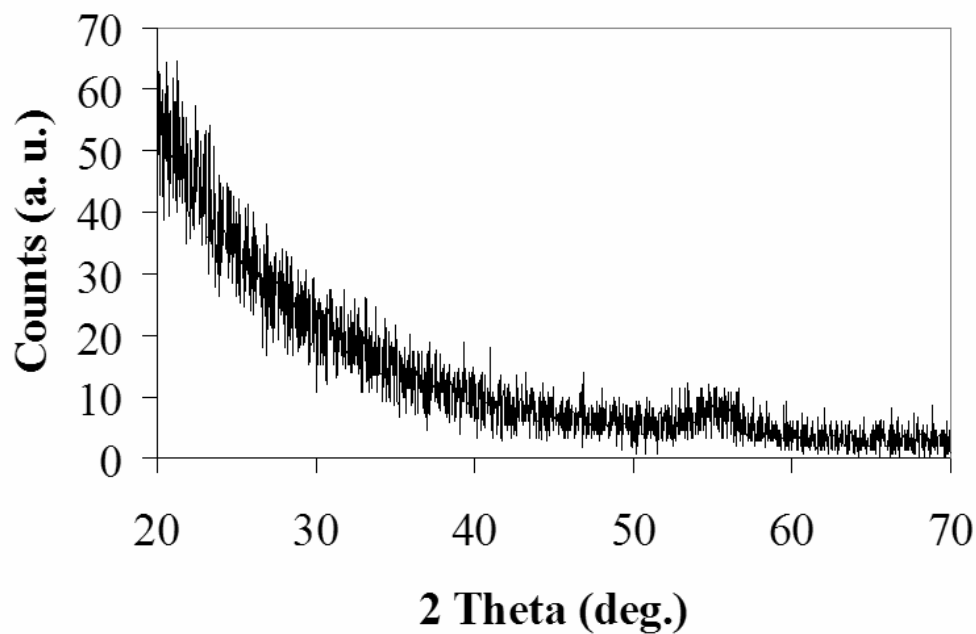


Figure 5-4: GIXD for sample AH3 annealed at 900 °C

Summary

The experiments from the second portion of this dissertation were extended in this chapter to study the effect of aluminum additions. It was shown that aluminum increased the crystallization temperature of the films sufficiently to counteract the crystallization which was resulting from the UV-assisted oxidation process. Furthermore aluminum was shown to drastically hinder the capacitance response of the films with respect to bulk and interface traps, as well as, reduction of the dielectric constant. Incorporation of nitrogen into the aluminum/hafnium metal alloys during deposition increased the stability of the films by eliminating fixed charge from the aluminum and by reducing the amount of interfacial layer formation.

CHAPTER 6 CONCLUSIONS

Since $\text{SiO}_2/\text{SiON}_x$ is vast approaching its physical limits for use in MOSFET device structures, there exists a driving force to replace the existing SiO_2 layer with an alternative layer with a higher dielectric constant. Though many research teams have investigated numerous different materials in an attempt to accomplish this goal, to date, none have succeeded due to new problems associated with the formation an unwanted low-k interfacial layer which forms between the silicon substrate and the dielectric material. The studies associated with this dissertation addressed the issues related to the kinetics of the interfacial layer formation of pulsed laser deposited HfO_2 films, the use of nitrogen incorporation during deposition of Hf metal films, post deposition oxidation using UV radiation, and additions of aluminum.

First, experimentation was conducted whereby ultrathin HfO_2 samples were deposited using varying temperatures and oxygen pressures. From the various characterization techniques, it was determined that the films deposited by pulsed laser deposition exhibited an interfacial layer even for samples that were deposited at 200 °C in very low oxygen pressures. The nature of the interface in all the samples was shown to be a physical mixture of HfO_2 and SiO_2 . No intermediate silicate structures were found to form. Increased deposition temperature caused increases in the interfacial layer thickness. The log of the pressure was shown to linearly increase the layer thickness formation. By understanding the kinetics, better control of the unwanted interfacial layer can be realized.

UV-assisted oxidation of metal films provides a lower temperature process whereby high-k films can be produced. However, UV radiation hinders the film properties by promoting crystallization and interfacial layer formation. It was found that small additions of nitrogen into the film during deposition by depositing in ammonia help to counteract the detrimental effects of the UV-assisted oxidation step. The nitrogen prevents diffusion of the highly reactive oxygen species to the interface and eliminates a majority of the bulk oxygen defects usually seen with PLD samples.

To control the crystallization temperature of the films, aluminum additions were studied. The as-deposited samples all were amorphous even after the UV-assisted oxidation step. Aluminum increases the crystallization temperature of the films at least to an extent at which the energy from the UV-radiation does not cause crystallization. The electrical characteristics of the films show that aluminum degrades the capacitance response by first decreasing the dielectric constant as it is a lower-k material. Furthermore, aluminum was shown to greatly shift the flatband voltage due to a greater amount of negative fixed charge as the concentration was increased. Finally the samples with higher concentrations of aluminum had increased interfacial defect densities shown by the decrease in the capacitance response slope. By adding nitrogen into the alloy during deposition, the flatband voltage was stabilized and the concentration of interface traps was reduced.

Studies in this dissertation indicated that there is development of an interfacial layer during deposition which can be controlled by using a combination of nitrogen and UV treatment to yield samples with acceptable electrical characteristics for use as an alternative gate dielectric material. The addition of UV radiation was shown to provide

beneficial removal of oxygen defects in the film but also detrimentally increased the interfacial layer formation and crystallization in the film. Depositing the Hf metal films in ammonia incorporates a small amount of nitrogen into the film. The nitrogen acts as a getter for the oxygen and slows the diffusion of oxygen species to the interface. Thus in effect the nitrogen counters the detrimental effects associated with UV-assisted oxidation. Further improvements of the films were made by depositing alloys of Hf and Al to increase the crystallization temperature of the films.

APPENDIX A ELECTRICAL DATA EXTRACTION METHOD

When conducting electrical characterization, once the proper model has been chosen for the with the Metrics ICS software, measurements may be acquired and a significant amount of information may be extracted from this data. For example, by calculating the total fixed charge in a MOS stack, numerous other important data are generated from the process. The derivation of the fixed charge will be done as an example.

It is important to first get a current-voltage measurement from one of the MOS devices to determine an appropriate diode to make capacitance-voltage measurements on. That is, a diode with a high breakdown voltage and turn on characteristics. Once this is determined, a high frequency/quasistatic output from the Win-82 system may be generated. A typical result for a p-type wafer is shown in Figure 2-11. While both curves are important, for this process, the calculations will be based off the high frequency curve. The first step is to use the CV curve to calculate doping concentration in the substrate. This is done by plotting the reciprocal of the square of the capacitance versus the gate voltage. The new plot should exhibit a linear region. By taking the slope of the linear region, it is possible to calculate the doping in the semiconductor. It is important to note that curvature in this region may represent nonuniform doping in the semiconductor. The equation for determining the doping is shown below:

$$N = \frac{2}{q\epsilon_s A^2 (\text{slope})} \quad (\text{A-1})$$

where q is the electric charge, ϵ_s is the semiconductor dielectric constant, A^2 is the gate area, and N is the doping (acceptor or donor). With the value, it is now possible to calculate the Debye length (L_D).

$$L_D = \sqrt{\frac{\epsilon_s k T}{q^2 N}} \quad (\text{A-2})$$

where k is the Boltzmann constant and T is temperature in Kelvin. With this value the semiconductor flatband capacitance can be calculated.

$$C_{FBS} = \frac{\epsilon_s A}{L_D} \quad (\text{A-3})$$

The next step is to calculate or experimentally determine the capacitance of the dielectric layer (C_i). In the scenario described here, the capacitance has been measured and represents the value of capacitance of the high frequency curve in the accumulation region. This typically is taken at a value of minimal leakage current, as ascertained by the previous IV measurements. If, one was unable to measure the capacitance, but had knowledge such as the thickness of the dielectric layer, d , area of the MOS stack, A , and the dielectric constant, ϵ_i , of the dielectric layer, then it is possible to calculate the corresponding capacitance of the insulator. The relationship is shown as follows:

$$C_i = \frac{\epsilon_i A}{d} \quad (\text{A-4})$$

The next important parameter in the process is calculation of the overall flatband capacitance and the ratio:

$$C_{FB} = \frac{C_{FBS} C_i}{C_{FBS} + C_i} \quad (\text{A-5})$$

$$\frac{C_{FB}}{C_i} \quad (A-6)$$

The next step is to calculate the V_{shift} this is done by plotting C/C_i versus gate voltage. Then use the ratio of C_{FB}/C_i to visually determine the flatband voltage shift (ΔV_{shift}). In an ideal MOS capacitor, the flatband voltage condition corresponds to a $\Delta V_{shift} = 0$ thereby allowing the conclusion that any voltage shift should be related to total fixed charge. This charge may come from many different sources:

Q_m	>	Mobile Charges	>	location dependent on bias
Q_{ot}	>	Oxide Trapped	>	distributed in the oxide
Q_f	>	Fixed Oxide	>	near surface charge
Q_{it}	>	Interfacial Traps	>	at the interface

The first three of these charges causes shifts of the overall CV curve to the left or right while the fourth charge manifests itself as changes in slope (stretching) of the overall CV curve.

The next step is to determine the value of ΔV_{shift} , which is the work function of the metal minus the work function of the semiconductor. Depending on the wafer type used, this would be done as follows

$$p\text{-type} \quad f_{MS} = f_M - f_s = f_M - \left[X + \frac{E_g}{2} + \Psi_B \right] \quad (A-7)$$

$$n\text{-type} \quad f_{MS} = f_M - f_s = f_M - \left[X + \frac{E_g}{2} - \Psi_B \right] \quad (A-8)$$

where $E_g/2$ is the intrinsic Fermi level, f_M is the metal work function, f_s is the semiconductor work function, ΔE_F is the electron affinity of the semiconductor, and $\Delta \Psi_B$ is the Fermi level difference between the Fermi level and the intrinsic Fermi level.

Finally, the total oxide charge may be calculated with the following equation by collating all of the previously determined values as:

$$\text{n-type} \quad N_f = \left[\frac{\Delta V - f_{MS}}{q} \right] C_i \quad (\text{A-9})$$

Another important electrical value that is commonly cited in literature is the value of the interface traps, Q_{it} . There are several possibilities for determining this value: 1) comparison of the high frequency capacitance to a theoretical capacitance without any interface traps, 2) comparison of a low frequency capacitance to a theoretical capacitance without any interface traps, or 3) comparison of a high frequency capacitance to a low frequency capacitance. The third option, first developed by Castagné and Vapaille consisted of combining the low and high frequency curves (i.e., the output of the Win-82 system) to determine the silicon surface capacitance per unit area, C_s . Unlike the Terman method where only the high frequency capacitance (C_{HF}) is measured, or the Berglund method where only low frequency capacitance (C_{LF}) is measured, this method measures both C_{LF} and C_{HF} . This eliminates the need for the generation of any of the theoretical computations needed for the other methods. As outlined in more detail by Nicollan and Brews,⁷³ the basic result is that interface trap level can be determined at a given voltage as a function of position in the bandgap by simple input of measured parameters into the following equation:

$$D_{it} = \frac{\Delta C}{q} \left(1 - \frac{C_{HF} + \Delta C}{C_{ox}} \right)^{-1} \left(1 - \frac{C_{HF}}{C_{ox}} \right)^{-1} \quad (\text{A-10})$$

where D_{it} is the interface trap density, C_{ox} is the capacitance per unit area, and

$$\Delta C = C_{HF} - C_{LF} \quad (\text{A-11})$$

This equation is used to make a plot if D_{ito} versus C_{HF}/C_{ox} where

$$D_{it} = D_{ito} \frac{1000}{x_o} \quad (\text{A-12})$$

and x_o is the thickness of the oxide in question. Combination of the directly measured CV data and the above equation it is therefore possible to determine the Dito. It is important to realize, however, that accurate values of D_{it} cannot be determined over the entire range of gate bias' due to a variety of reasons including round-off errors, errors due to use of a 1 Mhz CV curve, and error from C_{LF} . Each of these errors is addressed in detail in Nicollian and Brews.⁷³

APPENDIX B XPS DATA

The following tables are the compilation from the XPS data collected for analysis in Chapter 3. Extensive peak position, area, intensity, and calculation of layer thickness are presented in the tables for each of the samples at the three take-off angles used.

	HF11M1	HF11M2	HF11M3	HF12M1	HF12M2	HF12M3	HF13M1	HF13M2	HF13M3
Carbon Peak Location	287.2	287.1	287.1	287.0	287.0	287.0	286.7	286.7	286.7
Si 2p A Location	100.7	100.7	100.7	100.7	100.7	100.7	100.8	100.8	100.8
Si 2p A Area	3134	7727	9642	2734	4574	6287	3781	7501	9287
Si 2p B Location	104.4	104.4	104.4	104.2	104.2	104.2	103.7	103.8	103.9
Si 2p B Area	6305	5798	5511	5652	5176	5785	2875	4678	4291
Si 2p A/B Ratio	0.50	1.33	1.75	0.48	0.88	1.09	1.32	1.60	2.16
Si 2p A and B separation	3.6	3.7	3.7	3.5	3.5	3.4	3.4	2.9	3.1
Si 2p C location	102.9	102.4	102.5	102.3	102.3	102.4	102.4	102.4	102.4
Si 2p C area	33	148	502	441	441	167	531.6	531.6	531.6
O 1s A Location	532.2	532.2	532.2	532.0	532.1	532.1	531.6	531.6	531.6
O 1s A Area	58093	60924	58894	47008	60448	57678	59339	62066	63831
O 1s B Location	533.7	533.6	533.5	533.4	533.7	533.5	533.3	533.2	533.3
O 1s B Area	21324	18589	16646	29873	17737	17906	26036	22291	16860
Hf 4f A Location	19.5	19.5	19.5	19.3	19.4	19.4	18.9	18.9	18.9
Hf 4f A Area	56342	56808	53597	54300	55767	53821	60417	60428	57927
Hf 4f B Location	21.2	21.2	21.2	21.0	21.0	21.0	21.0	20.6	20.6
Hf 4f B Area	46676	45073	42545	46406	45977	44682	51799	50019	48335
O Auger A Location	744.6	744.5	744.4	744.4	744.4	744.4	743.9	743.9	743.9
O Auger A Area	58495	56032	55106	41048	54929	57889	57613	58549	65622
O Auger B Location	747.7	747.2	747.1	746.9	747.3	747.3	746.9	746.8	746.7
O Auger B Area	14131	20545	23776	16394	15431	15695	13705	15949	14648
O Auger C Location	740.8	740.7	740.8	741.2	740.8	740.6	740.1	740.5	739.8
O Auger C Area	10528	17554	15573	17260	12616	11916	13095	13150	15913
Take Off Angle	45	65	90	45	65	90	45	65	90
$\sin(\alpha) \ln(B/A^{1/\beta} + 1)$	0.89	0.60	0.54	0.90	0.80	0.77	0.47	0.52	0.46
thickness (angstroms)	32	22	19	32	29	28	17	19	16
Ratio of Hf A to O 1s A	0.97	0.93	0.91	1.16	0.92	0.93	1.02	0.97	0.91
Ratio of Hf A to O 1s B	2.64	3.06	3.22	1.82	3.14	3.01	2.32	2.71	3.44

	HF14M1	HF14M2	HF14M3	HF15M1	HF15M2	HF15M3	HF16M1	HF16M2	HF16M3
Carbon Peak Location	287.1	287.1	287.0	287.2	287.3	287.2	287.0	287.0	286.9
Si 2p A Location	100.9	100.9	100.9	101.0	100.9	100.9	100.9	100.9	100.9
Si 2p A Area	3235	5039	7670	2454	4047	5565	6260	7784	10184
Si 2p B Location	104.4	104.4	104.3	104.5	104.5	104.5	104.3	104.3	104.3
Si 2p B Area	5870	4913	4427	4060	3255	3584	9676	8775	7523
Si 2p A/B Ratio	0.55	1.03	1.73	0.60	1.24	1.55	0.65	0.89	1.35
Si 2p A and B separation	3.5	3.5	3.5	3.6	3.7	3.6	3.4	3.4	3.4
Si 2p C Location				102.4	102.4	102.7	102.2	102.5	102.5
Si 2p C area				495	839	422	667	703	984
O 1s A Location	532.2	532.2	532.2	532.3	532.2	532.3	531.9	532.0	532.1
O 1s A Area	59528	63457	62528	31879	32144	33466	31495	67680	64712
O 1s B Location	533.7	533.6	533.5	533.7	533.7	533.8	533.4	533.4	533.4
O 1s B Area	17728	15221	14471	10772	10073	7127	12984	21273	18016
Hf 4f A Location	19.4	19.5	19.5	19.6	19.6	19.6	19.2	19.3	19.4
Hf 4f A Area	57527	57975	55212	30024	29194	28352	30709	60024	55069
Hf 4f B Location	21.1	21.1	21.1	21.2	21.2	21.2	20.9	21.0	21.0
Hf 4f B Area	47592	47319	47085	24932	23838	22825	26355	51324	47625
O Auger A Location	744.6	744.5	744.6	744.7	744.6	744.6	744.4	744.4	744.5
O Auger A Area	60697	63028	63237	28219	29035	30477	30564	63575	71267
O Auger B Location	747.7	747.5	747.5	747.6	747.3	747.4	747.5	747.3	747.7
O Auger B Area	13918	16824	16921	8803	10360	8943	7264	19825	15833
O Auger C Location	740.6	740.7	740.8	740.8	741.0	740.9	740.5	740.5	740.3
O Auger C Area	12038	11775	12918	7671	7452	6681	6437	12875	14522
Take Off Angle	45	65	90	45	65	90	45	65	90
$\sin(\alpha)LN(B/A^*1/\beta)+1)$	0.84	0.72	0.54	0.79	0.63	0.59	0.76	0.80	0.65
thickness (angstroms)	30	26	20	29	23	21	27	29	24
Ratio of Hf A to O 1s A	0.97	0.91	0.88	0.94	0.91	0.85	0.98	0.89	0.85
Ratio of Hf A to O 1s B	3.25	3.81	3.82	2.79	2.90	3.98	2.37	2.82	3.06

	HF17M1	HF17M2	HF17M3	HF18M1	HF18M2	HF18M3	HF19M1	HF19M2	HF19M3
Carbon Peak Location	286.8	286.7	286.7	286.8	286.7	286.7	286.9	286.9	286.9
Si 2p A Location	100.8	100.8	100.8	100.8	100.8	100.8	100.9	100.9	100.9
Si 2p A Area	1665	3639	4939	2215	4489	6312	4576	6756	8587
Si 2p B Location	104.3	104.2	104.4	104.3	104.3	104.3	104.4	104.5	104.5
Si 2p B Area	4656	4788	5258	5378	7031	6885	12812	12119	10678
Si 2p A/B Ratio	0.36	0.76	0.94	0.41	0.64	0.92	0.36	0.56	0.80
Si 2p A and B separation	3.5	3.4	3.6	3.5	3.5	3.5	3.6	3.6	3.6
Si 2p C location			102.5	102.4	102.3	102.4		102.2	102.5
Si 2p C area			779	2	541	833		751	1156
O 1s A Location	531.8	531.9	531.8	531.8	531.9	531.9	532.0	532.1	532.2
O 1s A Area	67045	6461	69728	59573	63711	62455	61067	67145	68478
O 1s B Location	533.3	533.2	533.4	533.4	533.4	533.4	533.5	533.5	533.7
O 1s B Area	20340	18942	13041	19713	16512	17420	26526	19921	16142
Hf 4f A Location	19.0	19.0	19.1	19.0	19.0	19.1	19.1	19.3	19.5
Hf 4f A Area	63600	61210	59345	56713	56496	56829	58638	58653	55278
Hf 4f B Location	20.6	20.7	20.7	20.3	20.7	20.8	21.0	21.1	21.1
Hf 4f B Area	54533	51683	50207	48879	48685	48523	47962	47401	45171
O Auger A Location	744.3	744.3	744.3	744.4	744.4	744.4	744.7	744.7	744.6
O Auger A Area	69462	69268	71170	63948	59611	58595	58975	67505	62218
O Auger B Location	747.4	747.3	747.3	747.7	747.3	747.2	747.7	747.8	747.3
O Auger B Area	15281	18036	17643	13566	19350	20396	16329	17843	24290
O Auger C Location	739.9	740.4	740.2	740.0	741.0	741.1	741.0	740.8	740.6
O Auger C Area	15252	14980	14326	9612	12212	12494	11310	13198	18073
Take Off Angle	45	65	90	45	65	90	45	65	90
$\sin(\alpha) \ln(B/A^{1/\beta} + 1)$	1.06	0.88	0.85	0.99	0.98	0.86	1.06	1.07	0.94
thickness (angstroms)	38	32	30	36	35	31	38	38	34
Ratio of Hf A to O 1s A	0.95	0.92	0.85	0.95	0.89	0.91	0.96	0.87	0.81
Ratio of Hf A to O 1s B	3.13	3.23	4.55	2.88	3.42	3.26	2.21	2.94	3.42

LIST OF REFERENCES

- ¹ G. D. Wilk, R. M. Wallace, and J. M. Anthony, *J. Appl. Phys.* **89**, 5243 (2001).
- ² G. E. Moore, *Electron.* **19**, 114 (1965).
- ³ J. D. Plummer and P. B. Griffin, *Proceedings of the IEEE* **89**, 240 (2001).
- ⁴ *International Technology Roadmap for Semiconductors*, 2002 edition, ITRS Home Page, <http://public.itrs.net/Files/2002Update/2001ITRS/ExecSum.pdf> (02/16/2004).
- ⁵ R. Degraeve, E. Cartier, T. Kauerauf, R. Carter, L. Pantisano, A. Kerber, and G. Grossenbacher, *Mat. Res. Soc. Bulletin* **27**, 222 (2002).
- ⁶ J. Kwo, M. Hong, A. R. Kortan, K. L. Queeney, Y. J. Chabal, R. L. Opila Jr., D. A. Muller, S. N. Chu, B. J. Sapjeta, T. S. Lay, J. P. Mannaerts, T. Boone, H. W. Krautter, J. J. Krajewski, A. M. Sergent, and J. M. Rosamilia, *J. Appl. Phys.* **89**, 3920 (2001).
- ⁷ K. J. Hubbard and D. G. Schlom, *J. Mater. Res.* **11**, 2757 (1996).
- ⁸ J. P. Liu, P. Zaumseil, E. Bugiel, and H. J. Osten, *Appl. Phys. Lett.* **79**, 671 (2001).
- ⁹ D. G. Schlom and J. H. Haeni, *Mat. Res. Soc. Bulletin* **27**, 198 (2002).
- ¹⁰ R. D. Shannon, *J. Appl. Phys.* **73**, 398 (1993).
- ¹¹ A. Shanware, J. McPherson, M. R. Visokay, J. J. Chambers, A. L. Rotondaro, H. Bu, M. J. Bevan, R. Khamankar, and L. Colombo, *IEEE Electron Devices Meeting, 2001. IEDM Technical Digest International*, **2001** p. 6.6.1-6.6.4.
- ¹² W. Zhu, T. P. Na, H. Tamagawa, Y. Di, J. Kim, R. Carruthers, M. Gibson, and T. Furukawa, *IEEE Electron Devices Meeting, 2001. IEDM Technical Digest International*, **2001** p. 20.4.1-20.4.4.
- ¹³ C. W. Yang, Y. K. Fang, C. H. Chen, W. D. Wang, T. Y. Lin, M. F. Wang, T. H. Hou, J. Y. Cheng, L. G. Yao, S. C. Chen, C. H. Yu and M. S. Liang, *Electronics Lett.* **38**, 1223 (2002).
- ¹⁴ National Technology Roadmap for Semiconductors. Semiconductor Industry Association, San Jose, CA, **1997** p. 72.

- ¹⁵ A. I. Kingon, J. P. Maria, and S. K. Streiffer, *Nature* **406**, 1032 (2000).
- ¹⁶ G. Lucovsky, *J. Vac. Sci. Technol. A* **19**, 1553 (2001).
- ¹⁷ N. H. Weste and K. Eshraghian, *Principles of CMOS VLSI Design: A Systems Perspective*, Second Edition, Addison Wesley Publishing Company, New York, **1994** p 123.
- ¹⁸ Intel Home Page, <http://www.intel.com/home/glossary/body.htm> (06/24/2004).
- ¹⁹ S. Tang, R. M. Wallace, A. Seabaugh, and D. King-Smith, *Appl. Surf. Sci.* **135**, 137 (1998).
- ²⁰ B. E. Weir, P. J. Silverman, M. A. Alam, F. Baumann, D. Monroe, A. Ghetti, J. D. Bude, G. L. Timp, A. Hamad, and T. M. Oberdick, *Tech. Dig. Int. Electron Devices Meet.* **1999**, p. 437.
- ²¹ D. J. Frank, R. H. Dennard, E. Nowak, P. M. Solomon, Y. Taur, and H. P. Wong, *Proceedings of the IEEE* **89**, 259 (2001).
- ²² M. Depas, B. Vermeire, P. W. Mertens, R. L. Van Meirhaeghe, and M.W. Heynes, *Solid-State Electron.* **38**, 1465 (1995).
- ²³ D. A. Buchanan, *IBM J. Res. Develop.* **43**, 245 (1999).
- ²⁴ H. P. Wong, *IBM J. Res. Develop.* **46**, 133 (2002).
- ²⁵ J. Robertson, *Mat. Res. Soc. Bulletin* **27**, 217 (2002).
- ²⁶ J. J. Chambers and G. N. Parsons, *J. Appl. Phys.* **90**, 918 (2001).
- ²⁷ B. H. Lee, R. Choi, L. Kang, S. Gopalan, R. Nieh, K. Onishi, Y. Jeon, W.J. Qi, C. Kang, and J. C. Lee, *Electron Devices Meeting, 2000. IEDM Technical Digest. International*, **2000** p. 39.
- ²⁸ L. Manchanda, M. L. Green, R. B. van Dover, M. D. Morris, A. Kerber, Y. Hu, J. P. Han, P. J. Silverman, T. W. Sorsch, G. Weber, V. Donnelly, K. Pelhos, F. Klemens, D. Jacobson, J. Eng, B. Busch, and H. Schulte, *Electron Devices Meeting, 2000. IEDM Technical Digest. International*, **2000** p. 23.
- ²⁹ B. Y. Park, J. Park, M. Cho, C. S. Hwang, K. Oh, Y. Han, and D. Y. Yang, *Appl. Phys. Lett.* **80**, 2368 (2002).
- ³⁰ L. Kang, B. H. Lee, W. J. Qi, Y. Jeon, R. Nieh, S. Gopalan, K. Onishi, and J. C. Lee, *IEEE Electron Dev. Lett.* **21**, 181 (2000).

- ³¹ S. W. Nam, J. H. Yoo, S. Nam, H. J. Choi, D. Lee, D. H. Ko, J. H. Moon, J. H. Ku, and S. Choi, *J. Non Cryst. Solids* **303**, 139 (2002).
- ³² P. D. Kirsch, C. S. Kang, J. Lozano, J. C. Lee, and J. G. Ekerdt, *J. Appl. Phys.* **91**, 4353 (2002).
- ³³ H. Lee, S. Jeon, and H. Hwang, *Appl. Phys. Lett.* **79**, 2615 (2001).
- ³⁴ H. Yu, M. F. Li, B. J. Cho, C. C. Yeo, M. S. Joo, D. L. Kwong, J. S. Pan, C. H. Ang, J. Z. Zheng, and S. Ramanathan, *Appl. Phys. Lett.* **81**, 376 (2002).
- ³⁵ H. Cho, C. S. Kang, K. Onishi, S. Gopalan, R. Nieh, R. Choi, S. Krishnan, and J. C. Lee, *IEEE Electron Device Lett.* **23**, 249 (2002).
- ³⁶ C. W. Yang, Y. K. Fang, C. H. Chen, W. D. Wang, T. Y. Lin, M. F. Wang, T. H. Hou, J. Y. Cheng, L. G. Yao, S. C. Chen, C. H. Yu, and M. S. Liang, *Electron. Lett.* **38**, 1223 (2002).
- ³⁷ A. Kazor and I. W. Boyd, *J. Appl. Phys.* **75**, 227 (1994).
- ³⁸ E. M. Young and W. A. Tiller, *J. Appl. Phys.* **62**, 2086 (1987).
- ³⁹ Z. Cui, J. M. Madsen, and C. G. Takoudis, *J. Appl. Phys.* **87**, 8181 (2000).
- ⁴⁰ D. L. Blaluch, R. A. Cox, R. F. Hampson, J. A. Herr, J. Tore, and R. T. Watson, *Phys. Chem. Ref. Data* **9**, 295 (1980).
- ⁴¹ A. M. Goodman, *Phys. Rev. B* **152**, 785 (1966).
- ⁴² R. Williams, *Phys. Rev. B* **140**, A 569 (1965).
- ⁴³ B. E. Deal and A. S. Grove, *J. Appl. Phys.* **36**, 3770 (1965).
- ⁴⁴ Ishikawa, T. Shibamoto, and I. Nakamichi, *Jpn. J. Appl. Phys.* **31**, 1148 (1992).
- ⁴⁵ S. Ramanathan, P. C. McIntyre, J. Luning, P. Pianetta, and D. A. Muller, *Phil. Mag. Lett.* **82**, 519 (2002).
- ⁴⁶ S. Ramanathan, D. A. Muller, G. D. Wilk, C. M. Park, and P. C. McIntyre, *Appl. Phys. Lett.* **79**, 3311 (2001).
- ⁴⁷ S. Ramanathan, G. D. Wilk, D. A. Muller, C.M. Park, and P. McIntyre, *Appl. Phys. Lett.* **79**, 2621 (2001).
- ⁴⁸ S. Ramanathan, C.M. Park, and P. C. McIntyre, *J. Appl. Phys.* **91**, 4521 (2002).

- ⁴⁹ S. Ramanathan and P. C. McIntyre, *Appl. Phys. Lett.* **80**, 3793 (2002).
- ⁵⁰ S.J. Wang, *Semicond. Sci. Tech.* **16**, L13 (2001).
- ⁵¹ V. Misra, G. Lucovsky, and G. Parsons, *Mat. Res. Soc. Bulletin* **27**, 212 (2002).
- ⁵² H. Zhong, G. Heuss, and V. Misra, *IEEE Electron Device Lett.* **21**, 593 (2000).
- ⁵³ C.R. Brundle, C. A. Evans, and S. Wilson, *Encyclopedia of Materials Characterization*, Butterworth-Heinemann, Boston, **1992**.
- ⁵⁴ R. K. Singh and D. Kumar, *Mat. Sci. Engr. Reports* **R22**, 113 (1998).
- ⁵⁵ V. Craciun and R. K. Singh, *Electrochem. Solid-State. Lett.* **2**, 446 (1999).
- ⁵⁶ V. Craciun, E. S. Lambers, N. D. Bassim, R.K. Singh, and D. Craciun, *J. Mater. Res.* **15**, 488 (2000).
- ⁵⁷ V. Craciun, R.K. Singh, J. Perriere, J. Spear, and D. Craciun, *J. Electrochem. Soc.* **147**, 1077 (2000).
- ⁵⁸ A. Srivastava, V. Craciun, J. M. Howard, and R. K. Singh, *Appl. Phys. Lett.* **75**, 3002 (1999).
- ⁵⁹ V. Craciun and R. K. Singh, *Appl. Phys. Lett.* **76**, 1932 (2000).
- ⁶⁰ V. Craciun, J. M. Howard, N. D. Bassim, and R. K. Singh, Transport and Microstructural Phenomena in Oxide Electronics, Editors: Dave H. Blank, David S. Ginley, Marilyn E. Hawley, Stephen K. Streiffer, David C. Paine, *MRS Proceedings Volume 666*, F11.4, **2001**.
- ⁶¹ V. Craciun, N. D. Bassim, J. M. Howard, J. Spear, S. Bates, and R. K. Singh, MRS Spring Meeting, Transport and Microstructural Phenomena in Oxide Electronics, Editors: Dave H. Blank, David S. Ginley, Marilyn E. Hawley, Stephen K. Streiffer, David C. Paine, *MRS Proceedings Volume 666*, F8.11.1, **2001**.
- ⁶² V. Craciun, C. Chiritescu, F. Kelly, and R.K. Singh, *J. Optoelectronics and Adv. Mat.* **4**, 21-26 (2002).
- ⁶³ F. Iacona, R. Kelly, and G. Marletta, *J. Vac. Sci. Technol. A* **17**, 2771 (1999).
- ⁶⁴ L. A. Knauss, J. M. Pond, J. S. Horwitz, D. B. Chrisey, C. H. Mueller, and R. Treece, *Appl. Phys. Lett.* **69**, 25 (1996).
- ⁶⁵ H. Ono, Y. Hosokawa, T. Ikarashi, K. Shinoda, N. Ikarashi, K. Koyanagi, and H. Yamaguchi, *J. Appl. Phys.* **89** (2), 995 (2001).

- ⁶⁶ T. J. Vink, R. G. F. A. Verbeek, J. H. M. Snijders, and Y. Tamminga, *J. Appl. Phys.* **87** (10), 7252 (2000).
- ⁶⁷ V. Craciun, J. M. Howard, N. D. Bassim, and R. K. Singh, *Appl. Surf. Sci.* **168** (1-4), 123 (2000).
- ⁶⁸ C. H. Choi, T. S. Jeon, R. Clark, and D. L. Kwong, *IEEE Electron Device Letters* **24**, 215 (2003).
- ⁶⁹ J. M. Howard, Ultraviolet-assisted Processing of Dielectric Thin Films for Metal Oxide Semiconductor Applications, Ph.D. Dissertation, University of Florida, **2002** p.111.
- ⁷⁰ Z. H. Lu, J. P. McCaffrey, B. Brar, G. D. Wilk, R. M. Wallace, L. C. Feldman, and S. P. Tay, *Appl. Phys. Lett.* **71**, 2764 (1997).
- ⁷¹ H. Sim, H. Chang, and H. Hwang, *Jpn. J. Appl. Phys. Part I, No. 4A*, **42**, 1596 (2003).
- ⁷² D. Young, H. D. Wu, R. C. Y. Auyeung, and R. Modi, *J. Mater. Res.* No. 6, **16**, 1720 (2001).
- ⁷³ E. H. Nicollian and J. R. Brews, *MOS (Metal Oxide Semiconductor) Physics and Technology*, Wiley, New York, **1982**.

BIOGRAPHICAL SKETCH

Chad Robert Essary was born in Springfield, Missouri, on March 3rd, 1976. He grew up in Southwest Missouri and attended Forsyth High School in Forsyth, Missouri. Upon graduation as co-valedictorian of his class in 1994, he began an undergraduate curriculum at the University of Missouri-Rolla. Chad graduated in the spring of 1998 with a Bachelor of Science in ceramic engineering and minors in mathematics and history. He decided to stay at Rolla for his masters work under the guidance of Dr. Wayne Huebner. In the summer of 2000, Chad graduated with a Master of Science degree in ceramic engineering for his thesis work entitled Processing and Characterization of Ceramic Tape Layers for Ultra-high Gradient Insulators. In the fall of 2000, Chad moved to Gainesville, Florida, to pursue a doctorate degree in the Department of Materials Science and Engineering at the University of Florida.